THE ASTROPHYSICAL JOURNAL SUPPLEMENT SERIES, 87:63–133, 1993 July

THE RADIO PROPERTIES OF HIGH-REDSHIFT QUASARS. I. DUAL-FREQUENCY OBSERVATIONS OF 79 STEEP-SPECTRUM QUASARS AT $z > 1.5$

C. J. LONSDALE,[1] P. D. BARTHEL,[2] AND G. K. MILEY[3]
Received 1992 October 5; accepted 1992 December 8

ABSTRACT

We have made sensitive VLA observations of virtually all known high-redshift ($z > 1.5$) radio-loud QSOs with extended radio morphologies. The resulting images (at 6 and 2 cm wavelength, including linear polarization) have angular resolutions of typically 0".4 and 0".15 and are compiled here. This compilation of maps will permit the extraction of numerous radio source parameters, constituting a data base for comprehensive statistical analyses to be explored in subsequent papers. The data base is particularly useful for statistical studies. The key characteristics of the sample are the narrow redshift range, the narrow distribution in linear resolutions of the maps, the narrow distribution of map sensitivity to emitting regions of standard physical characteristics, and the relatively narrow range of source luminosities. As a result of these properties, the sample enjoys relative freedom from the effects of parameter correlations with redshift and luminosity. A brief discussion of the sample characteristics and some elaboration of the particular advantages of this sample are presented. Some clear trends in the data are discussed briefly.

Subject headings: polarization — quasars: general — radio continuum: galaxies — surveys

I. INTRODUCTION

Radio observations have proven extremely important in developing our understanding of extragalactic objects, particularly in the early universe. The discovery of radio galaxies (e.g., Baade & Minkowski 1954) and quasars (e.g., Sandage 1960; Schmidt 1963) through radio astronomy mark milestones in extragalactic research. The study of extragalactic radio sources has developed steadily since the 1950s, and major discoveries include: (1) The establishment that a double-lobed structure straddling a radio core and associated optical object is a common property (Maltby & Moffet 1963), with linear dimensions for the overall radio morphologies up to several megaparsecs (Willis, Strom, & Wilson 1974). These lobe-dominated sources are found to be associated both with faint galaxies and QSOs. (2) The frequent detection of bright compact hot spots at the edges of the most luminous sources (Macdonald, Kenderdine, & Neville 1968; Miley & Wade 1971), and the subsequent discovery that this morphological property can be used for a bimodal luminosity classification (Fanaroff & Riley 1974). (3) The detection of essentially pointlike, compact radio sources, often variable in flux density, and usually identified with QSOs (Dent 1965). Sensitive observations commonly detect faint extended emission around these core-dominated sources (e.g., O'Dea, Barvainis, & Challis 1988; Kollgaard, Wardle, & Roberts 1990). (4) The discovery of large-scale jets, linking the compact radio cores with the outer lobes (Hogg et al. 1969; Van Breugel & Miley 1977; Potash & Wardle 1979). (5) The establishment, with VLBI techniques that the core components in both core- and lobe-dominated radio sources are indeed very compact, with angular dimensions on the milliarcsecond scale (Clark et al. 1968; Kellermann et al. 1975), and common (Schilizzi 1976; Barthel et al. 1984).

Despite substantial advances in instrumentation over the years, understanding of radio source physical mechanisms remains primitive. Perhaps the most important step forward in our knowledge of the radio source phenomenon is the recognition that energy is transported from the central engine and deposited in the lobes via a narrow, fast-moving, collimated flow of material, generally referred to as a beam, and observationally manifested as a quasi-linear feature universally known as a jet (e.g., Bridle & Eilek 1984; Hughes 1991). It is now possible, given a wealth of high-quality radio images, to construct a broadly accepted, but fundamentally qualitative picture of a radio source, supported by ever more sophisticated fluid dynamical simulations (e.g., Norman et al. 1982). Energy from the central engine (the nature of which remains poorly constrained beyond the likelihood that accretion onto a supermassive black hole is involved; Blandford 1990) is transported, probably dominantly in the form of bulk kinetic energy, down a narrow pipeline at speeds which start out relativistic, at least in powerful sources, but may slow to nonrelativistic speeds many kiloparsecs from the nucleus (Bridle 1992). If the parameters of the flow, particularly involving the Mach number, are in a regime typical of high-power sources, the beam terminates abruptly at a strong shock, with concomitant compression and (probably) particle acceleration, resulting in one or more prominent hot spots surrounded by relatively diffuse lobe emission. Conversely, if the source power is low, the beam lacks stability and will tend to entrain surrounding material, eventually slowing down to form a subsonic plume with no terminal hot spot. These general radio source characteristics are discussed in much greater detail by Bridle (1992).

Many fundamental details of this picture remain unknown. For example, the efficiency with which energy from the central engine is converted first to bulk kinetic energy in the beam,

[1] MIT/NEROC Haystack Observatory, Westford, MA 01886.
[2] Kapteyn Astronomical Institute, P.O. Box 800, NL–9700 AV Groningen, The Netherlands.
[3] Leiden Observatory, P.O. Box 9513, NL–2300 RA Leiden, The Netherlands.

then to relativistic particle and magnetic field energy in the synchrotron emitting regions, and finally to the observed radio radiation, is almost completely unconstrained by observation. This efficiency is a vital part of any complete model of a radio source, but we cannot even make informed guesses about it, because the physical mechanisms involved in these various energy conversions are not agreed upon (e.g., Eilek & Hughes 1991). The characteristic velocities and evolutionary time scales of various parts of radio sources are poorly known. Estimates often rely on highly model dependent calculations involving aging of the synchrotron electron population without the benefit of knowledge of the initial electron energy spectrum (e.g., Liu, Pooley, & Riley 1992), or on assumptions of source symmetry combined with differential light travel time arguments (e.g., Longair & Riley 1979), despite pervasive evidence for widespread intrinsic source asymmetry. These time scale uncertainties again translate directly into uncertainty in the time-integrated energy demands on the central engine—something we would like to constrain. The composition of the radio emitting regions is essentially unknown in most cases. Energy equipartition between the thermal plasma, the relativistic electrons and protons, and the magnetic field is typically assumed but almost never observationally justified, leading to large uncertainties in internal pressures, which in turn prohibit reliable inferences about expansion rates, lifetimes, and external medium properties. The thermal electron content of jets, hot spots and lobes, in theory constrained by measurements of internal Faraday depolarization (e.g., Miley 1980), are in practice typically unmeasurable, due to foreground magnetoionic screens with small-scale irregularities, and a lack of knowledge of the magnetic field configuration and strength within the emitting region, including line-of-sight field reversals.

A characteristic of the radio source population is its diversity, particularly in morphology. Sources come in all shapes and sizes (Miley 1980), and particularly in high-luminosity objects, can appear asymmetric from side to side. The most notorious asymmetry involves the jets, which are typically one-sided in quasars (e.g., Owen 1986). Other systematic asymmetries have been noted, involving, for example, lobe depolarization (e.g., Garrington et al. 1988; Laing 1988) and associated optical line emitting gas (McCarthy, Van Breugel, & Kapahi 1991). In the past decade, much attention has focused on the role that source orientation with respect to the line of sight plays in the appearance of sources, particularly with regard to asymmetries, distorted morphologies, the incidence of core-dominated sources, and superluminal motion (Orr & Browne 1982; Barthel 1989; Garrington & Conway 1991; Padovani & Urry 1991). These models attempt to unify core-dominated and lobe-dominated quasi-stellar radio sources (QSRs), and subsequently QSRs and (FR2) radio galaxies by the effects of viewing angle combined with anisotropic obscuration. Such unification models depend critically on the presence of bulk relativistic flow velocities, and hence relativistic beaming effects in the small- and large-scale jets. On the other hand, some of the observed radio properties and correlations as well as radio-optical correlations can be explained as being due to source intrinsic, physical phenomena (e.g., Liu & Pooley 1991; McCarthy et al. 1991). Our lack of knowledge of the Doppler boosting factors associated with various parts of radio sources of various types substantially complicates attempts to construct an accurate picture of the orientation independent structure and overall energetics of a source and its constituent parts. Disentangling the effects of orientation and relativistic beaming from source intrinsic properties is a prerequisite to understanding many aspects of the radio source phenomenon, and should be accorded high priority.

Two complementary observational approaches have been employed in order to address these astrophysical questions and problems. The first, typified by the work of Carilli et al. (1991) on Cygnus A, is to perform highly detailed, state-of-the-art observations of a nearby, hopefully representative object in an effort to make measurements of sufficient accuracy and variety to constrain the physical processes involved in the formation of the source. The second, more common approach is to perform necessarily more cursory observations of a well-defined statistical sample of radio sources, and to search for telltale trends and patterns in the sample population. Both approaches have key drawbacks. The single source approach suffers from the impossibility of selecting a truly representative source to study, especially in view of the intrinsic diversity of the radio source population. As an example, the Faraday rotation measures due to the magnetoionic screen in front of Cygnus A are anomalously high compared to the general radio source population. Conversely, statistical studies typically suffer from subtle but serious and often intractable selection effects and systematic biases. A classic example would be studies involving the 3CRR sample (Laing, Riley, & Longair 1983), in which luminosity and redshift are strongly correlated: the extragalactic 3CRR sources span a range of over four orders of magnitude in intrinsic luminosity. If one observes a correlation between, say, overall lobe spectral index and hot spot prominence in such a sample, one may be tempted to speculate about electron acceleration, aging mechanisms and time scales as a function of the strength of the terminal shock in the jet. However, such a correlation is likely to arise purely as a result of secondary relationships with luminosity and redshift. Higher redshift sources will have higher luminosity, and therefore more prominent hot spots, while at the same time, we observe the lobes at a higher emitted frequency in high-redshift sources. Lobes typically have convex spectra, so the measured spectral index will steepen with redshift. The consequence of such effects is that heterogeneous samples such as 3CRR are insensitive to a wide variety of potential effects that in principle can shed light on the physics of radio sources.

Another phenomenon that can be viewed alternately as an intractable complication or a principal target of research is the cosmological evolution of radio sources. This can be due to evolution of the nature of the power supply, the environment with which the source interacts, or both. Radio galaxies at low and moderate redshift display evolution in their linear dimensions (Oort 1987), but due to the paucity of samples of high-redshift radio galaxies, most studies of cosmological evolution have been performed on quasars. On the basis of relatively crude maps, cosmological size evolution for QSRs has been reported since the late 1960s and early 1970s (Hogg 1969; Miley 1968, 1971; Wardle & Miley 1974). More detailed investigations have little doubt about this size evolution, despite the unavoidable luminosity selection effect (Barthel & Miley 1988; Kapahi 1989). Garrington & Conway (1991) report an

increasing depolarization asymmetry with redshift, whereas McCarthy et al. (1991) find some evidence for a more pronounced arm-length asymmetry in higher redshift radio galaxies. Using a preliminary set of 6 cm maps of the sample presented in this paper, Barthel & Miley (1988) and Bogers et al. (1992) have, by comparison with lower redshift QSR samples, reported evidence for an increased occurrence of distorted morphologies at high redshift.

To lay the groundwork for addressing some of the above-mentioned astrophysical issues, we have been carrying out an extensive radio imaging project. This project is aimed primarily at the generation of a high-quality data base of source properties in a specific, rather narrow fractional redshift range, for statistical investigation. Although the data base can be used for evolutionary studies in conjunction with matched lower redshift samples, as mentioned above, such utility is a secondary consideration here. We made sensitive VLA[4] observations of 79 (i.e., virtually all known) $z > 1.5$ radio-loud QSOs having steep radio spectra near 1 GHz. Being interested in radio morphological properties on kiloparsec scales (cores, jets, hotspots), we used the VLA in its highest resolution A-configuration. In order to obtain spectral information for source components, we observed at 6 cm (C-band) and 2 cm (U-band), preferring the highest angular resolution obtainable to matched array observations. We judged that the spectral index of most of the energetically important, bright, relatively compact components could be adequately measured despite differing angular resolutions at 6 and 2 cm, and that the structure of these small, distant sources would in many cases be poorly delineated at the 0".4 maximum resolution of matched-array observations at the VLA. In addition, for several dozen of the sample objects we obtained 20 cm (L-band) data, in order to map extended, low surface-brightness emission. The 20 cm maps will be published in a forthcoming paper, but we will mention some preliminary results in § 4.2. Stokes parameters Q and U were analyzed at all observing bands, to allow extraction of linear polarization characteristics. As explained below, our sample is characterized by uniformity, with the consequence that the small range of physical properties ensures relative freedom from selection effects and observational biases. We will discuss the QSR sample, with emphasis on its homogeneity, the VLA observations, which comprise ~60 hr of observing time, and the results. The latter are presented in the form of 167 radio maps, with accompanying table and notes on individual sources. Although we will postpone parameter extraction and statistical investigations of source properties to forthcoming papers, we will note here a few interesting trends that are clearly present.

2. SAMPLE SELECTION AND CHARACTERISTICS

The sample was selected from the Hewitt & Burbidge (1987) compilation on the basis of two primary criteria: (*a*) redshift greater than 1.5; and (*b*) radio spectral index in the vicinity of 1 GHz larger (steeper) than $\alpha = 0.6$ (where $S_\nu \propto \nu^{-\alpha}$). The steep spectrum selection criterion ensures that most of the sources will have extended radio structure. We used α_{1400}^{5000}, α_{408}^{5000}, α_{178}^{5000}, α_{178}^{1400}, or α_{408}^{1400}, whichever was available. These criteria were met by examination of the 3C, 4C, 5C, PKS, MC (Molonglo), W (Westerbork), and Ohio radio source surveys, and in some cases by determination of the spectral index directly from our previous VLA observations (Barthel et al. 1988, hereafter BMSL). To allow satisfactory mapping at the VLA, we applied a secondary criterion: (*c*) declination greater than −30°. Application of these criteria resulted in the compilation of 81 QSRs, of which we were able to observe 79 at 6 cm and 74 at 2 cm. The high-redshift QSR sample is listed in Table 1, together with some information from the VLA observations.

Columns (3), (4), and (8) list accurate optical QSO positions with references. Column (6) lists our measured 5 GHz flux density values (see also § 3), whereas the observing epochs are specified in column (7) (two dates mark different epochs at 6 and 2 cm, respectively). Two objects (MC3 1634+176 and PKS 2146−133, see BMSL for previous 6 cm maps) were not observed due to equipment failures at the VLA. Five QSRs [MC2 1214+106, 1559+173 (4C 17.65), 1606+289 (4C 28.40), 1629+680 (4C 68.18), and 2249+185 (3C 454)] could only be observed at 6 cm because of scheduling constraints and a computer failure. Omission of these objects does not bias the sample in any way. More details of the VLA observations are given in § 3 below. We believe that the sample has unique characteristics, which render it very useful for statistical studies. Among those characteristics are the following.

1. The sample exhibits a relatively narrow fractional redshift range (see Fig. 1). 80% of the sample members fall in the interval $1.5 < z < 2.2$, and all objects have $z < 2.9$. This narrow range has the consequence that uniform observational parameters transform to relatively uniform physical quantities at the source, and is a principal reason for the unique statistical utility of the database to be derived from the maps we present in this paper. Some of the other sample characteristics are a direct consequence of the limited redshift range.

2. The redshift range covered by the sample is one in which, for a standard cosmological model, the angular size distance D_a (Weinberg 1972) is approximately constant: the ratio of D_a ($z = 3$)/D_a ($z = 1$) = 1.2 and 0.8, for q_0 of zero and unity, respectively. When combined with the uniformity of our observational parameters, this translates to the property of our data that all sources have been observed with approximately constant linear resolution. The median resolving beam values of 0".4 and 0".15 (at 5 and 15 GHz, respectively) translate to ~3 kpc and ~1.2 kpc linear resolution, adopting $H_0 = 75$ km s^{-1} Mpc^{-1} and $q_0 = 0.05$. This characteristic, illustrated in Figures 2 and 3 greatly simplifies comparisons between sources in the sample.

3. The monochromatic source power at 15 GHz emitted frequency covers only 2 decades in magnitude, and 70% of the sources are contained within 1 decade (see Fig. 4). These values were calculated from the observed 5 GHz flux densities (Table 1) using standard formulae (Weinberg 1972), and on the assumption of an $\alpha = -1$ spectral index around 15 GHz emitted frequency. By the standards of other extragalactic radio source samples, all the sources may be considered to belong to the same luminosity class. While the source power is somewhat correlated with redshift (Fig. 5), the correlation is not strong. It will be noted from Figure 5 that omitting the 20% of the sample at redshifts greater than 2.2 significantly reduces

[4] The VLA is a facility of the National Radio Astronomy Observatory, which is operated by Associated Universities, Inc., under contract with the National Science Foundation.

TABLE 1

HIGH-REDSHIFT QUASAR SAMPLE

QUASAR	RADIO SOURCE	R.A.(1950)	DEC.(1950)	z	S_{5GHz}	OBS. EPOCH(S)	REFS.
0017+154	3C 9	$00^h17^m49^s.89$	+15°24′16″.4	2.012	443	04/86, 02/85	2, 3
0032+423	4C 42.01	00 32 23.33	+42 21 49.3	1.588	121	02/85, 04/86	1
0033+079	4C 08.04	00 33 40.96	+07 58 34.0	1.578	121	02/85, 04/86	1
0038−019	4C −02.04	00 38 52.62	−01 59 42.7	1.690	369	02/85, 04/86	1
0044−055	4C −05.03	00 44 12.01	−05 38 23.8	1.869	129	08/83, 02/85	1
0046−067	4C −06.04	00 46 25.86	−06 44 51.8	2.063	152	08/83, 04/86	4
0051+291	4C 29.01	00 51 02.11	+29 08 51.2	1.828	259	02/85	1
0109+176	4C 17.09	01 09 09.62	+17 37 56.1	2.157	143	04/86	1
0225−014	4C −01.11	02 25 35.04	−01 29 03.2	2.037	147	08/83, 02/85	1
0238+100	MC5	02 38 40.70	+10 05 59.5	1.816	76	04/86	1, 3
0316−203	MC	03 16 10.21	−20 23 12.0	2.880	39	04/86	1
0352+123	4C 12.17	03 52 59.25	+12 23 03.5	1.616	277	02/85, 08/83	1
0404+177	4C 17.22	04 04 36.15	+17 42 52.5	1.712	193	04/86, 02/85	1
0424−131	PKS	04 24 47.85	−13 09 33.4	2.165	267	04/86	1
0445+097	4C 09.17	04 45 37.12	+09 45 37.2	2.110	443	02/85, 08/83	1
0549−213	MC	05 49 50.56	−21 20 29.6	2.245	230	04/86	1
0553−205	MC	05 53 09.99	−20 30 19.7	1.544	68	02/85, 04/86	1
0730+257	4C 25.21	07 30 05.48	+25 42 54.8	2.686	158	02/85, 04/86	1, 3, 5
0730+659	W1	07 30 17.96	+65 59 39.0	1.937	24	04/86	1
0747+613	OI 680	07 47 50.17	+61 20 06.0	2.492	293	04/86, 02/85	1
0751+298	4C 29.27	07 51 50.96	+29 49 50.7	2.106	155	04/86	1
0758+120	MC5	07 58 14.49	+12 01 43.3	2.660	43	04/86	1
0802+103	3C 191	08 02 03.80	+10 23 58.1	1.956	506	08/83, 02/85	1
0835+580	3C 205	08 35 10.02	+58 04 51.4	1.534	588	08/83	1, 2, 6, 7
0836+195	4C 19.31	08 36 15.00	+19 32 24.6	1.691	149	08/83, 04/86	1
0843+136	4C 13.39	08 43 01.35	+13 39 57.4	1.875	180	03/85, 08/83	1
0848+155	OJ 180	08 48 04.36	+15 33 30.6	2.101	192	04/86, 02/85	1
0856+124	MC5	08 56 49.55	+12 28 17.1	1.760	46	08/83, 04/86	1
0926+117	4C 11.32	09 26 01.06	+11 47 32.4	1.754	165	04/86, 02/85	1
0941+261	OK 270	09 41 50.22	+26 08 32.0	2.910	339	02/85	1
1023+067	3C 243	10 23 55.15	+06 42 50.7	1.699	205	02/85, 04/86	1
1055+499	5C 02.56	10 55 17.73	+49 55 39.7	2.390	100	04/86, 08/83	1
1153+317	4C 31.38	11 53 44.08	+31 44 46.85	1.557	1054	04/86	1
1158+122	MC2	11 58 22.21	+12 14 00.4	2.018	29	04/86	1
1214+106	MC2	12 14 28.42	+10 36 32.6	1.884	27	04/86	1
1218+339	3C 270.1	12 18 03.89	+33 59 50.1	1.519	889	04/86, 08/83	5
1221+114	MC2	12 21 47.41	+11 23 59.6	1.755	122	04/86	1
1226+105	MC2	12 26 04.61	+10 35 16.4	2.296	222	03/85, 04/86	1
1235−182	MC	12 35 17.12	−18 13 58.2	2.192	105	03/85, 04/86	8
1258+404	3C 280.1	12 58 14.09	+40 25 16.2	1.659	327	04/86	9
1308+182	4C 18.36	13 08 29.47	+18 15 33.8	1.689	133	04/86	1
1311−270	PKS	13 11 02.90	−27 00 55.9	2.195	198	04/86	1
1318+113	4C 11.45	13 18 49.68	+11 22 31.4	2.171	793	03/85	1, 3
1323+655	4C 65.15	13 23 48.49	+65 30 46.6	1.618	196	08/83, 02/85	1
1334+119	MC2	13 34 41.3	+11 55 29	1.760	93	04/86	1
1345+584	4C 58.27	13 45 55.97	+58 27 36.7	2.039	233	02/85, 03/85	1
1354+258	PKS	13 54 48.40	+25 52 00.8	2.032	120	03/85, 04/86	1
1456+092	MC	14 56 56.98	+09 16 01.8	1.991	272	04/86, 08/83	1
1504−164	MC	15 04 04.64	−16 26 21.9	1.790	266	03/85, 04/86	8
1511+103	MC2	15 11 04.5	+10 22 15	1.546	46	04/86	1
1540+180	4C 18.43	15 40 03.62	+18 05 38.3	1.662	294	08/83, 04/86	1
1554−203	MC	15 54 26.13	−20 20 34.8	1.945	65	04/86	1
1557−199	MC	15 57 16.13	−19 59 15.3	1.590	22	04/86	1
1559+173	4C 17.65	15 59 04.63	+17 22 36.5	1.944	299	03/85	1
1602−001	4C −00.63	16 02 22.0	−00 11 01	1.625	420	04/86	1
1602+576	4C 57.27	16 02 53.92	+57 39 01.9	2.850	346	04/86	1
1606+289	4C 28.40	16 06 09.95	+28 56 55.7	1.989	144	03/90	7
1629+120	4C 12.59	16 29 24.51	+12 02 24.4	1.782	734	03/90, 08/83	1
1629+680	4C 68.18	16 29 50.74	+68 03 39.1	2.475	377	03/85	1

TABLE 1—*Continued*

QUASAR	RADIO SOURCE	R.A.(1950)	DEC.(1950)	z	S_{5GHz}	OBS. EPOCH(S)	REFS.
1634+176	MC3	16 34 02.8	+17 41 10	1.897		not observed	1
1658+575	4C 57.29	16 58 53.44	+57 35 52.4	2.173	114	04/86	1
1702+298	4C 29.50	17 02 10.51	+29 51 04.8	1.927	553	08/83	1, 10
1732+160	4C 16.49	17 32 27.87	+16 02 27.3	1.880	312	04/86	1
1816+475	4C 47.48	18 16 58.70	+47 35 26.9	2.225	180	04/86	1
1857+566	4C 56.28	18 57 31.70	+56 41 45.8	1.595	227	04/86	1, 3
2120+168	3C 432	21 20 25.53	+16 51 46.4	1.805	330	04/86	1, 5
2146−133	PKS	21 46 46.35	−13 18 26.4	1.800		not observed	1
2149+212	4C 21.59	21 49 26.11	+21 16 06.9	1.534	376	02/85, 04/86	1
2150+053	4C 05.81	21 50 54.12	+05 22 08.5	1.979	336	04/86, 02/85	1
2156+297	4C 29.64	21 56 27.72	+29 44 46.1	1.753	461	02/85	1
2158+101	4C 10.67	21 58 48.97	+10 09 19.3	1.730	185	04/86, 08/83	1
2209+152	MC3	22 09 07.85	+15 15 38.2	1.502	88	02/85, 04/86	1
2222+051	4C 05.84	22 22 43.50	+05 11 53.4	2.323	253	03/90, 02/85	1
2223+210	PKS	22 23 14.75	+21 02 50.0	1.960	1081	02/85, 04/86	1
2248+192	4C 19.74	22 48 06.19	+19 15 25.1	1.806	265	04/86, 02/85	1
2249+185	3C 454.0	22 49 07.74	+18 32 43.9	1.757	760	04/86	1
2251+244	4C 24.61	22 51 44.32	+24 29 24.7	2.328	855	03/90, 04/86	1
2332+489	OZ 453.7	23 32 17.90	+48 58 44.0	1.534	112	04/86	1
2338+042	4C 04.81	23 38 24.66	+04 14 37.2	2.594	470	02/85	1, 11
2345+061	4C 06.76	23 45 58.40	+06 08 18.7	1.546	341	04/86, 02/85	1
2354+144	4C 14.85	23 54 44.85	+14 29 27.2	1.810	388	04/86, 02/85	1

REFERENCES.—(1) BMSL; (2) Argue & Kenworthy 1972; (3) Lonsdale & Barthel 1987; (4) Warner et al. 1975; (5) Wills 1978; (6) Lonsdale & Barthel 1984; (7) Lonsdale & Barthel 1986a; (8) Murdoch, Hunstead, & White 1984; (9) Jenkins et al. 1977; (10) Lonsdale & Barthel 1986b; (11) Barthel & Lonsdale 1983.

the strength of the correlation, raising the possibility of defining a subsample for the study of source properties which may be particularly sensitive to luminosity or redshift. Figure 5 should furthermore dispel concerns that a correlation of luminosity with redshift will be a major limitation of the sample, although future analysis must take it into account.

4. This sample differs from a simple flux-density limited sample in that flat-spectrum radio sources are excluded. It is widely suspected that flat-spectrum radio cores are strongly Doppler boosted due to bulk relativistic motion within a few parsecs of the central engine, leading to the phenomenon of (often superluminal) core-dominated sources when the flow direction is close to the line of sight (e.g., Kellermann & Pauliny-Toth 1981). It is probable that the optically thin emission, which mostly originates at much greater distances from the central engine, is boosted to a much lesser extent than the core emission, so that flux density limited samples will display an excess of bright, flat-spectrum sources which are oriented close to the line of sight. Our sample, having excluded such sources on the basis of spectral index, should display a more uniform distribution of source axis orientations, and be relatively free

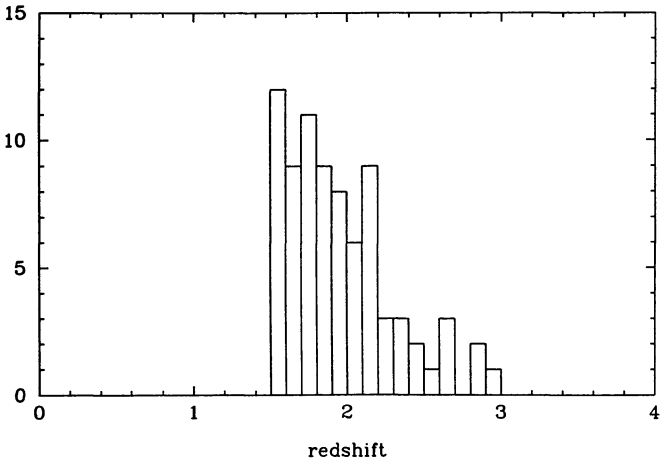

FIG. 1.—Redshift distribution of the steep-spectrum high-redshift QSO sample.

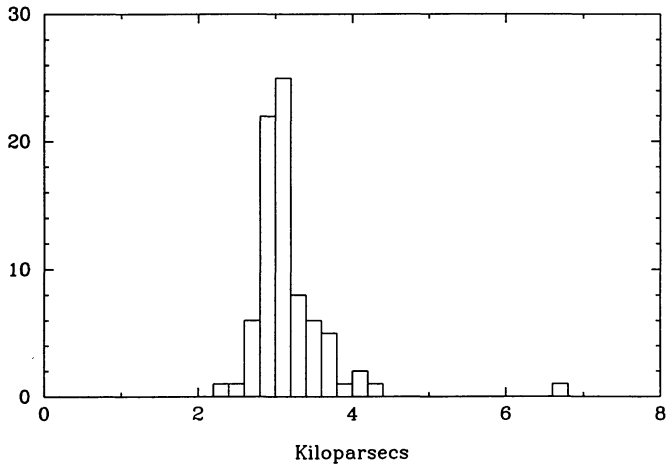

FIG. 2.—Distribution of linear resolution on the 6 cm maps. Sizes correspond to the geometric mean of the major and minor axes of the restoring beam, using $H = 17$ km s^{-1} Mpc^{-1} and $q = 0.05$.

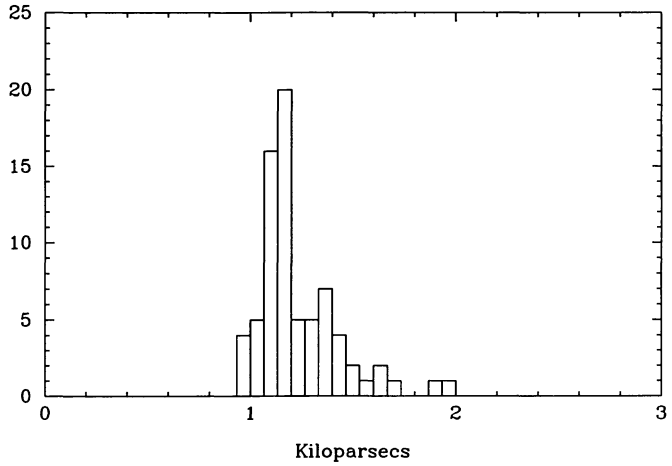

FIG. 3.—Distribution of linear resolution on the 2 cm maps, calculated as in Fig. 2.

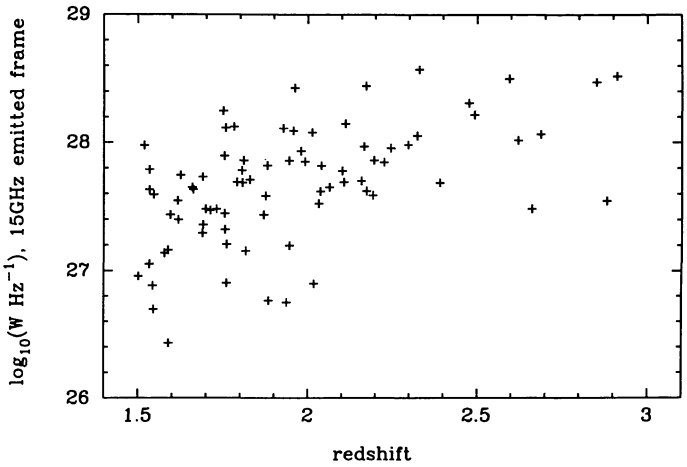

FIG. 5.—Plot of monochromatic source power at 15 GHz emitted frame vs. redshift. A correlation is present, but is much weaker than in most radio source samples (see text).

of many effects arising from close alignment, such as exaggeration of bends in jets, and the like. The exclusion of intrinsically weak flat spectrum sources with strongly boosted cores also preserves the abovementioned sample homogeneity in luminosity. We emphasize that these alignment effects greatly complicate attempts to extract information on physical conditions in radio sources, and can compromise statistical studies.

Hutchings, Price, & Gower (1988), Neff, Hutchings, & Gower (1989), and Neff & Hutchings (1990) have repeatedly (and in our view, incorrectly) criticized the use of a radio spectral index selection criterion in studies of this nature and have used a simple high-frequency radio flux density cutoff to define their samples. However, several of the radiomorphological correlations which appear from these studies can be explained simply by assuming the presence of relativistic beaming in the QSR radio cores. In addition, preferred orientation of core-boosted, closely aligned sources with increasing rest frequency/redshift can be held responsible for observed correlations with redshift.

We recognize that our sample may well not be orientation unbiased. In particular, it has been suggested (Barthel 1989) that all quasars are oriented within ~45° of the line of sight. Also, the optical flux density limit (see item 6 below) may lead to additional mild orientation biases due to geometrical effects when viewing optically thick inclined accretion disks. Nevertheless, our selection criteria should effectively exclude strongly beamed objects very close to the line of sight, thus rendering statistical analyses substantially more tractable. We assert that orientation effects have been minimized by our approach to the extent that is currently feasible, although they cannot be ignored in subsequent analyses.

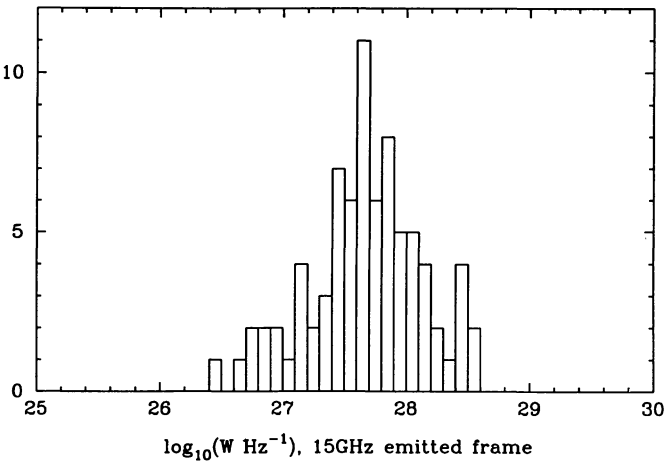

FIG. 4.—Distribution of monochromatic source power at 15 GHz in emitted frame (close to 5 GHz observed frame).

5. The sample is radio flux limited, but is not complete at low flux density levels. This is due to the inclusion of a few sources from the Molonglo and Westerbork surveys, which were of limited sky area. No bias with respect to the properties of the radio sources other than total luminosity is anticipated, although these faint sources are not well represented in the sample.

6. The sample has an effective optical flux density limit, due to the requirement that sources be identified, and their redshifts be measured. In practice, this means that few sources with optical counterparts fainter than 20th magnitude will be included. However, this implicit selection criterion depends only on QSO optical magnitude and not on the detailed radio properties (they were not known at the time), nor on any other optical properties we are aware of that might be related to the radio properties we are examining.

In summary, this sample of early-epoch radio-loud quasars is characterized by narrow distributions of intrinsic and observed source parameters.

3. OBSERVATIONS AND DATA REDUCTION

The sample of 81 steep spectrum quasars was observed with the NRAO Very Large Array (Thompson et al. 1980) in its A-configuration, at 5 and 15 GHz standard frequencies and 50 or 100 MHz bandwidth. The observations were made in snapshot mode during several observing sessions: 1983 August 21–22, 1985 February 26 and March 10, 1986 April 27–29, and 1990 March 22–23. Generally, the fields were observed for 5–8 minutes at 5 GHz, and for 15–20 minutes at 15 GHz. For each

observing session, calibrator sources were typically observed between each program source, and standard phase and amplitude calibration procedures were followed using the DEC-10 computer at the VLA site. Polarization calibration was achieved by the deliberate inclusion of a polarization calibrator source at a wide variety of parallactic angles, and in all cases the solution for the instrumental polarization was excellent. Absolute flux density and polarization position angle calibration was achieved by the inclusion of a scan on 3C 286 for all observing runs.

Data reduction was performed in a uniform, standard manner, using the NRAO Astronomical Image Processing System. Maps were made using Fourier transform and "CLEAN" algorithms as implemented in the AIPS tasks UVMAP and APCLN, or MX, depending on the size of the source. In all cases, extensive self-calibration was employed in an effort to realize the fullest potential of the data. Each map received individual attention, typically involving identification and flagging of bad data points, and between 2 and 12 cycles of self-calibration. The initial self-calibration was restricted to the phase data. Occasionally, especially at 2 cm, phase-only self-calibration proved insufficient, and amplitude self-calibration had to be invoked. Polarization intensity and position angle maps were generated from the Stokes Q and U images using the POLC and POLA options in the AIPS task COMB, the first of which corrects for Ricean bias in the $(Q^2 + U^2)^{1/2}$ polarization intensity image.

There were several instances where the final map quality was judged insufficient for our purposes, most commonly due to poor sensitivity as a result of the lack of cooled 2 cm receivers in the first (1983) observing session, but occasionally due to interference problems, poor synthesized beam shape, or undiagnosed problems with the data. In most such cases, we were able to reobserve the source/frequency combination in question, and obtain satisfactory images. A few 2 cm images from the early, uncooled observations remain, however, and the rms noise on these maps is markedly higher than that for other maps. During the 1986 April run, a period of complete data loss occurred due to a computer crash. As mentioned already, the effects of this data loss are very minor.

The quality of the final maps is summarized in the histograms of rms noise and dynamic range (defined as the peak on the map divided by the rms noise), shown in Figures 6–9. Figures 6 and 7 illustrate the comparable noise levels in the 5 and 15 GHz maps. Similarly, Figures 8 and 9 specify the obtained dynamic range values.

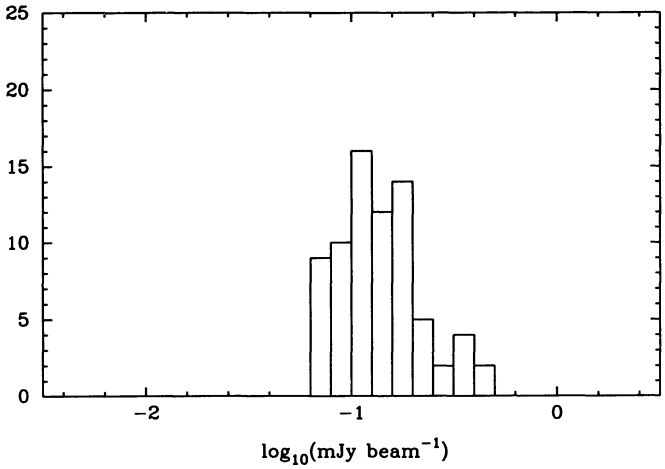

FIG. 7.—Distribution of rms noise on 2 cm maps

Typical noise-limited dynamic ranges are several hundred to 1, while a significant number of images achieve dynamic ranges of over 2000 to 1. The image fidelity is expected to be considerably lower than this, primarily because of the limited, snapshot uv-coverage. We have attempted to estimate the typical fidelity of our images by comparison of our maps to those of others in the few instances where images made from longer VLA integrations are available. Comparison maps may be found for 0802+103 (Kronberg, Perry, & Zukowski 1990), 0017+154, and 2120+168 (Bridle et al. 1993), and 1857+566 (Owen & Puschell 1984). The results of such comparisons are reassuring, and lead us to believe that beyond the known limitations of surface brightness sensitivity and poor or absent rendition of features with two-dimensional extent greater than ~2″ at 2 cm and ~6″ at 6 cm, our images may be used for the reliable extraction of a variety of morphological, flux density, and polarization parameters.

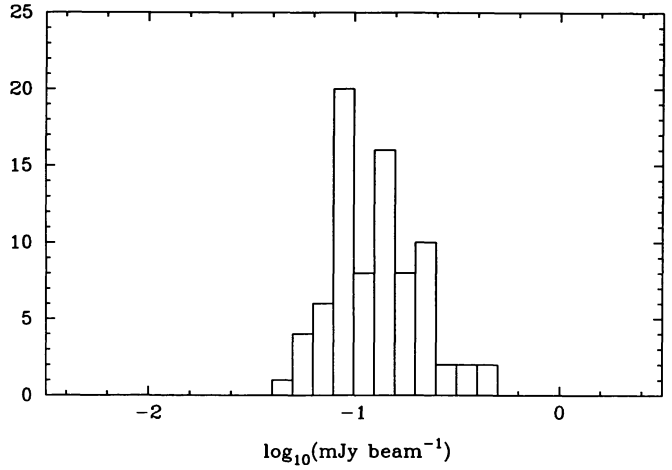

FIG. 6.—Distribution of rms noise on 6 cm maps

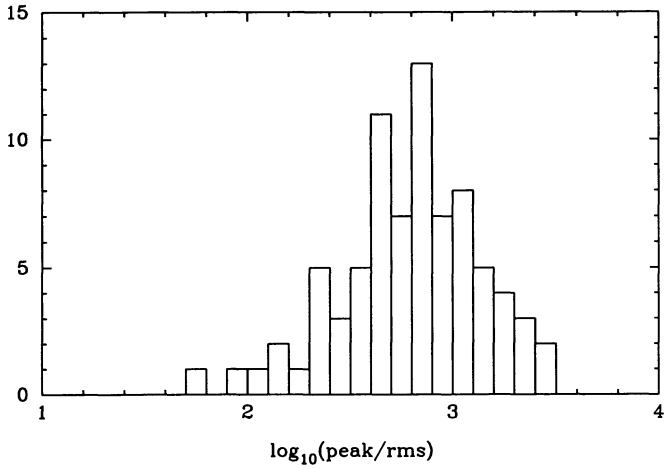

FIG. 8.—Distribution of dynamic range on 6 cm maps

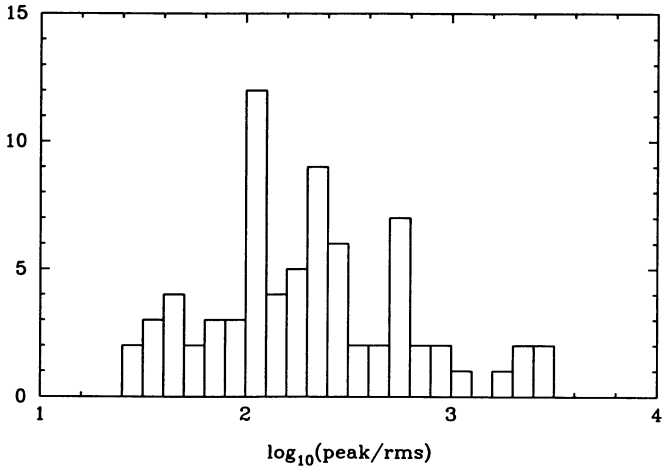

FIG. 9.—Distribution of dynamic range on 2 cm maps

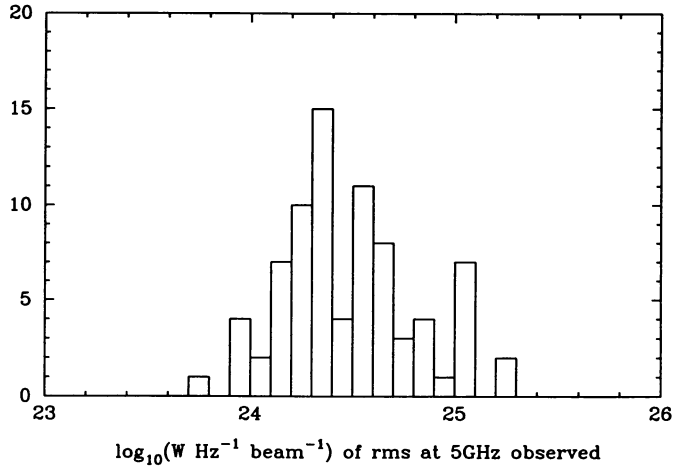

FIG. 10.—Distribution of $P_{\rm noise}$ as defined in the text, for the 6 cm maps. This quantity is a redshift-independent measure of the image sensitivity.

In the case of resolved regions of emission, the surface brightness sensitivity of the 2 cm observations is substantially inferior to that of the 6 cm observations. The synthesized beam is typically a factor of 9 smaller in area, and the steep spectral index of such regions further reduces their detectability at 2 cm. Also, the 6 cm systems at the VLA are intrinsically more sensitive than those at 2 cm. We have somewhat ameliorated these differences by extending the observing time at 2 cm relative to that at 6 cm, but in general, the sensitivity of the 2 cm observations to regions extended on the 6 cm maps is of order 30 times poorer than the 6 cm sensitivity. As a result there are numerous cases in which features that show clearly on the 6 cm maps are not present on the 2 cm maps.

Despite the disparate surface brightness sensitivities between our two frequencies precipitated by our choice of maximum angular resolution, the effective sensitivities of our observations within each band are uniform. One may define a quantity, $P_{\rm noise}$, as the monochromatic power of an unresolved component which would produce a 1σ noise spike on the final image. This "physical noise" constitutes a measure of the sensitivity of our observations to source features of a given size and strength, independent of redshift. In Figures 10 and 11 we show the distributions of this physical noise at 6 and 2 cm. The distributions again indicate that in general our data base will not be strongly biased in the sense of low brightness components falling below the detection threshold in particular subsets of the sample.

Nevertheless, these figures underline the need for caution when interpreting trends based on source properties influenced by the existence or nonexistence of components of surface brightness less than ~ 10 times the rms noise level on the maps. Part of the rationale for conducting 1.4 GHz VLA observations of most of our sources was to guard against inadvertent complete omission of components, with consequent miscalculations of total source extents, arm length ratios, and the like. Inspection of § 4.2 reveals the prudence of this course of action.

Additional information regarding the underestimation or omission of diffuse emission on our maps may be derived by comparison of the integrated flux densities on our 6 cm maps with those in the Becker, White, & Edwards (1991) catalog. This catalog was generated from the 6 cm Greenbank sky survey of Condon, Broderick, & Seielstad (1989), and the flux densities in the catalog are expected to exhibit an rms error not exceeding 10%. The low angular resolution of the survey will ensure that all diffuse emission is included in the catalog value. In Figure 12, we show the distribution of our integrated map flux densities divided by the Becker et al. (1991) values, for the 64 sources in common. This distribution is dominated by a peak of width consistent with the $\sim 10\%$ rms error anticipated from the catalog. This peak, however, is centered close to 0.94, indicating a systematic deficit on our maps, or excess in the Becker et al. values, of order 6%. Furthermore, there are pronounced tails in the distribution to both low and high values, inconsistent with a simple Gaussian distribution. It transpires that five of the eight sources with values of this flux density ratio ≤ 0.8 are of angular extent exceeding 25″, which strongly suggests that in these large sources, substantial amounts of diffuse emission invisible to the A-array of the VLA at 6 cm are present. For the sources in question, this hypothesis is confirmed by inspection of the 20 cm images.

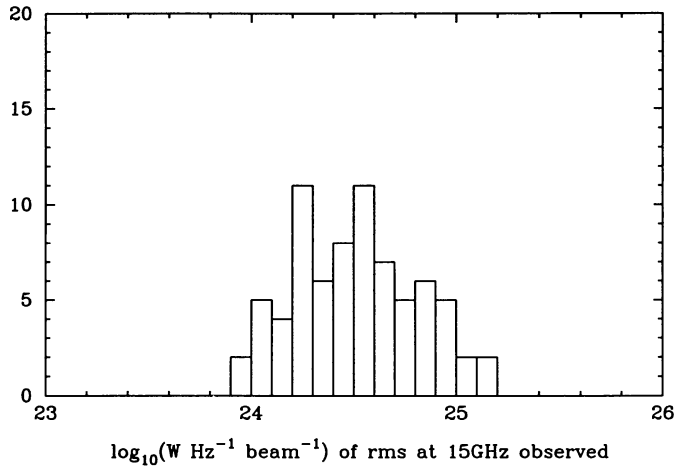

FIG. 11.—Distribution of $P_{\rm noise}$ for the 2 cm maps

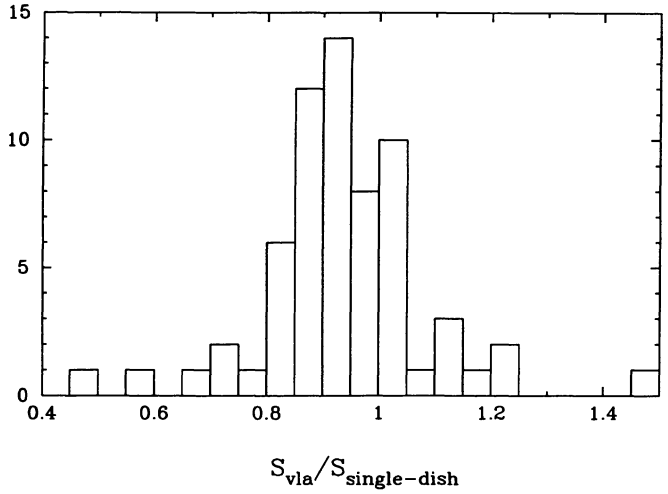

FIG. 12.—Distribution of the ratio of 6 cm VLA-measured flux densities (this paper) to single-dish flux densities (Becker et al. 1991). The bias to values lower than 1.0 and the tails to both high and low values are discussed in the text.

The tail in the distribution to high values is less straightforwardly explained. One possible origin of anomalously high values would be time variability of the core component, but in most of the cases in question, there is insufficient flux density in the core to admit such a hypothesis. It is difficult to envisage a substantial overestimate of the flux density from our images, and we are therefore forced to conclude that a significant subset of the sources in the Becker et al. (1991) catalog suffers from ~20% underestimates of the flux density, for unknown reasons.

The offset of the distribution from unity can be attributed to a variety of causes. The flux density scales used for our data and for the Condon et al. (1989) survey may differ slightly. Confusion from weak sources in the Condon et al. beam may lead to a small but systematic positive offset in the measured values. Our sources may, as a class, possess weak halo emission amounting to a few percent of the total, on scales larger than ~6″. We are unable to distinguish between the various possibilities, but can conclude that no persuasive evidence exists from this comparison that, with the exception of a handful of the largest sources, our images fail to adequately represent important regions of diffuse emission. In conjunction with our 20 cm images, we feel that we are justified in a claim to have imaged essentially all the radio emission associated with these QSRs. The 6 cm images are mostly complete in this sense, while the 2 cm images will be seriously incomplete. It follows, as stated earlier, that comparisons between the 6 and 2 cm images must exclude the more diffuse regions of emission.

4. RESULTS

4.1. *Contour Maps*

We present the results of this study in the form of 167 radio contour maps, with reference to Table 1 (optical positions) and § 4.2 below (notes on individual sources). The contour, restoring beam and polarization scale values are given in the figure captions. The display scale (millimeter per arcsec) is uniform at 6 and 2 cm, and is chosen such that the latter is twice the former. Four large sources are displayed at smaller scale (at 6 cm).

4.2. *Comments on Individual Sources*

0017+154.—Diffuse NW lobe emission is not detected at 15 GHz.

0046−067.—A faint W lobe is detected in our (as yet unpublished) lower resolution 1.4 GHz observations; using an improved position for the optical QSO (Warner et al. 1975) we identify the compact component with the core (although it has a steep radio spectrum): 0046−067 is a double-lobed quasar with overall angular extent of 20″.

0109+176.—Diffuse NW lobe emission is not detected at 15 GHz.

0225−014.—Diffuse SE and NW lobe emission is not detected at 15 GHz; the emission peaks SSW of the W lobe originate in a low surface brightness feature, which is seen in our 1.4 GHz map.

0238+100.—No significant polarized emission detected at 15 GHz.

0316−203.—We do not display maps, since the source is unresolved at 5 and 15 GHz.

0352+123.—Diffuse SE lobe emission is not detected at 15 GHz.

0404+177.—A 1.4 GHz map (1.″5 resolution) reveals low surface brightness emission in the E lobe, as well as a possible weak W lobe; no significant polarized emission was detected at 15 GHz.

0424−131.—We do not display maps, since the source is unresolved at 5 and 15 GHz.

0445+097.—Our previous 5 GHz map (BMSL) was obtained with higher resolution and therefore shows more detail; ~20% of the Becker et al. (1991) single-dish 5 GHz flux density is not represented on the map.

0553−205.—Diffuse emission NW and SE of the core is not detected at 15 GHz.

0730+257.—Diffuse SE lobe emission is not detected at 15 GHz.

0730+659.—We do not display the 15 GHz map, since we only detect point sources at the core and NE hotspot location.

0747+613.—We do not display maps, since the source is unresolved at 5 and 15 GHz.

0758+120.—We do not display the 15 GHz map, since we only detect a point source at the core position.

0836+195.—We have a 1.4 GHz map, which reveals a continuous jet between the core and the N lobe, as well as a diffuse S lobe; ~20% of the Becker et al. (1991) single-dish 5 GHz flux density is not represented on the map.

0856+124.—No significant polarized emission detected at 15 GHz.

0926+117.—Diffuse SW lobe emission is not detected at 15 GHz.

1023+067.—The S lobe has extended emission toward the SW (from 1.4 GHz data); ~30% of the Becker et al. (1991) single-dish 5 GHz flux density is not represented on the map.

1158+122.—We do not display the 15 GHz map, since we only detect a point source at the core location; our 1.4 GHz map reveals a continuous jet between the core and the W lobe, as well as an E lobe.

1214+106.—We lack 15 GHz data; ~50% of the Becker et al. (1991) single-dish 5 GHz flux density is not represented on the map.

1311−270.—Diffuse E lobe emission is not detected at 15 GHz.

1323+655.—Our 1.4 GHz map reveals additional low surface brightness emission NW of the core; ~20% of the Becker et al. (1991) single-dish 5 GHz flux density is not represented on the map.

1334+119.—The features just N of the core on the 5 GHz map represent low surface brightness lobe emission (seen on our 1.4 GHz map).

1345+584.—Diffuse E lobe emission is not detected at 15 GHz.

1354+258.—Diffuse N and S lobe emission is not detected at 15 GHz; our 1.4 GHz map reveals additional low surface brightness emission, and the jet is found to connect to the S lobe.

1456+092.—Faint NE lobe emission is not detected at 15 GHz and was not detected in our previous 5 GHz observations (BMSL).

1511+103.—Our 1.4 GHz map reveals a jet toward the E lobe, as well as an extended, low surface brightness W lobe; no significant polarized emission is detected at 15 GHz; ~30% of the Becker et al. (1991) single-dish 5 GHz flux density is not represented on the map.

1540+180.—Diffuse N and S emission is not detected at 15 GHz; the source has additional faint halo emission (1.4 GHz).

1559+173.—We lack 15 GHz data.

1606+289.—We lack 15 GHz data.

1629+120.—The faint emission W of the core is real; ~20% of the Becker et al. (1991) single-dish 5 GHz flux density is not represented on the map.

1629+680.—We lack 15 GHz data.

1658+575.—We identify the compact component at 57°35′53″.9 with the core (BMSL); additional low surface brightness emission is seen on our 1.4 GHz map.

1816+475.—Diffuse SE lobe emission is not detected at 15 GHz.

1857+566.—Diffuse lobe emission is not detected at 15 GHz; our 1.4 GHz map reveals extensive diffuse emission in both NW and SE lobes; ~30% of the Becker et al. (1991) single-dish 5 GHz flux density is not represented on the map.

2150+053.—Diffuse W lobe emission is not detected at 15 GHz.

2209+152.—Diffuse W lobe emission is not detected at 15 GHz.

2223+210.—Faint SW lobe emission is not detected at 15 GHz and was not detected in our previous 5 GHz observations (BMSL).

2249+185.—We lack 15 GHz data; a high-resolution MERLIN map of this compact steep-spectrum QSR is presented by Spencer et al. (1991).

2332+489.—Low surface brightness lobe emission is detected in our 1.4 GHz data, extending back toward the core from both lobes; ~40% of the Becker et al. (1991) single-dish 5 GHz flux density is not represented on the map.

2354+144.—Diffuse NW lobe emission is not detected at 15 GHz; ~20% of the Becker et al. (1991) single-dish 5 GHz flux density is not represented on the map.

4. DISCUSSION

Visual inspection of the maps presented in this paper allows certain trends to be immediately noticed. There is a startling predominance of strong jets without well-defined terminal hot spots, or, in some cases, lobes. Excellent examples of this phenomenon can be found in 0017+154, 0038−019, 0730+257, 1258+404, 1318+113, 1323+655, 1345+584, and 1857+566. Several sources show terminal features or hot spots that are relatively weak or diffuse (e.g., 0033+081, 0051+291, 1816+475). Some of the jets are responsible for the bulk of the radio emission from the source, raising the disturbing possibility that Doppler boosting of the kiloparsec-scale jet emission has led to an orientation bias in our sample. On the other hand, it has recently become clear that extensive gaseous halos, having masses up to $10^9\ M_\odot$ and sizes up to 100 kpc, exist around high-redshift radio-loud QSOs (Heckman et al. 1991). Turbulent mass entrainment in the QSO jets with rapid bulk flow energy depletion (comparable to what is seen in the jets of low-luminosity radio galaxies, e.g., Bridle 1992), may be responsible for this QSO jet and lobe appearance.

In addition, many of the jets are strongly bent (1857+566, 0038−019, 1345+584, 0941+261, and many others), and as explained by Bridle & Perley (1984) it can be argued that strong Doppler boosting of these jets is unlikely in view of the constancy of their apparent emissivity as the presumed inclination of the flow to the line of sight changes. Such an argument depends on the jets being confined, which seems likely given the Mach numbers implied by a free-jet interpretation of, for example, 1857+566. Consistent with the findings of Barthel & Miley (1988), the subjective impression is one of a large percentage of highly distorted structures, typically as the result of a sharply curved jet.

In cases where jets and strong hot spots coexist in a source, the well-known trend for jetted hotspots to be brighter and more compact than their unjetted counterparts is generally confirmed. There are, however, a few weak counterexamples (e.g., 0802+103 and 1658+575), including some sources with "hot-spot–less" jets whose opposite lobes contain features that could be called "hot spots" (e.g., 0038−019, 1323+655). The relatively weak jets feeding very bright, compact hot spots found frequently in a lower redshift sample of QSRs (Bridle et al. 1993) appear to be infrequent in this high redshift sample.

Comparison of the 6 and 2 cm polarization vectors for various components sometimes reveals evidence of substantial Faraday rotation between the two frequencies, despite the fact that the emitted frequencies are typically 15 and 45 GHz. This is most clearly seen in the hot spots of 0032+423, 0445+097, and 1629+120, the jet of 0802+103, and the cores of 1456+092, 1602+576, and 2251+244, although it is present to a less obvious degree in several other sources and components. If the polarization position angle change is indeed due to Faraday rotation at the source, the implied rotation measures typically exceed 1000 rad m^{-2} in such cases (e.g., Kronberg et al. 1990). If rotation measures of this magnitude were indeed common in this sample, there could be significant implications for the distribution and density of the medium surrounding these high-redshift objects. Careful quantitative comparison of the images, taking into account their differing resolutions, is necessary to measure the position angle differ-

ences, and in the absence of a third frequency, there is no way to resolve turn ambiguities or confirm a λ^2 dependence of the rotation angle. Nevertheless, particularly for jets and hot spots (which are less likely than cores to exhibit strong spectral gradients on unresolvably small scales), Faraday rotation remains the most likely cause of the observed rotations, and these images can place meaningful lower limits on the magnitude of the rotation measures.

A striking aspect of the sample concerns the spectral indices of the core components. Inspection of the peak contours on the 6 and 2 cm maps reveals that most of the unresolved core components have steep spectra, implying the dominance of optically thin components on scales ≥ 1 milliarcsecond (mas) or so. This is somewhat surprising, and atypical of previously studied radio source populations. Some of the explanation may be found in the high emitted frequencies corresponding to these images. It is possible that a significant fraction of all core components become optically thin around a few tens of GHz. Such core components are presumably dominated by milliarcsec-scale jets instead of optically thick jet bases (Blandford & Königl 1979). Certainly, the steepness of the core component is responsible for the inclusion of several sources in our sample (notably 0051+291, 0225−014, 0352+123, and several others), since otherwise the overall source spectral index would not have satisfied our criteria. This again raises the specter of orientation bias, since milliarcsec-scale beams in powerful sources are generally considered to be moving relativistically. Any statistical analysis of the sample must consider the likelihood of a modest degree of orientation bias in the sample.

There are 21 sources (27%) in the sample of angular extent $\lesssim 2''$, which may be generically referred to as compact steep-spectrum (CSS) sources. This represents a sizable fraction of the steep-spectrum, high-z QSR population, but the occurrence is comparable to that found at lower redshifts (Fanti et al. 1990). Small-scale jets and hot spots are often seen in these sources (e.g., 0032+423, 0044−055, 0445+097, 0751+298, 0843+136, 0848+155, 0856+124, 0941+261, 1153+317, and several others). With reference to a previous paragraph, the incidence rate of high rotation measure values among CSS sources appears to be high (in agreement with Taylor, Inoue, & Tabara 1992).

Our approach toward the quantitative analysis of these images will be to extract a variety of parameters for each identifiable component of each source, such as total flux density, angular extent, sky coordinates, polarized intensity and position angle, spectral index, frequency dependence of polarization parameters, and the like. Parameters depending on comparison between maps at the two frequencies will be derived from images convolved to the same angular resolution. Size and position parameters will be combined to produce morphological parameters for the source, such as bending angle, total angular size, arm length ratio, jet opening angles, and so on. Upon completion of this parameter extraction, a search will be conducted for relationships between numerous pairs of parameters in order to gain physical insight into radio source processes and orientation effects. Clearly, there will be many instances where parameters are unmeasurable or simply absent, and many more where the information will consist of an upper or lower limit. Under these circumstances, effective utilization of the data will dictate the use of the statistical techniques of survival analysis (Feigelson & Nelson 1985). In addition, despite the unusual properties of our sample as described in § 2, some selection effects and biases remain, which will require careful examination before the intrinsic nature of any parameter relationship is claimed. We believe that our sample is sufficiently well understood for this to be an achievable goal. The details of the parameter extraction and statistical analysis process, now underway, will be reported in subsequent papers.

We thank the VLA staff, in particular B. Clark, P. Perley, and D. Wunker, for help with the observations, and A. H. Bridle for carrying out some 15 GHz observations. We thank W. Bogers for assistance in various aspects of the final assembly of this paper. The NRAO VLA is operated by Associated Universities, Inc., under contract with the National Science Foundation. Research at Haystack Observatory is sponsored by the National Science Foundation, through the Northeast Radio Observatory Corporation. C.J.L. acknowledges support from NSF grants AST81-01204 and AST83-51447 to the Pennsylvania State University, where part of this work was conducted. P.D.B. acknowledges support by the Royal Netherlands Academy of Arts and Sciences, as well as NSF support through the Owens Valley Radio Observatory. G.K.M. acknowledges research grants from NATO and the European Economic Community.

REFERENCES

Argue, A. N., & Kenworthy, C. M. 1972, MNRAS, 160, 197
Baade, W., & Minkowski, R. 1954, ApJ, 119, 206
Barthel, P. D. 1983, A&A, 126, 16
———. 1989, ApJ, 336, 606
Barthel, P. D., & Lonsdale, C. J. 1983, MNRAS, 205, 395
Barthel, P. D., & Miley, G. K. 1988, Nature, 333, 319
Barthel, P. D., Miley, G. K., Schilizzi, R. T., & Lonsdale, C. J. 1988, A&AS, 73, 515 (BMSL)
Barthel, P. D., Miley, G. K., Schilizzi, R. T., & Preuss, E. 1984, A&A, 140, 399
Becker, R. H., White, R. L., & Edwards, A. L. 1991, ApJS, 75, 1
Blandford, R. D. 1990, in Active Galactic Nuclei (Saas Fee Advanced Course 20), ed. T. J.-L. Courvoisier & M. Mayor (Heidelberg Springer), 161
Blandford, R. D., & Königl, A. 1979, ApJ, 232, 34
Bogers, W. J., et al. 1993, in preparation
Bridle, A. H. 1992, in The AGN Paradigm, ed. S. S. Holt, S. G. Neff, & C. M. Urry (New York: AP), 386
Bridle, A. H., & Eilek, J. A. ed. 1984, Physics of Energy Transport in Extragalactic Radio Sources (Green Bank: NRAO)
Bridle, A. H., & Perley, R. A. 1984, ARA&A, 22, 319
Bridle, A. H., et al. 1993, in preparation
Carilli, C. L., Perley, R. A., Dreher, J. W., & Leahy, J. P. 1991, ApJ, 383, 554
Clark, B. G., Kellermann, K. I., Bare, C. C., Cohen, M. H., & Jauncey, D. L. 1968, ApJ, 153, 705
Condon, J. J., Broderick, J. J., & Seielstad, G. A. 1989, AJ, 97, 1064
Dent, W. A. 1965, Science, 148, 1458
Eilek, J. A., & Hughes, P. A. 1991, in Beams and Jets in Astrophysics ed. P. A. Hughes (Cambridge Univ. Press)
Fanaroff, B. L., & Riley, J. M. 1974, MNRAS, 167, 31P
Fanti, R., et al. 1990, A&A, 231, 333
Feigelson, E. D., & Nelson, P. I. 1985, ApJ, 293, 192
Garrington, S. T., & Conway, R. G. 1991, MNRAS, 250, 198
Garrington, S. T., Leahy, J. P., Conway, R. G., & Laing, R. A. 1988, Nature, 331, 147

Heckman, T. M., Lehnert, M. D., Van Breugel, W., & Miley, G. K. 1991, ApJ, 368, 28
Hewitt, A., & Burbidge, G. 1987, ApJS, 63, 1
Hogg, D. E. 1969, ApJ, 155, 1099
Hogg, D. E., Macdonald, G. H., Conway, R. G., & Wade, C. M. 1969, AJ, 74, 1206
Hughes, P. A. ed. 1991, Beams and Jets in Astrophysics (Cambridge Univ. Press)
Hutchings, J. B., Price, R., & Gower, A. C. 1988, ApJ, 329, 122
Kapahi, V. K. 1989, AJ, 97, 1
Kellermann, K. I., Clark, B. G., Niell, A. E., & Shaffer, D. B. 1975, ApJ, 197, L113
Kellermann, K. I., & Pauliny-Toth, I. I. K. 1981, ARA&A, 19, 373
Kollgaard, R. I., Wardle, J. F. C., & Roberts, D. H. 1990, AJ, 100, 1057
Kronberg, P. P., Perry, J. J., & Zukowski, E. L. H. 1990, ApJ, 355, L31
Laing, R. A. 1988, Nature, 331, 149
Laing, R. A., Riley, J., & Longair, M. 1983, MNRAS, 204, 151
Liu, R., Pooley, G. 1991, MNRAS, 253, 669
Liu, R., Pooley, G., & Riley, J. M. 1992, MNRAS, 257, 545
Longair, M., & Riley, J. 1979, MNRAS, 188, 625
Lonsdale, C. J., & Barthel, P. D. 1984, A&A, 135, 45
Lonsdale, C. J., & Barthel, P. D. 1986a, AJ, 92, 12
———. 1986b, ApJ, 303, 617
———. 1987, AJ, 94, 1487
Macdonald, G. H., Kenderdine, S., & Neville, A. C. 1968, MNRAS, 138, 259
Maltby, P., & Moffet, A. T. 1963, ApJS, 7, 141
McCarthy, P. J., Van Breugel, W., & Kapahi, V. K. 1991, ApJ, 371, 478
Miley, G. K. 1968, Nature, 218, 933
———. 1971, MNRAS, 152, 477
Miley, G. K. 1980, ARA&A, 18, 165
Miley, G. K., & Wade, C. M. 1971, Astrophys. Lett., 8, 11
Murdoch, H. S., Hunstead, R. W., & White, G. L. 1984, Proc. Astron. Soc. Australia, 5, 341
Neff, S. G., & Hutchings, J. B. 1990, AJ, 100, 1441
Neff, S. G., Hutchings, J. B., & Gower, A. C. 1989, AJ, 97, 1291
Norman, M. L., Winkler, K.-H., Smarr, L. L., & Smith, M. D. 1982, A&A, 113, 187
O'Dea, C. P., Barvainis, R., & Challis, P. M. 1988, AJ, 96, 435
Oort, M. J. A. 1987, Ph. D. thesis, Univ. of Leiden
Orr, M. J. L., & Browne, I. W. A. 1982, MNRAS, 200, 1067
Owen, F. N. 1986, in IAU Symp. 119, Quasars, ed. G. Swarup & V. K. Kapahi (Dordrecht: Reidel), 173
Owen, F. N., & Puschell, J. J. 1984, AJ, 89, 932
Padovani, P., & Urry, C. M. 1991, ApJ, 387, 449
Potash, R. I., & Wardle, J. F. C. 1979, ApJ, 239, 42
Sandage, A. 1960, S&T, 21, 148
Schilizzi, R. T. 1976, AJ, 81, 946
Schmidt, M. 1963, Nature, 197, 1040
Spencer, R. E., et al. 1991, MNRAS, 250, 225
Taylor, G. B., Inoue, M., & Tabara, H. 1992, A&A, 264, 421
Thompson, A. R., Clark, B. G., Wade, C. M., & Napier, P. J. 1980, ApJS, 44, 151
Van Breugel, E. J. M., & Miley, G. K. 1977, Nature, 265, 315
Wardle, J. F. C., & Miley, G. K. 1974, A&A, 30, 305
Warner, J. W., Assousa, G. E., Balick, B., & Craine, E. 1975, PASP, 87, 103
Weinberg, S. 1972, Gravitation and Cosmology (New York: Wiley)
Willis, A. G., Strom, R. G., & Wilson, A. S. 1974, Nature, 250, 625
Wills, D. 1978, MNRAS, 184, 559

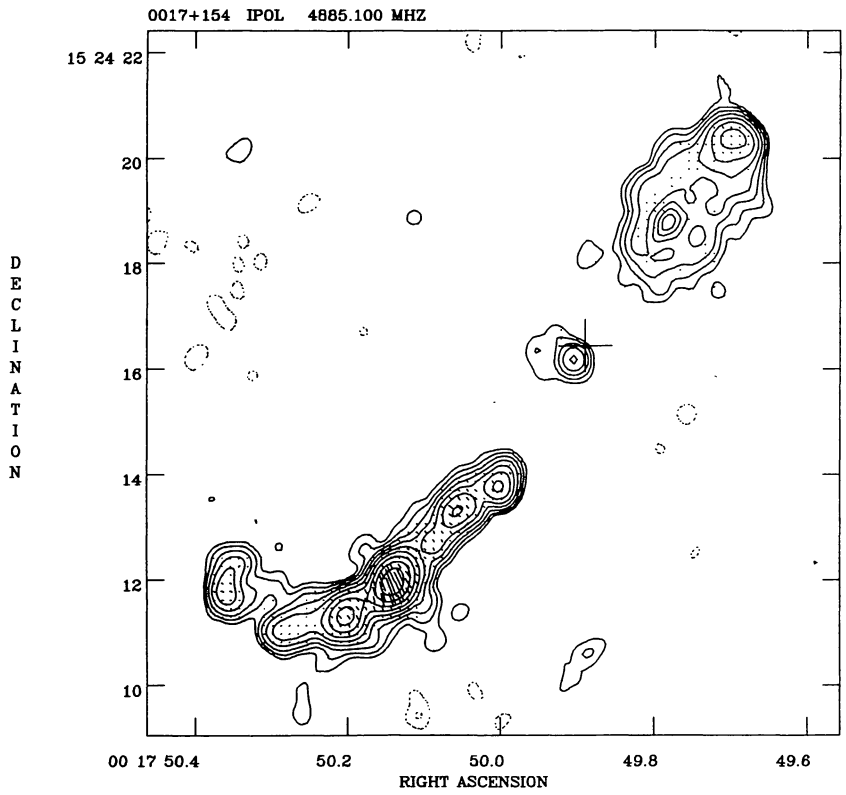

FIG. 13.—0017+154 at 5 GHz; contours $0.2 \times (-1, 1, 2, 4, 8, \cdots)$ mJy beam^{-1}; restoring beam $0''.39 \times 0''.35$ in P.A. 4°.6; polarization vector scale 50 mJy beam^{-1} arcsec^{-1}.

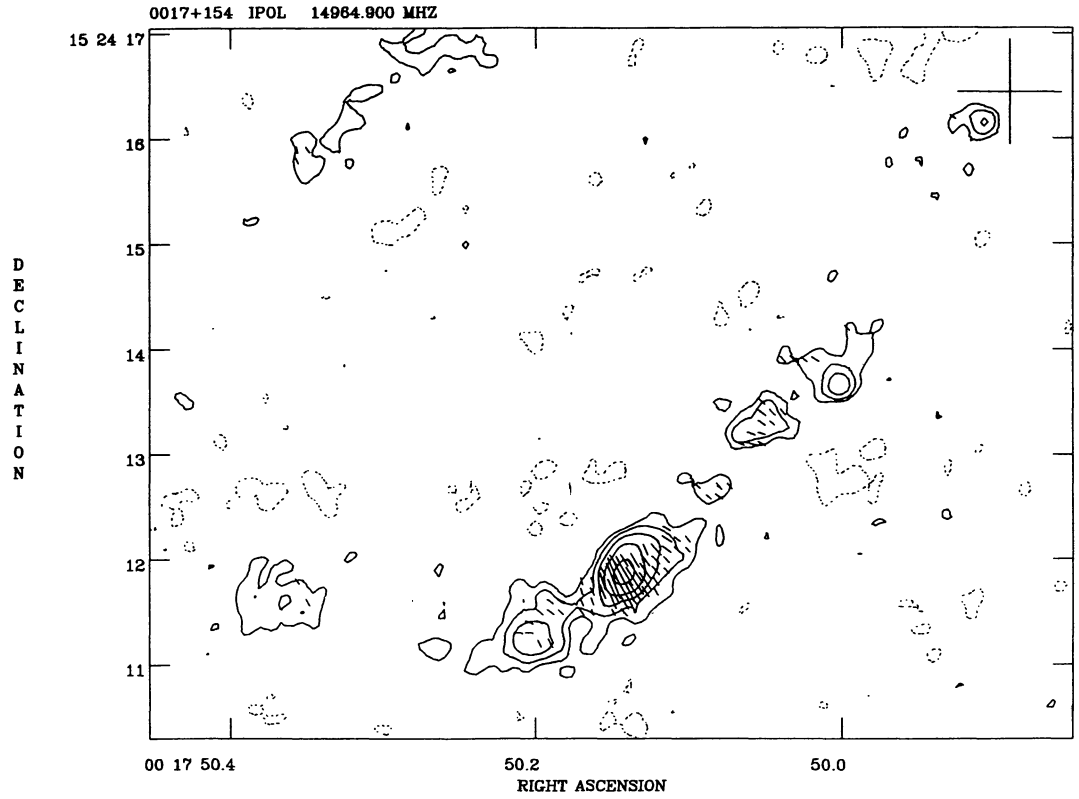

FIG. 14.—0017+154 at 15 GHz; contours $1.0 \times (-1, 1, 2, 4, 8, \cdots)$ mJy beam^{-1}; restoring beam $0''.18$; polarization vector scale 10 mJy beam arcsec^{-1}

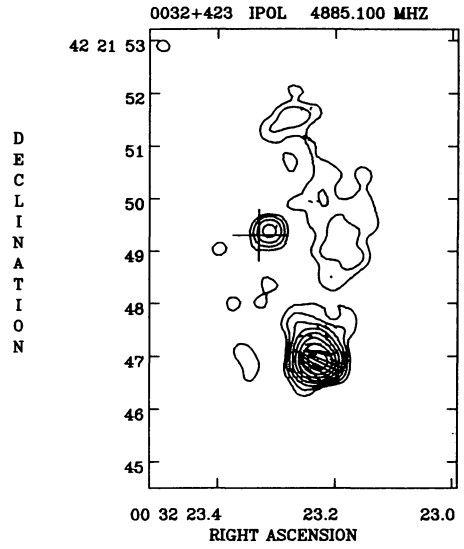

FIG. 15.—0032+423 at 5 GHz; contours $0.3 \times (-1, 1, 2, 4, 8, \cdots)$ mJy beam^{-1}; restoring beam $0''.38 \times 0''.35$ in P.A. 64°; polarization vector scale 5 mJy beam^{-1} arcsec^{-1}.

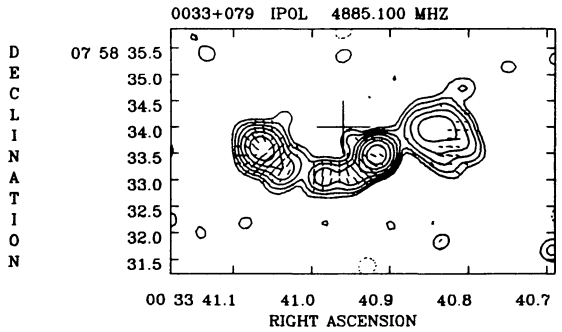

FIG. 16.—0032+423 at 15 GHz; contours $0.3 \times (-1, 1, 2, 4, 8, \cdots)$ mJy beam^{-1}; restoring beam $0''.14$; polarization vector scale 10 mJy beam^{-1} arcsec^{-1}.

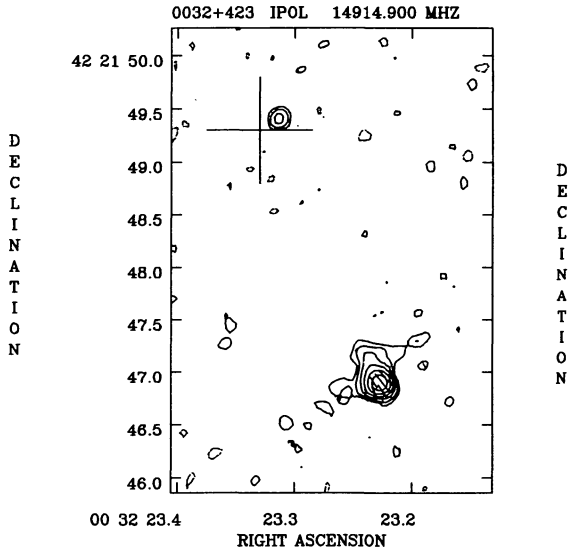

FIG. 17.—0033+079 at 5 GHz; contours $0.3 \times (-1, 1, 2, 4, 8, \cdots)$ mJy beam^{-1}; restoring beam $0''.37$; polarization vector scale 5 mJy beam^{-1} arcsec^{-1}.

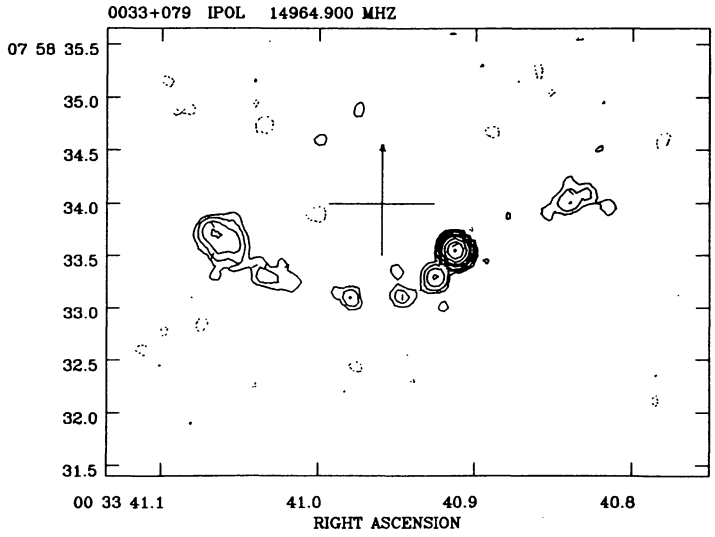

FIG. 18.—0033+079 at 15 GHz; contours $0.2 \times (-1, 1, 2, 4, 8, \cdots)$ mJy beam^{-1}; restoring beam $0''.15 \times 0''.14$ in P.A. 23°; polarization vector scale 5 mJy beam^{-1} arcsec^{-1}.

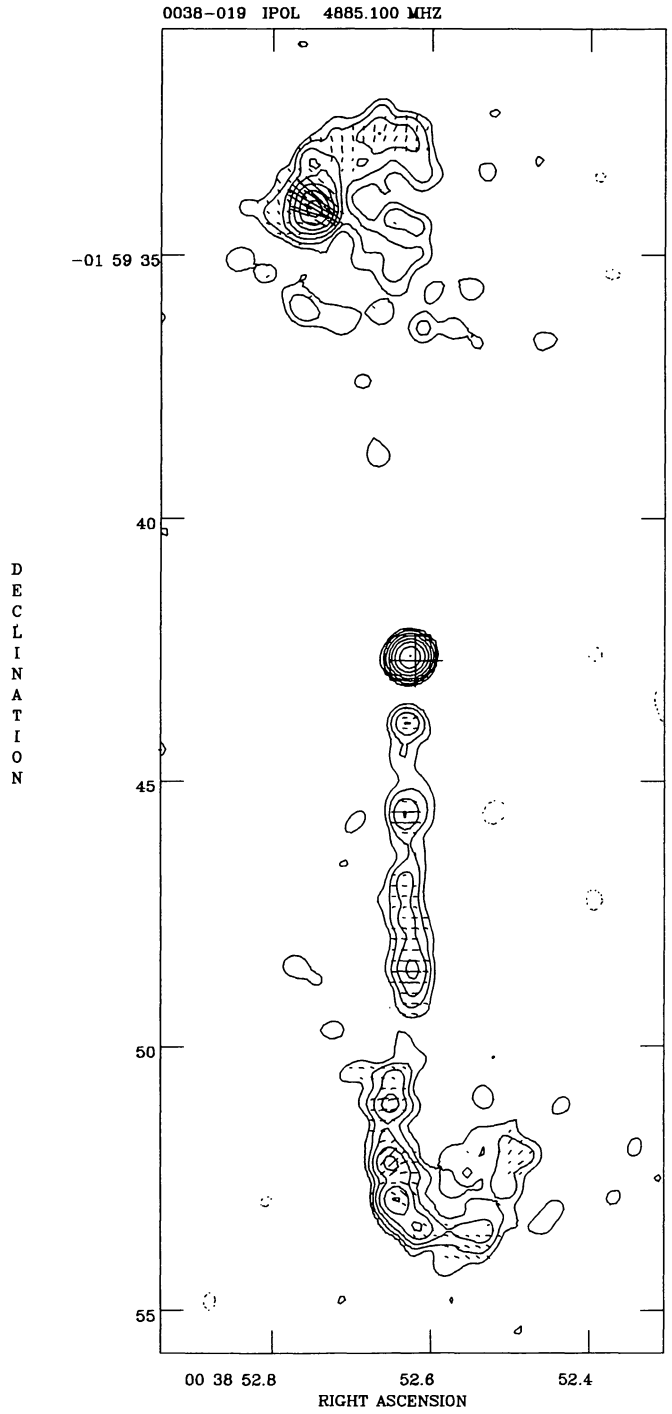

FIG. 19.—0038−019 at 5 GHz; contours 0.45 × (−1, 1, 2, 4, 8, · · ·) mJy beam^{-1}; restoring beam 0″.39 × 0″.38 in P.A. −42°; polarization vector scale 5 mJy beam^{-1} arcsec^{-1}.

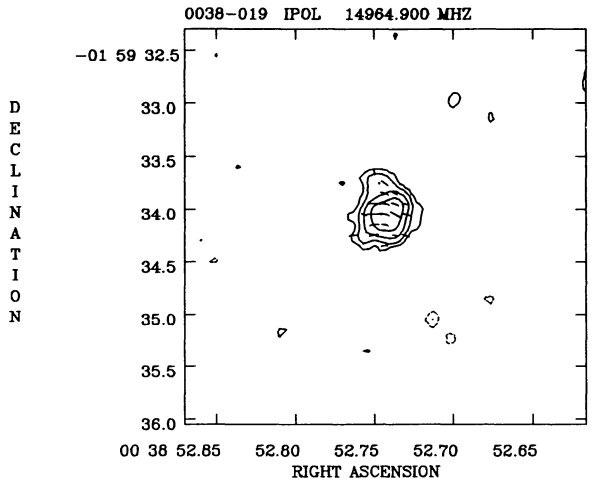

FIG. 20.—0038−019 at 15 GHz; contours 0.2 × (−1, 1, 2, 4, 8, · · ·) mJy beam^{-1}; restoring beam 0″.17 × 0″.14 in P.A. 13°; polarization vector scale 5 mJy beam^{-1} arcsec^{-1}.

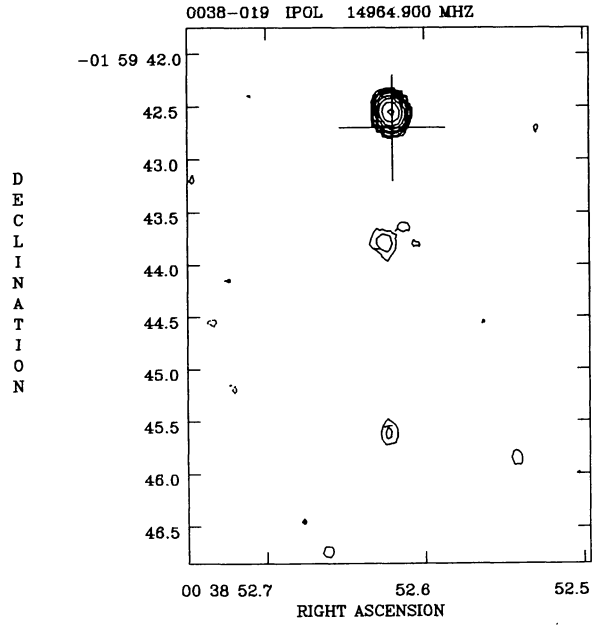

FIG. 21.—Same as Fig. 20

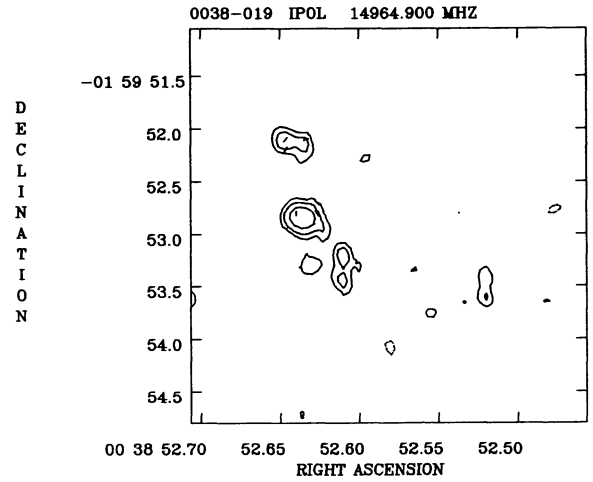

FIG. 22.—Same as Fig. 20

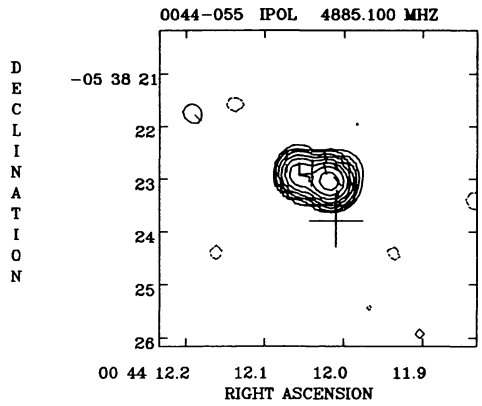

FIG. 23.—0044−055 at 5 GHz; contours 0.45 × (−1, 1, 2, 4, 8, · · ·) mJy beam^{-1}; restoring beam 0″.42 × 0″.39 in P.A. 34°; polarization vector scale 2 mJy beam^{-1} arcsec^{-1}.

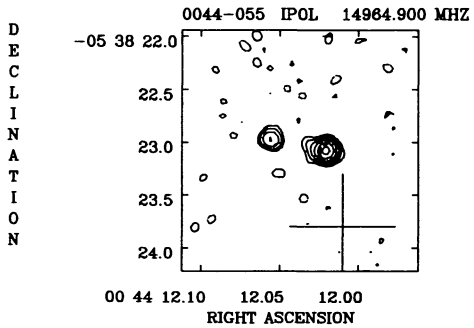

FIG. 24.—0044−055 at 15 GHz; contours 0.6 × (−1, 1, 2, 4, 8, · · ·) mJy beam^{-1}; restoring beam 0″.13 × 0″.11 in P.A. −31°; polarization vector scale 10 mJy beam^{-1} arcsec^{-1}.

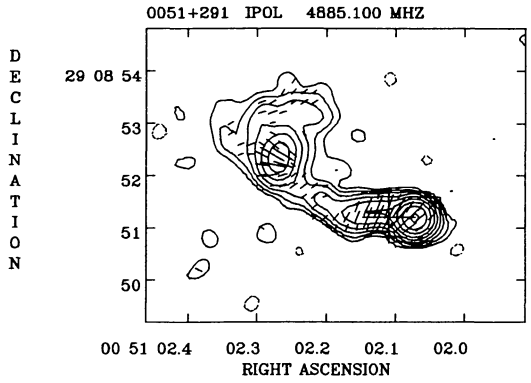

FIG. 25.—0051+291 at 5 GHz; contours 0.45 × (−1, 1, 2, 4, 8, · · ·) mJy beam^{-1}; restoring beam 0″.40; polarization vector scale 5 mJy beam^{-1} arcsec^{-1}.

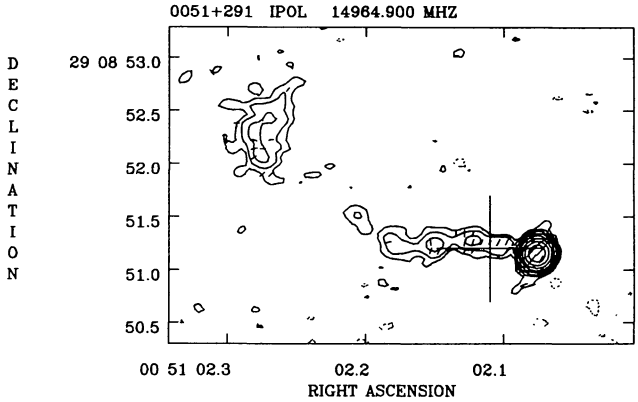

FIG. 26.—0051+291 at 15 GHz; contours 0.6 × (−1, 1, 2, 4, 8, · · ·) mJy beam^{-1}; restoring beam 0″.16; polarization vector scale 10 mJy beam^{-1} arcsec^{-1}.

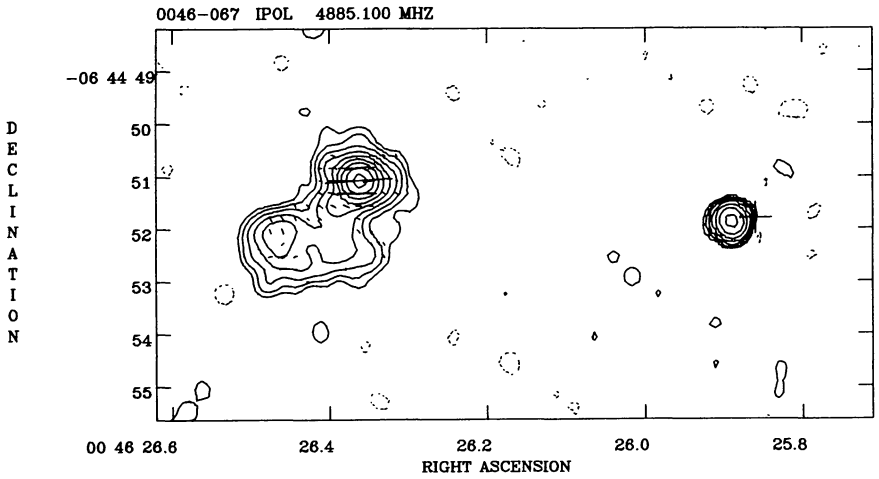

FIG. 27.—0046−067 at 5 GHz; contours $0.2 \times (-1, 1, 2, 4, 8, \cdots)$ mJy beam^{-1}; restoring beam 0″.42 × 0″.36 in P.A. 19°; polarization vector scale 5 mJy beam^{-1} arcsec^{-1}.

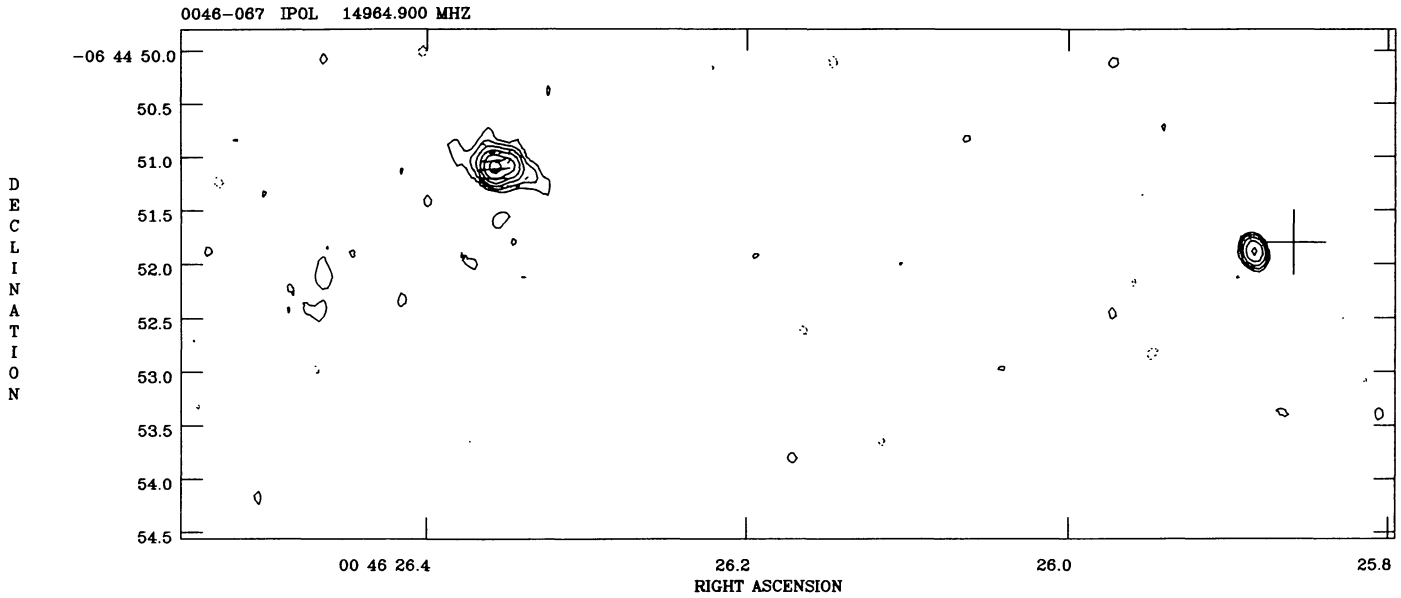

FIG. 28.—0046−067 at 15 GHz; contours $0.3 \times (-1, 1, 2, 4, 8, \cdots)$ mJy beam^{-1}; restoring beam 0″.18 × 0″.14 in P.A. 15°; polarization vector scale 10 mJy beam^{-1} arcsec^{-1}.

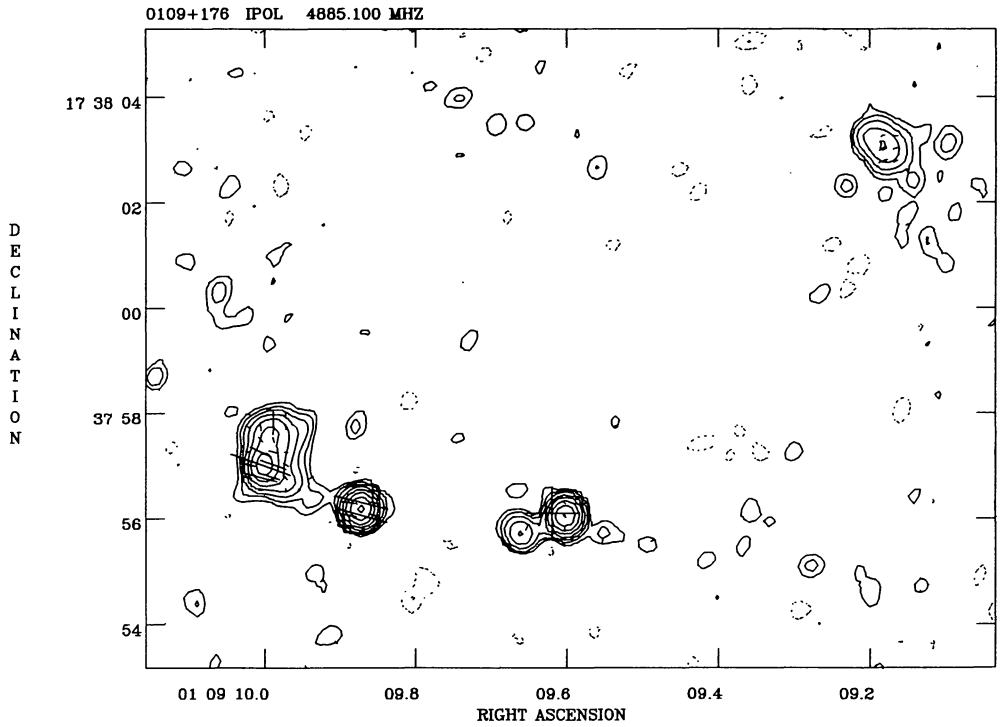

FIG. 29.—0109+176 at 5 GHz; contours $0.2 \times (-1, 1, 2, 4, 8, \cdots)$ mJy beam^{-1}; restoring beam $0''.38 \times 0''.34$ in P.A. 6°; polarization vector scale 5 mJy beam^{-1} arcsec^{-1}.

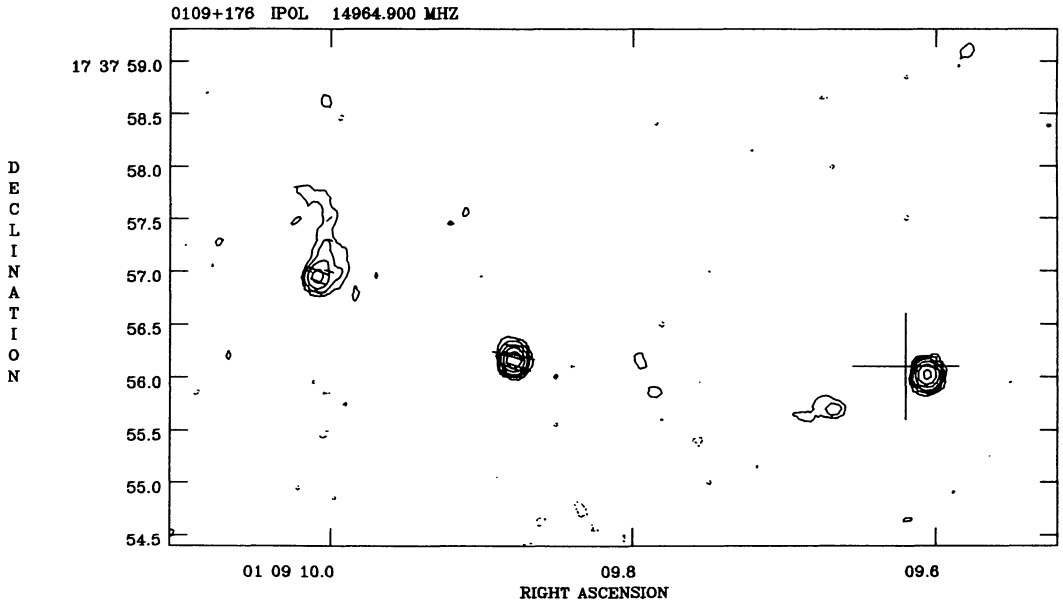

FIG. 30.—0109+176 at 15 GHz; contours $0.3 \times (-1, 1, 2, 4, 8, \cdots)$ mJy beam^{-1}; restoring beam $0''.15 \times 0''.14$ in P.A. 19°; polarization vector scale 5 mJy beam^{-1} arcsec^{-1}.

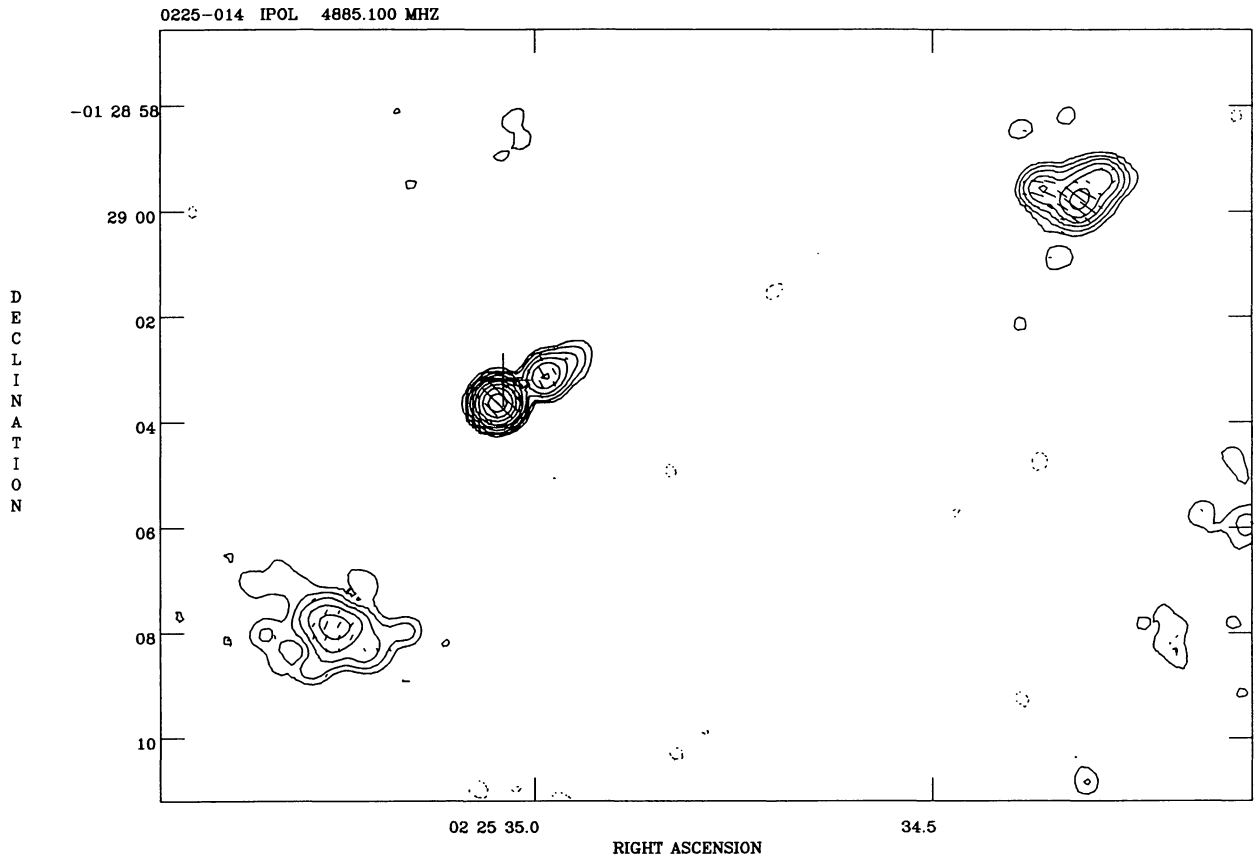

FIG. 31.—0225−014 at 5 GHz; contours $0.2 \times (-1, 1, 2, 4, 8, \cdots)$ mJy beam^{-1}; restoring beam 0.″42; polarization vector scale 5 mJy beam^{-1} arcsec^{-1}

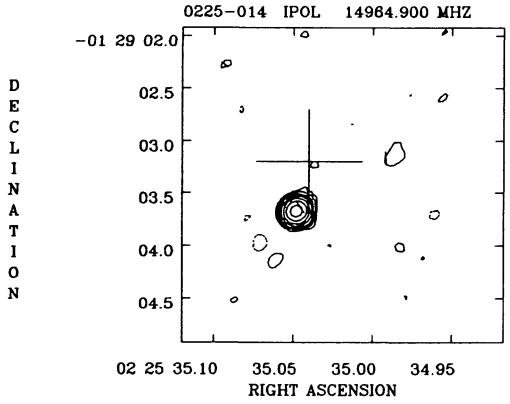

FIG. 32.—0225−014 at 15 GHz; contours $1.0 \times (-1, 1, 2, 4, 8, \cdots)$ mJy beam^{-1}; restoring beam 0.″15; polarization vector scale 10 mJy beam^{-1} arcsec^{-1}

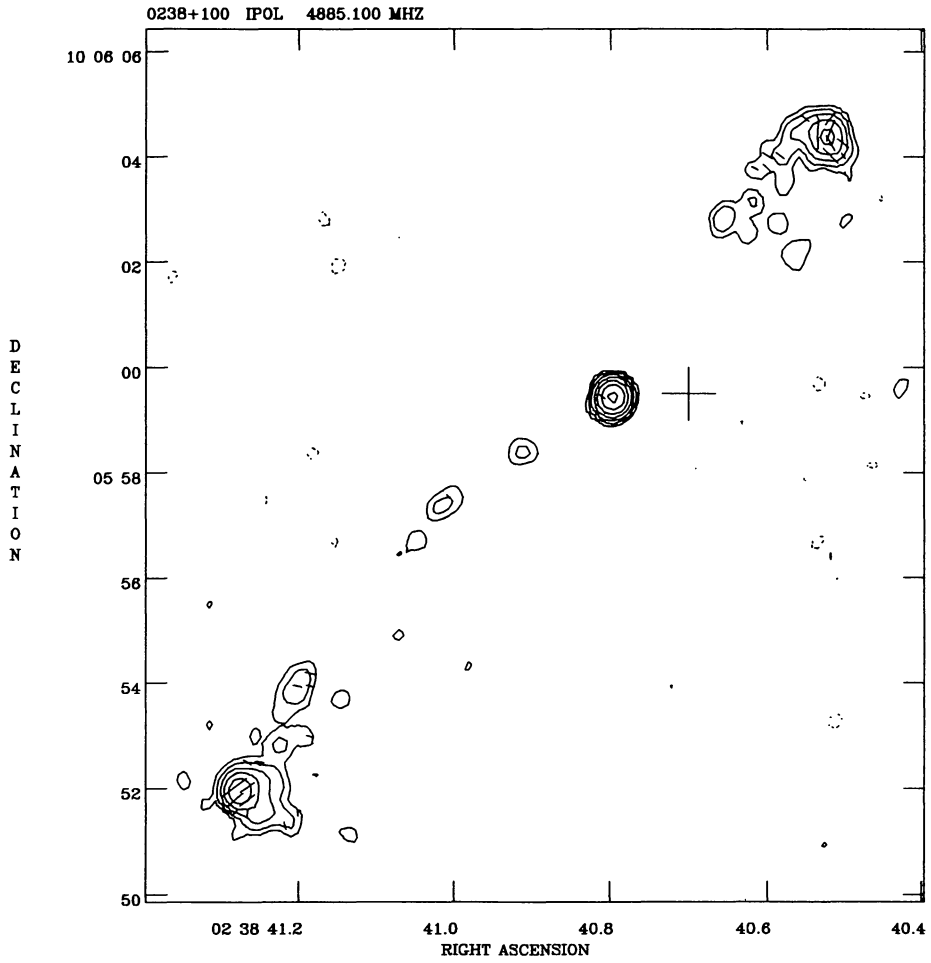

FIG. 33.—0238+100 at 5 GHz; contours $0.3 \times (-1, 1, 2, 4, 8, \cdots)$ mJy beam^{-1}; restoring beam $0''.40 \times 0''.36$ in P.A. 13°; polarization vector scale 2 mJy beam^{-1} arcsec^{-1}.

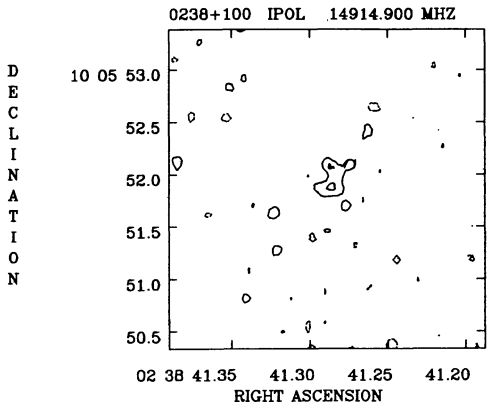

FIG. 34.—0238+100 at 15 GHz; contours $0.3 \times (-1, 1, 2, 4, 8, \cdots)$ mJy beam^{-1}; restoring beam $0''.15 \times 0''.13$ in P.A. 17°.

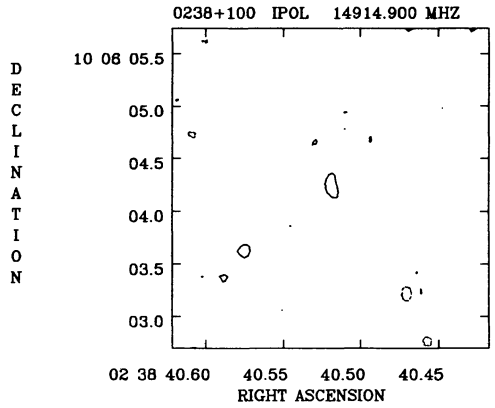

FIG. 35.—Same as Fig. 34

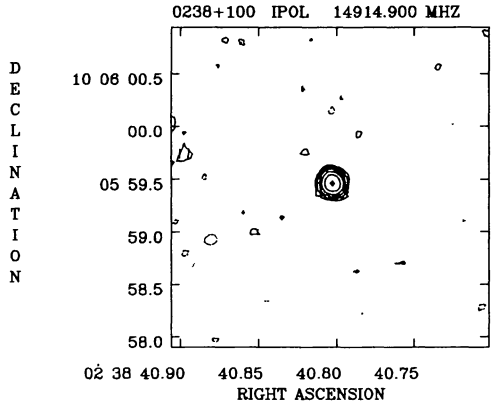

FIG. 36.—0238+100 at 15 GHz; contours $0.3 \times (-1, 1, 2, 4, 8, \cdots)$ mJy beam^{-1}; restoring beam $0''.15 \times 0''.13$ in P.A. 17°

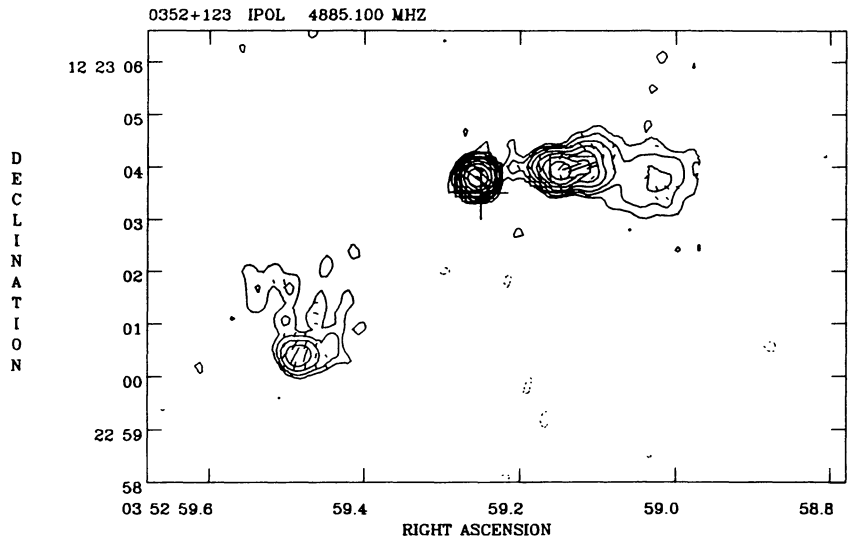

FIG. 37.—0352+123 at 5 GHz; contours $0.45 \times (-1, 1, 2, 4, 8, \cdots)$ mJy beam^{-1}; restoring beam $0''.35$; polarization vector scale 5 mJy beam^{-1} arcsec^{-1}

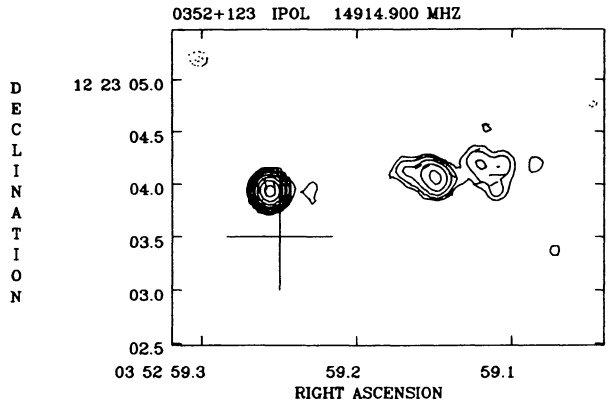

FIG. 38.—0352+123 at 15 GHz; contours $0.6 \times (-1, 1, 2, 4, 8, \cdots)$ mJy beam^{-1}; restoring beam $0''.16 \times 0''.15$ in P.A. 18°; polarization vector scale 10 mJy beam^{-1} arcsec^{-1}.

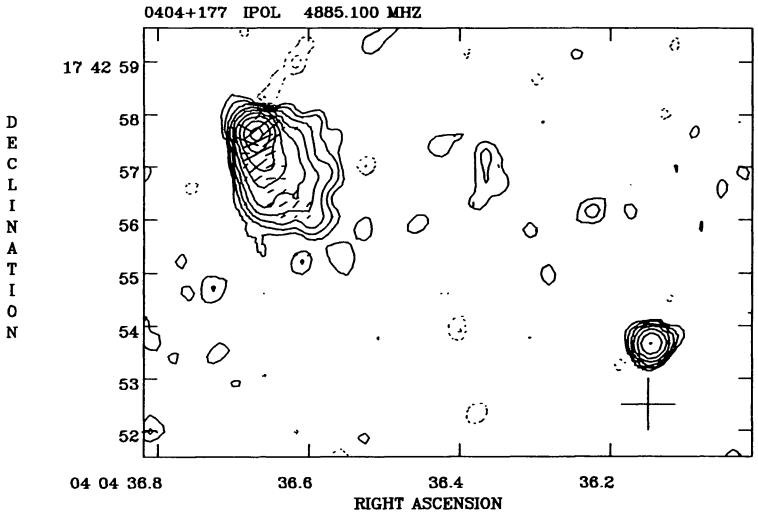

FIG. 39.—0404+177 at 5 GHz; contours $0.2 \times (-1, 1, 2, 4, 8, \cdots)$ mJy beam^{-1}; restoring beam 0.″38 × 0.″35 in P.A. 0°; polarization vector scale 5 mJy beam^{-1} arcsec^{-1}.

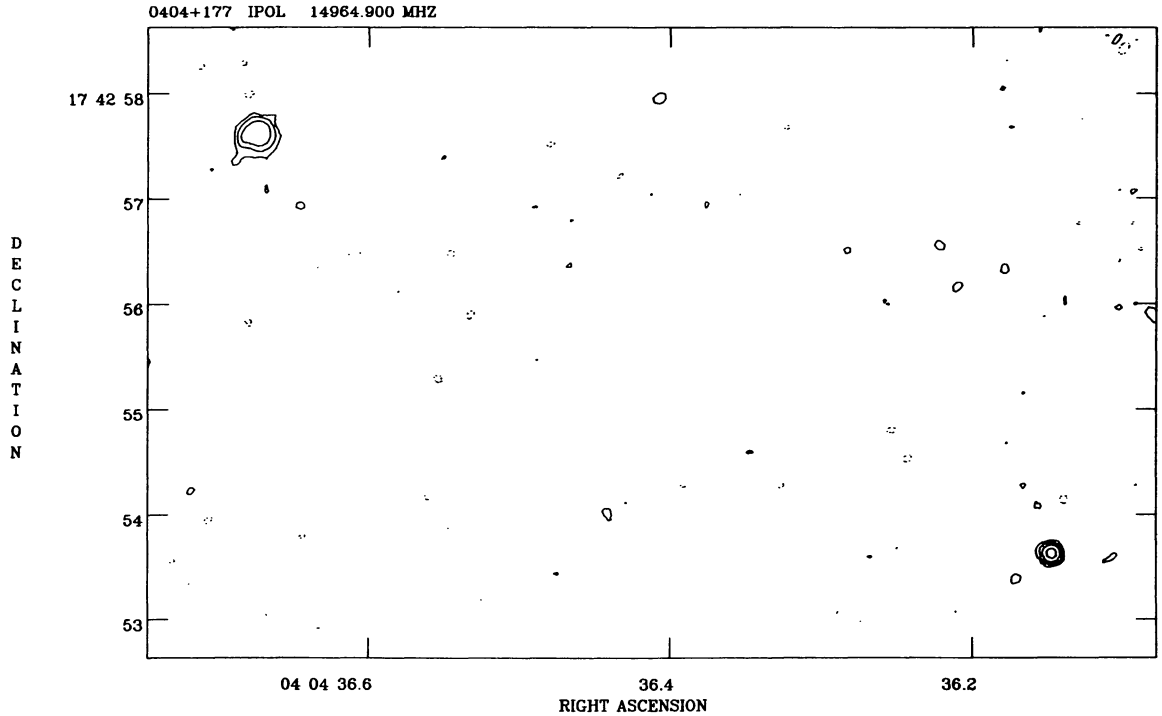

FIG. 40.—0404+177 at 15 GHz; contours $1.0 \times (-1, 1, 2, 4, 8, \cdots)$ mJy beam^{-1}; restoring beam 0.″13

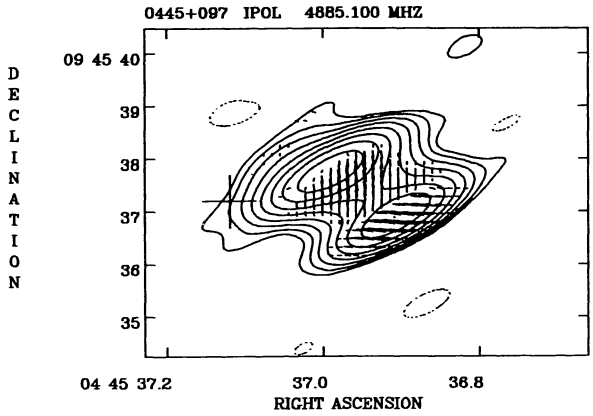

FIG. 41.—0445+097 at 5 GHz; contours $1.0 \times (-1, 1, 2, 4, 8, \cdots)$ mJy beam^{-1}; restoring beam $0''.45 \times 0''.49$ in P.A. $-61°$; polarization vector scale 10 mJy beam^{-1} arcsec^{-1}.

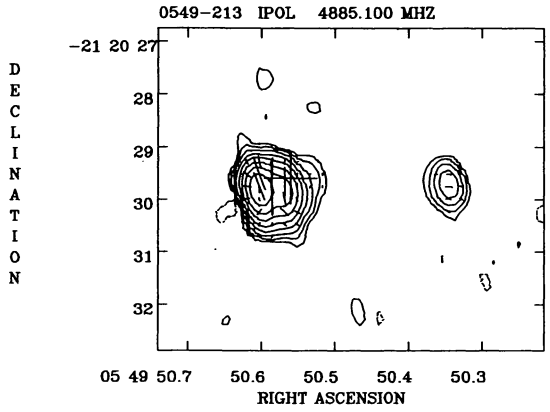

FIG. 42.—0445+097 at 15 GHz; contours $0.45 \times (-1, 1, 2, 4, 8, \cdots)$ mJy beam^{-1}; restoring beam $0''.16 \times 0''.15$ in P.A. $-10°$; polarization vector scale 10 mJy beam^{-1} arcsec^{-1}.

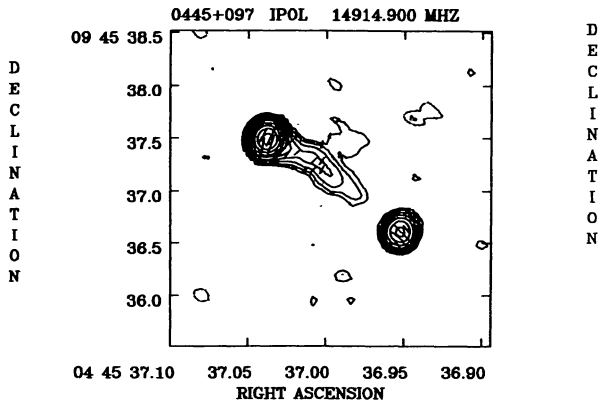

FIG. 43.—0549−213 at 5 GHz; contours $0.45 \times (-1, 1, 2, 4, 8, \cdots)$ mJy beam^{-1}; restoring beam $0''.56 \times 0''.33$ in P.A. 15°; polarization vector scale 10 mJy beam^{-1} arcsec^{-1}.

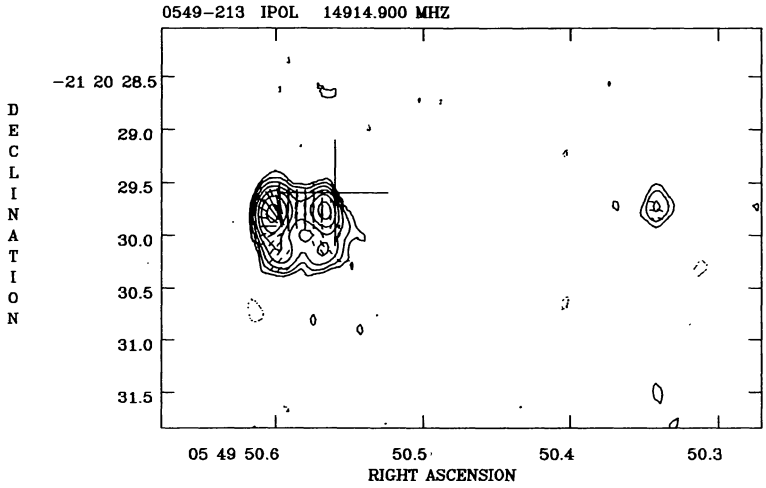

FIG. 44.—0549−213 at 15 GHz; contours $0.3 \times (-1, 1, 2, 4, 8, \cdots)$ mJy beam^{-1}; restoring beam $0''.24 \times 0''.14$ in P.A. 6°; polarization vector scale 10 mJy beam^{-1} arcsec^{-1}.

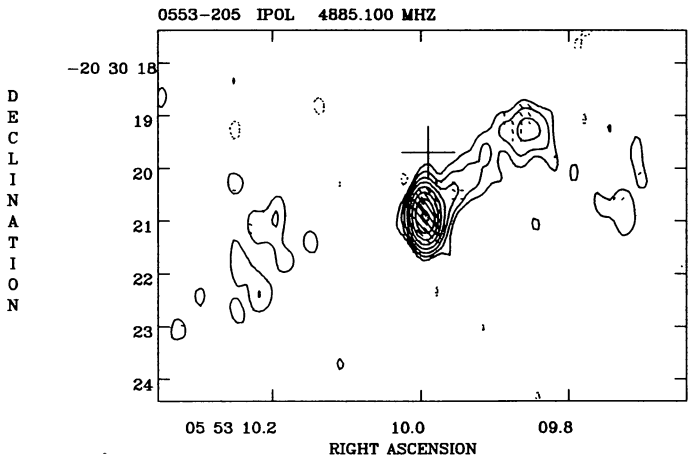

FIG. 45.—0553−205 at 5 GHz; contours $0.3 \times (-1, 1, 2, 4, 8, \cdots)$ mJy beam^{-1}; restoring beam $0''.60 \times 0''.31$ in P.A. 5°; polarization vector scale 5 mJy beam^{-1} arcsec^{-1}.

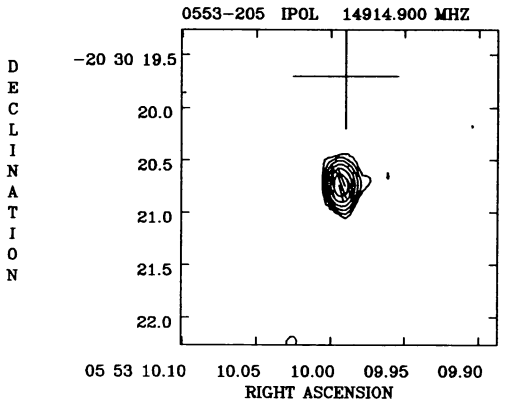

FIG. 46.—0553−205 at 15 GHz; contours $0.45 \times (-1, 1, 2, 4, 8, \cdots)$ mJy beam^{-1}; restoring beam $0''.23 \times 0''.14$ in P.A. 8°; polarization vector scale 5 mJy beam^{-1} arcsec^{-1}.

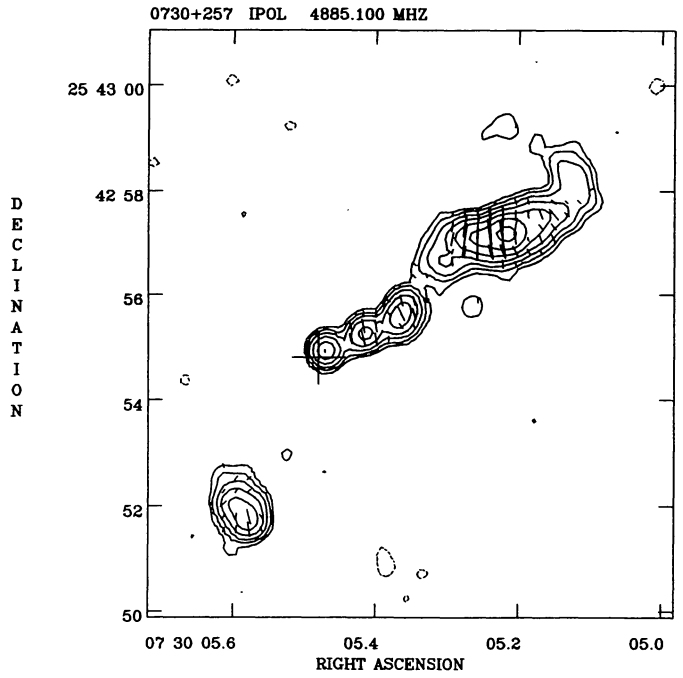

FIG. 47.—0730+257 at 5 GHz; contours $0.3 \times (-1, 1, 2, 4, 8, \cdots)$ mJy beam^{-1}; restoring beam $0''.39 \times 0''.36$ in P.A. 20°; polarization vector scale 5 mJy beam^{-1} arcsec^{-1}.

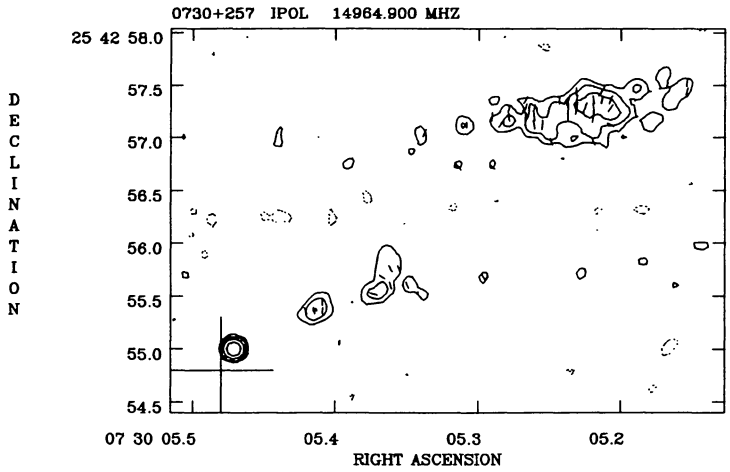

FIG. 48.—0730+257 at 15 GHz; contours $0.3 \times (-1, 1, 2, 4, 8, \cdots)$ mJy beam^{-1}; restoring beam $0''.14$; polarization vector scale 5 mJy beam^{-1} arcsec^{-1}

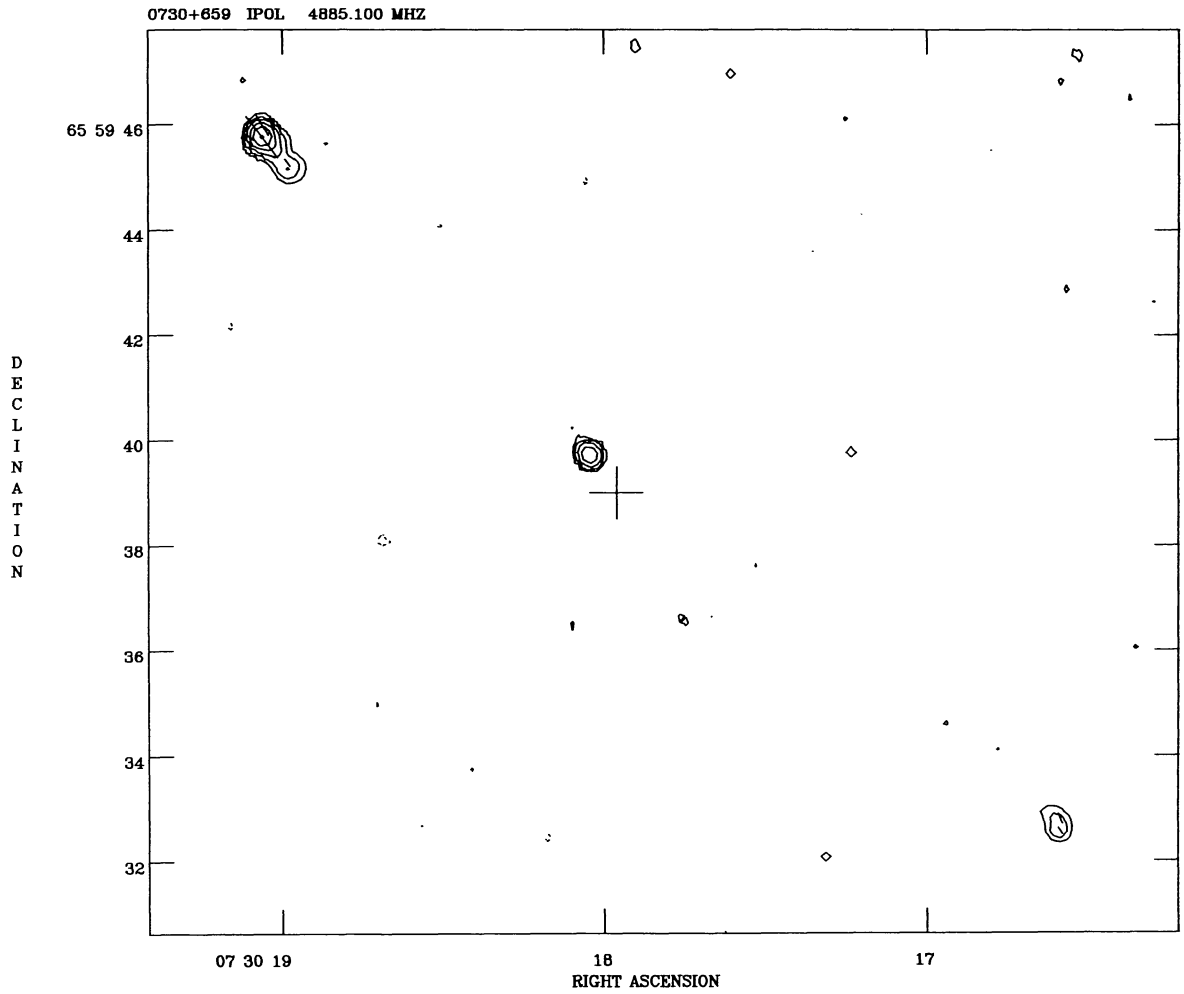

FIG. 49.—0730+659 at 5 GHz; contours $0.3 \times (-1, 1, 2, 4, 8, \cdots)$ mJy beam^{-1}; restoring beam 0.″30; polarization vector scale 2 mJy beam^{-1} arcsec^{-1}

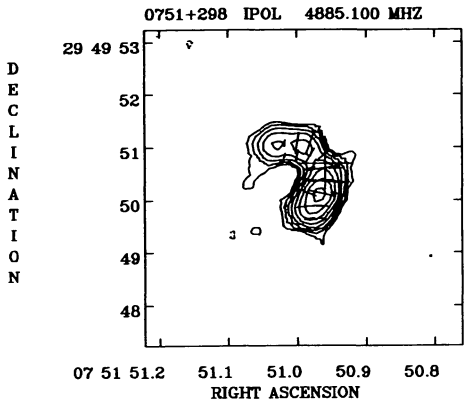

FIG. 50.—0751+298 at 5 GHz; contours $0.45 \times (-1, 1, 2, 4, 8, \cdots)$ mJy beam^{-1}; restoring beam $0''.37 \times 0''.36$ in P.A. 30°; polarization vector scale 5 mJy beam^{-1} arcsec^{-1}

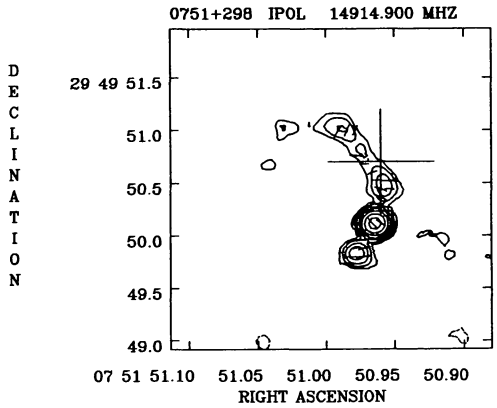

FIG. 51.—0751+298 at 15 GHz; contours $0.45 \times (-1, 1, 2, 4, 8, \cdots)$ mJy beam^{-1}; restoring beam $0''.15 \times 0''.14$ in P.A. 72°; polarization vector scale 5 mJy beam^{-1} arcsec^{-1}.

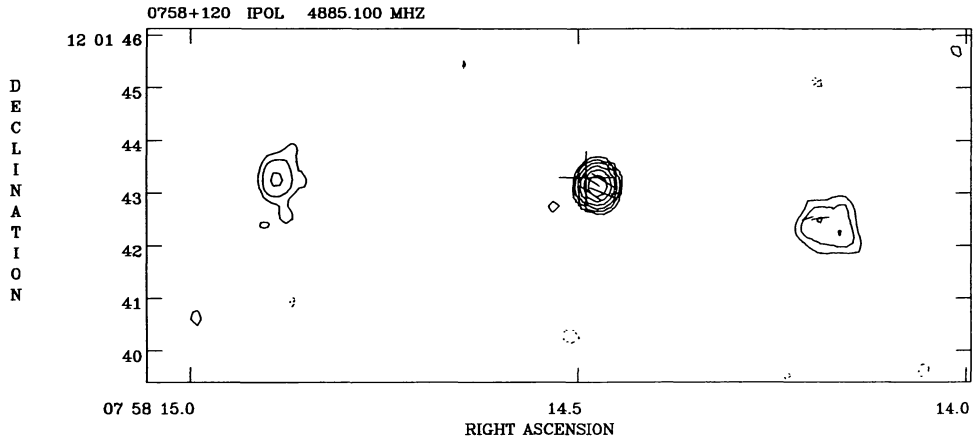

FIG. 52.—0758+120 at 5 GHz; contours $0.45 \times (-1, 1, 2, 4, 8, \cdots)$ mJy beam^{-1}; restoring beam $0''.41 \times 0''.36$ in P.A. 8°; polarization vector scale 2 mJy beam^{-1} arcsec^{-1}.

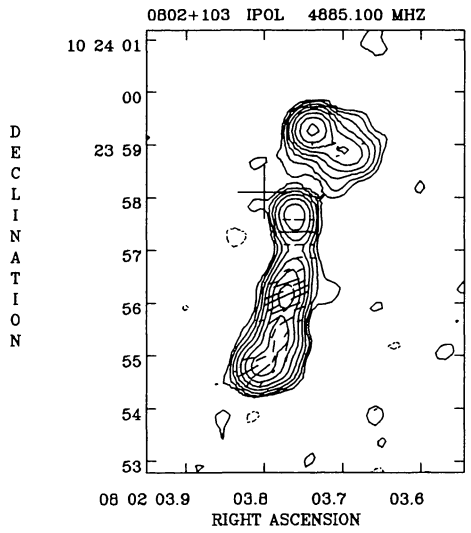

FIG. 53.—0802+103 at 5 GHz; contours $0.6 \times (-1, 1, 2, 4, 8, \cdots)$ mJy beam^{-1}; restoring beam 0.″40; polarization vector scale 10 mJy beam^{-1} arcsec^{-1}.

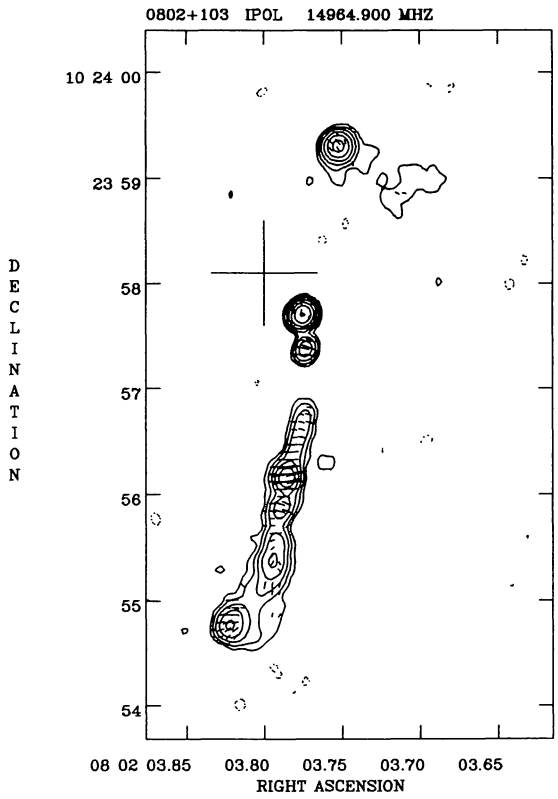

FIG. 54.—0802+103 at 15 GHz; contours $0.45 \times (-1, 1, 2, 4, 8, \cdots)$ mJy beam^{-1}; restoring beam 0.″16 × 0.″14 in P.A. −15°; polarization vector scale 10 mJy beam^{-1} arcsec^{-1}.

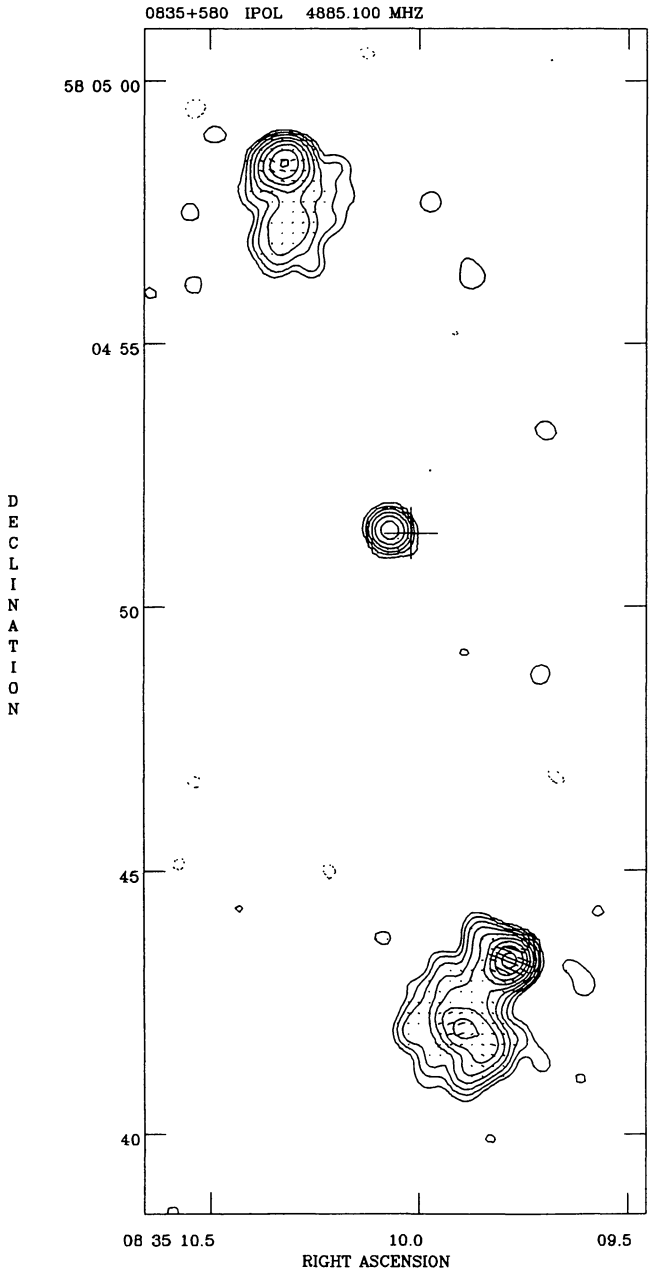

FIG. 55.—0835+580 at 5 GHz; contours 0.45 × (−1, 1, 2, 4, 8, · · ·) mJy beam^{-1}; restoring beam 0″.40; polarization vector scale 50 mJy beam^{-1} arcsec^{-1}.

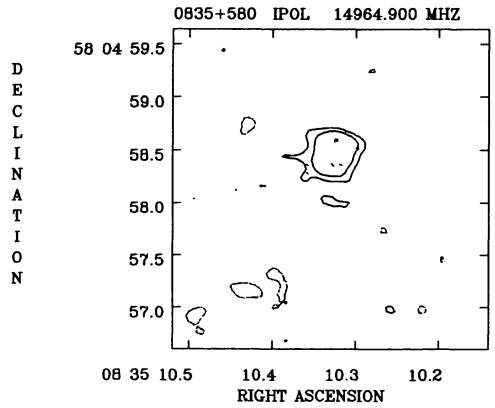

FIG. 56.—0835+580 at 15 GHz; contours 1.0 × (−1, 1, 2, 4, 8, · · ·) mJy beam^{-1}; restoring beam 0″.20 × 0″.14 in P.A. 85°; polarization vector scale 50 mJy beam^{-1} arcsec^{-1}.

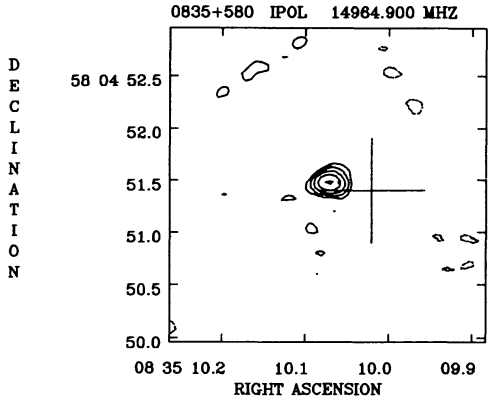

FIG. 57.—Same as Fig. 55

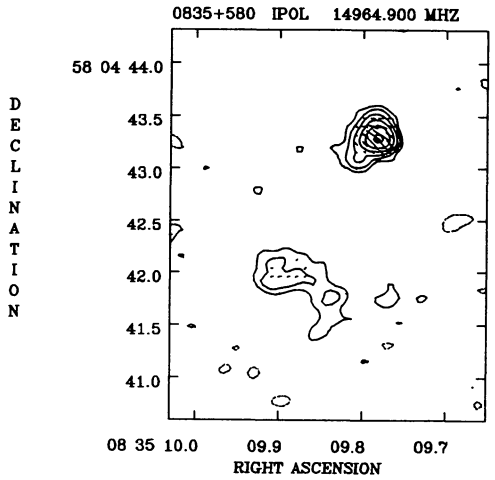

FIG. 58.—Same as Fig. 55

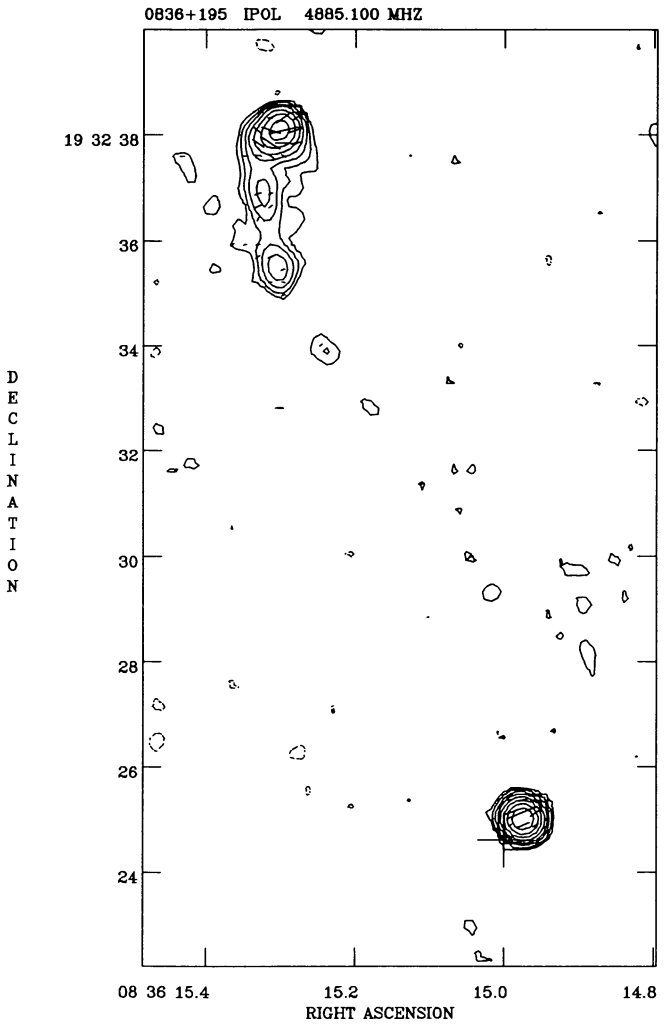

FIG. 59.—0836+195 at 5 GHz; contours $0.3 \times (-1, 1, 2, 4, 8, \cdots)$ mJy beam^{-1}; restoring beam $0''.41 \times 0''.38$ in P.A. 61°; polarization vector scale 5 mJy beam^{-1} arcsec^{-1}.

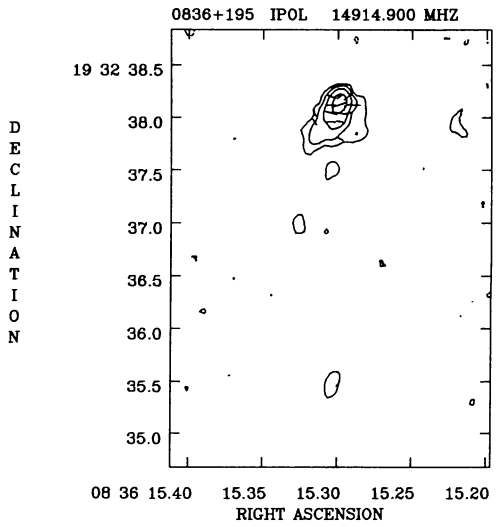

FIG. 60.—0836+195 at 15 GHz; contours $0.3 \times (-1, 1, 2, 4, 8, \cdots)$ mJy beam^{-1}; restoring beam $0''.15 \times 0''.13$ in P.A. 7°; polarization vector scale 5 mJy beam^{-1} arcsec^{-1}.

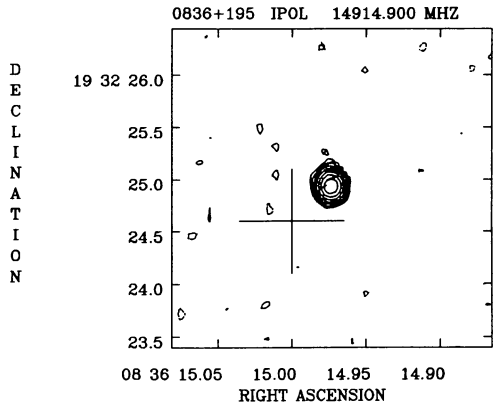

FIG. 61.—Same as Fig. 59

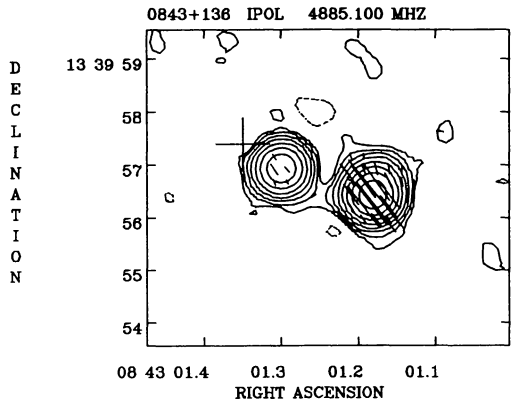

FIG. 62.—0843+136 at 5 GHz; contours $0.45 \times (-1, 1, 2, 4, 8, \cdots)$ mJy beam^{-1}; restoring beam 0″.55; polarization vector scale 5 mJy beam^{-1} arcsec^{-1}.

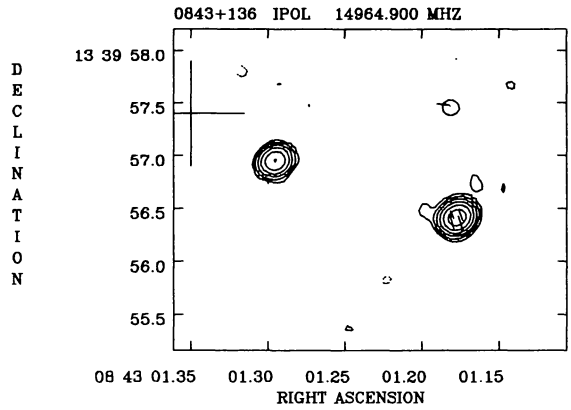

FIG. 63.—0843+136 at 15 GHz; contours $0.6 \times (-1, 1, 2, 4, 8, \cdots)$ mJy beam^{-1}; restoring beam 0″.19 × 0″.16 in P.A. −65°; polarization vector scale 10 mJy beam^{-1} arcsec^{-1}.

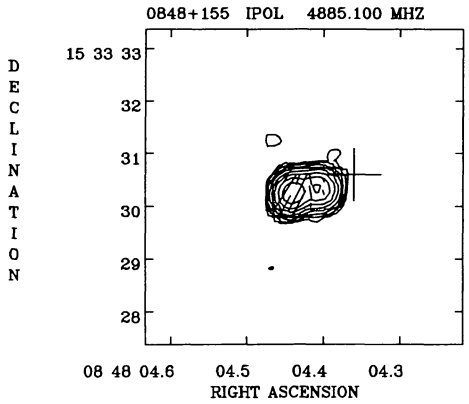

FIG. 64.—0848+155 at 5 GHz; contours $0.45 \times (-1, 1, 2, 4, 8, \cdots)$ mJy beam^{-1}; restoring beam 0″.39 × 0″.36 in P.A. −2°; polarization vector scale 2 mJy beam^{-1} arcsec^{-1}.

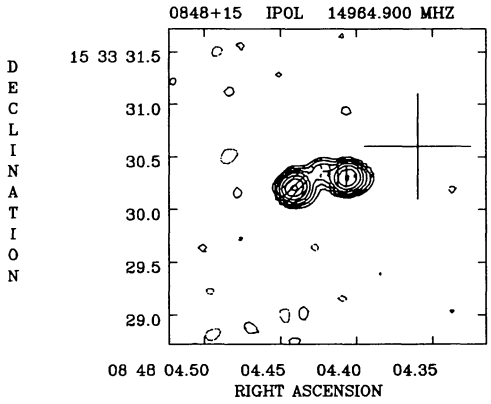

FIG. 65.—0848+155 at 15 GHz; contours $0.45 \times (-1, 1, 2, 4, 8, \cdots)$ mJy beam^{-1}; restoring beam 0″.15 × 0″.14 in P.A. −54°; polarization vector scale 20 mJy beam^{-1} arcsec^{-1}.

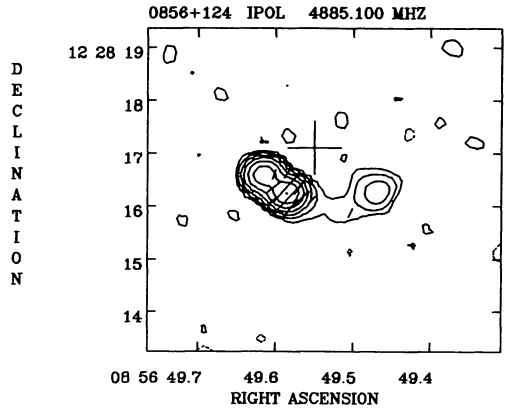

FIG. 66.—0856+124 at 5 GHz; contours $0.3 \times (-1, 1, 2, 4, 8, \cdots)$ mJy beam^{-1}; restoring beam $0''.43 \times 0''.37$ in P.A. 88°; polarization vector scale 2 mJy beam^{-1} arcsec^{-1}.

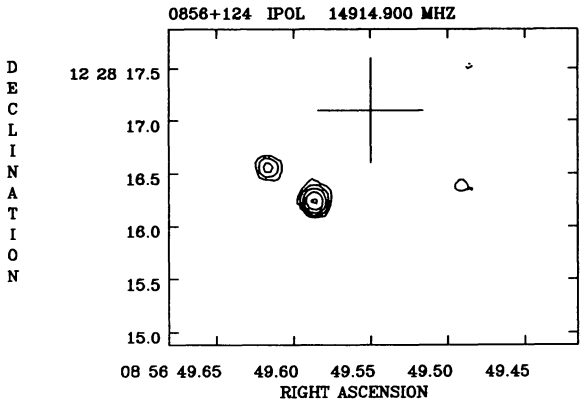

FIG. 67.—0856+124 at 15 GHz; contours $0.6 \times (-1, 1, 2, 4, 8, \cdots)$ mJy beam^{-1}; restoring beam $0''.15 \times 0''.13$ in P.A. 1°.

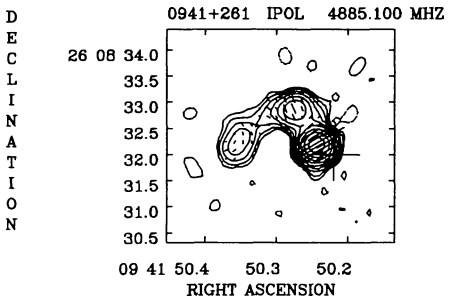

FIG. 68.—0941+261 at 5 GHz; contours $0.6 \times (-1, 1, 2, 4, 8, \cdots)$ mJy beam^{-1}; restoring beam $0''.35$; polarization vector scale 20 mJy beam^{-1} arcsec^{-1}.

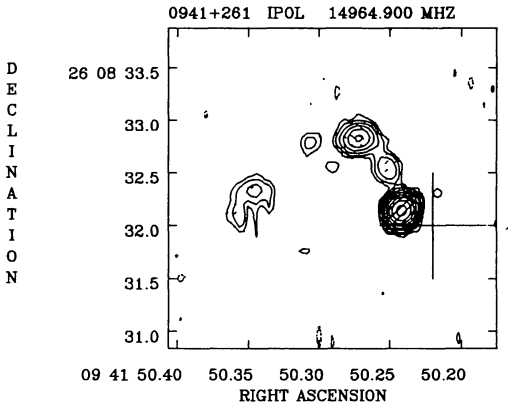

FIG. 69.—0941+261 at 15 GHz; contours $0.3 \times (-1, 1, 2, 4, 8, \cdots)$ mJy beam^{-1}; restoring beam $0''.15 \times 0''.14$ in P.A. −28°; polarization vector scale 20 mJy beam^{-1} arcsec^{-1}.

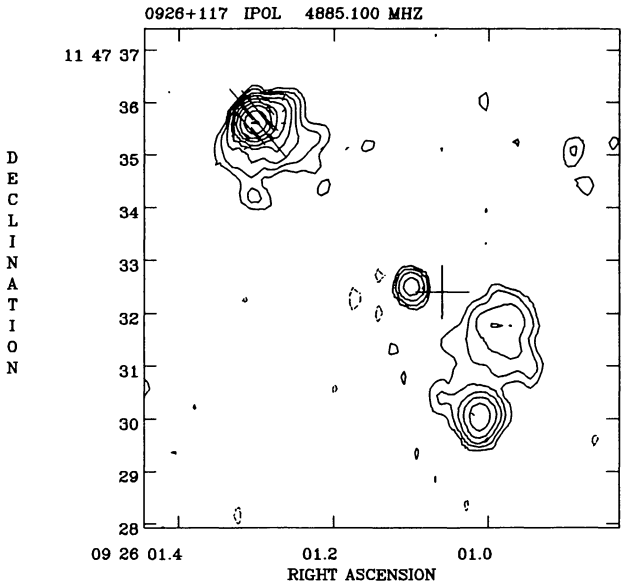

FIG. 70.—0926+117 at 5 GHz; contours $0.3 \times (-1, 1, 2, 4, 8, \cdots)$ mJy beam^{-1}; restoring beam 0.″39 × 0.″36 in P.A. −5°; polarization vector scale 5 mJy beam^{-1} arcsec^{-1}.

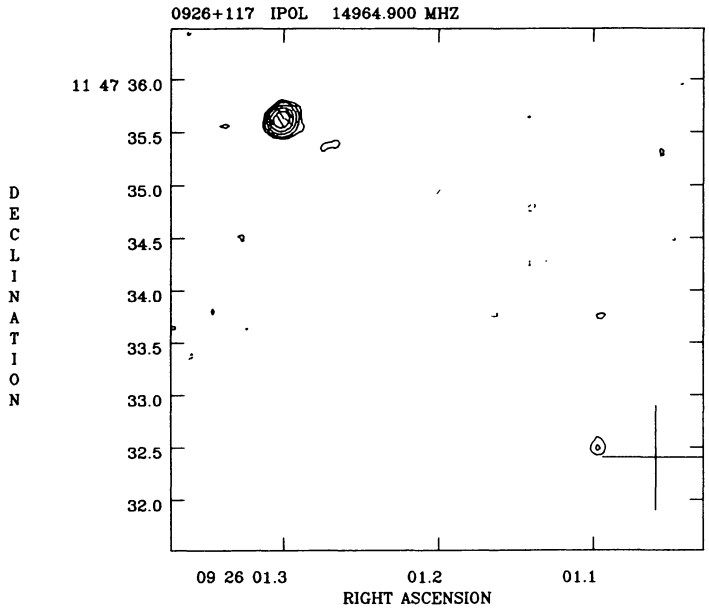

FIG. 71.—0926+117 at 15 GHz; contours $1.0 \times (-1, 1, 2, 4, 8, \cdots)$ mJy beam^{-1}; restoring beam 0.″15; polarization vector scale 20 mJy beam^{-1} arcsec^{-1}

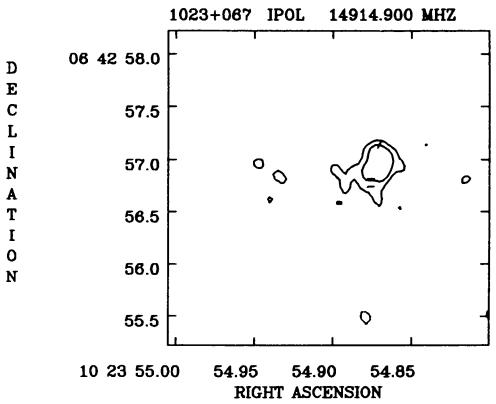

FIG. 73.—1023+067 at 15 GHz; contours $0.3 \times (-1, 1, 2, 4, 8, \cdots)$ mJy beam^{-1}; restoring beam $0''.16 \times 0''.14$ in P.A. 14°; polarization vector scale 5 mJy beam^{-1} arcsec^{-1}.

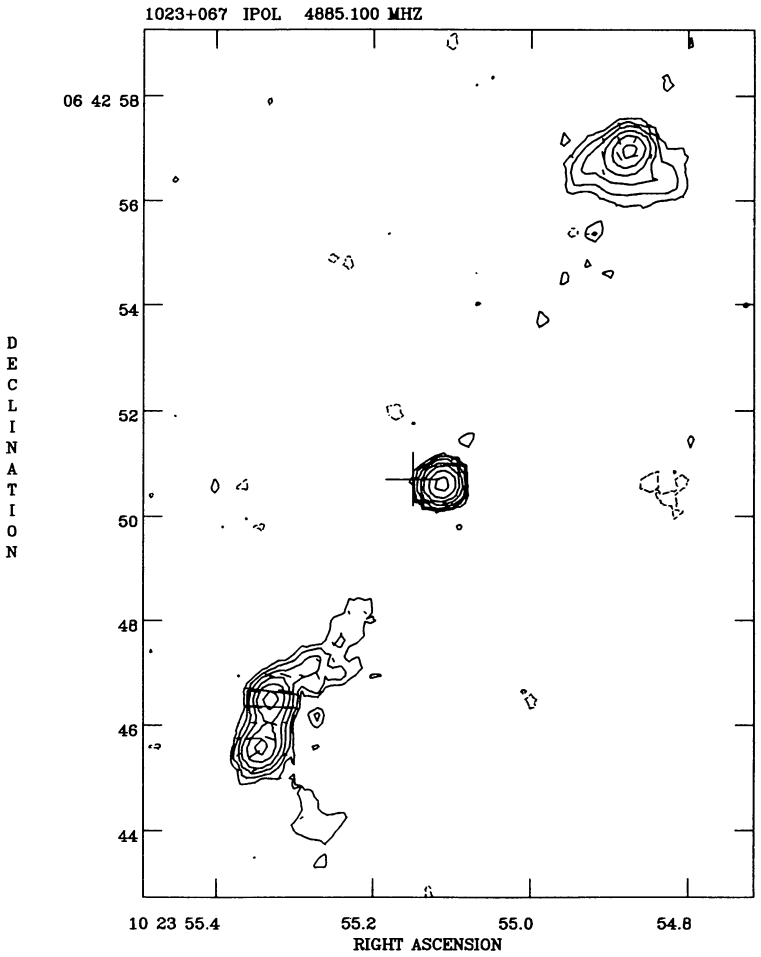

FIG. 72.—1023+067 at 5 GHz; contours $0.6 \times (-1, 1, 2, 4, 8, \cdots)$ mJy beam^{-1}; restoring beam $0''.40$; polarization vector scale 5 mJy beam^{-1} arcsec^{-1}.

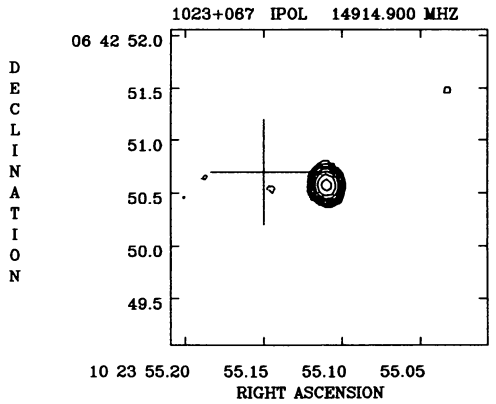

FIG. 74.—Same as Fig. 73

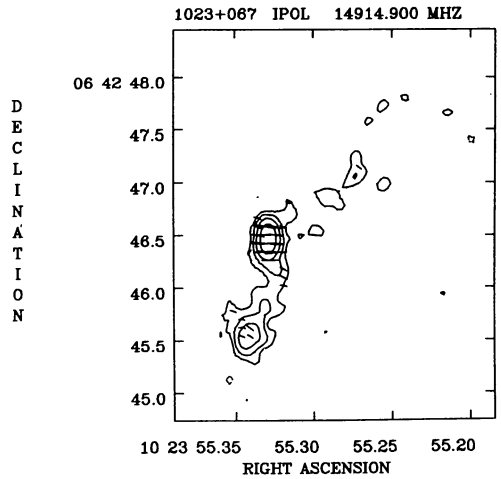

FIG. 75.—Same as Fig. 73

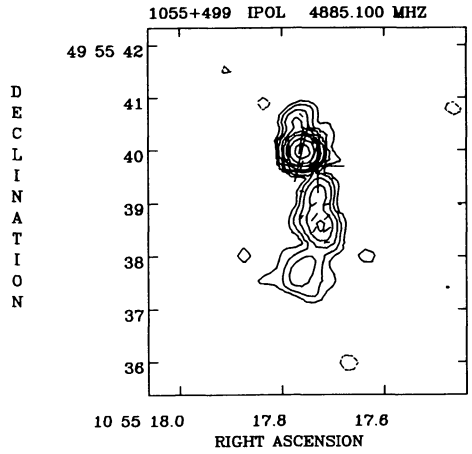

FIG. 76.—1055+499 at 5 GHz; contours $0.3 \times (-1, 1, 2, 4, 8, \cdots)$ mJy beam^{-1}; restoring beam $0''.34 \times 0''.33$ in P.A. 40°; polarization vector scale 5 mJy beam^{-1} arcsec^{-1}.

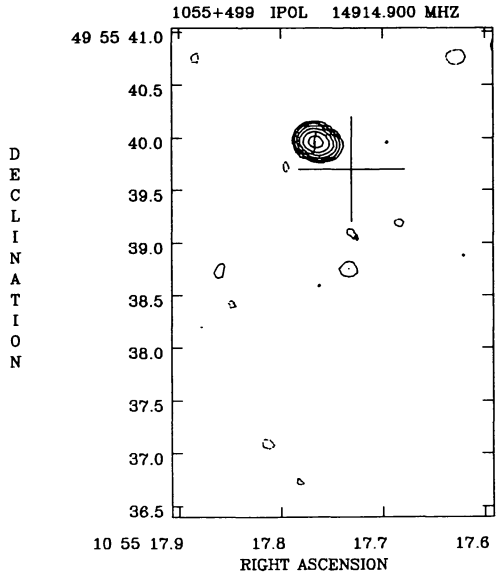

FIG. 77.—1055+499 at 15 GHz; contours $0.6 \times (-1, 1, 2, 4, 8, \cdots)$ mJy beam^{-1}; restoring beam $0''.18 \times 0''.15$ in P.A. 64°; polarization vector scale 10 mJy beam^{-1} arcsec^{-1}.

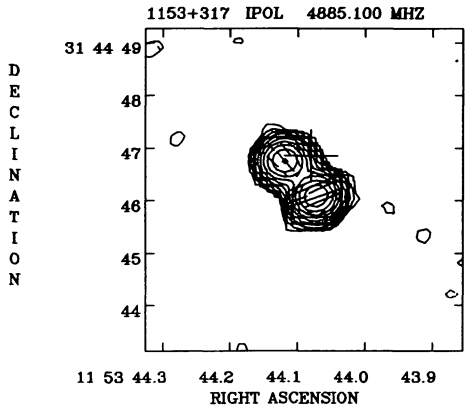

FIG. 78.—1153+317 at 5 GHz; contours $0.6 \times (-1, 1, 2, 4, 8, \cdots)$ mJy beam^{-1}; restoring beam $0''.43 \times 0''.39$ in P.A. −87°; polarization vector scale 5 mJy beam^{-1} arcsec^{-1}.

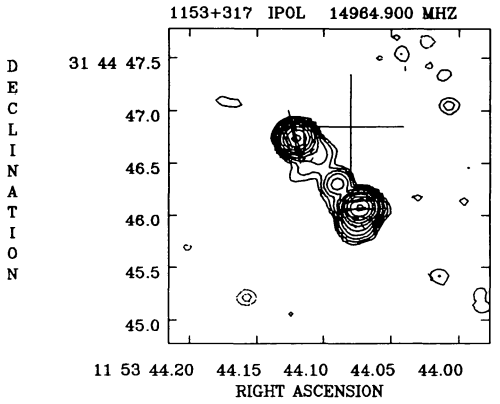

FIG. 79.—1153+317 at 15 GHz; contours $0.2 \times (-1, 1, 2, 4, 8, \cdots)$ mJy beam^{-1}; restoring beam $0''.16 \times 0''.14$ in P.A. −85°; polarization vector scale 10 mJy beam^{-1} arcsec^{-1}.

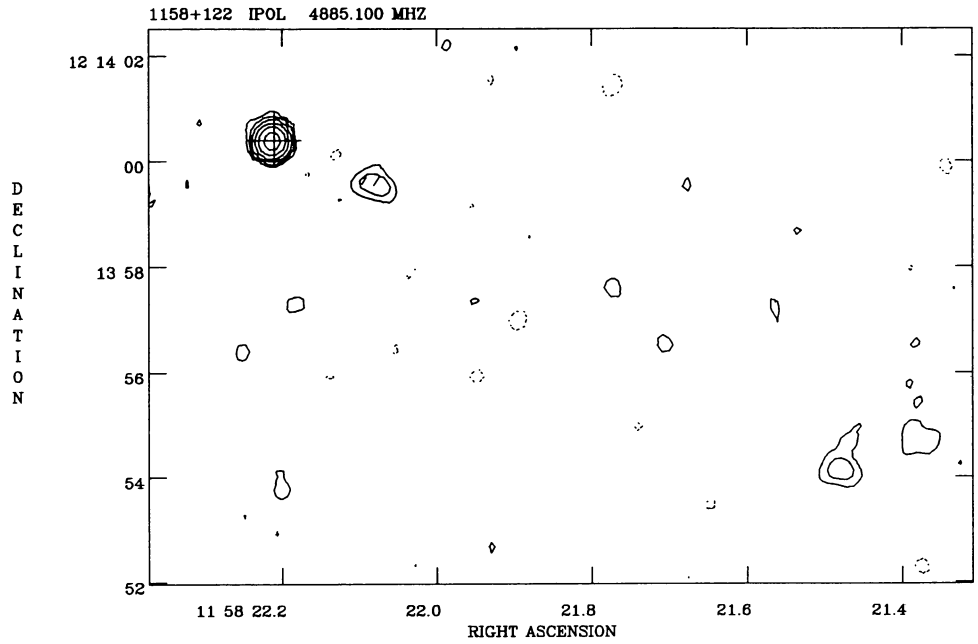

FIG. 80.—1158+122 at 5 GHz; contours $0.3 \times (-1, 1, 2, 4, 8, \cdots)$ mJy beam^{-1}; restoring beam $0''.39 \times 0''.36$ in P.A. 0°; polarization vector scale 2 mJy beam^{-1} arcsec^{-1}.

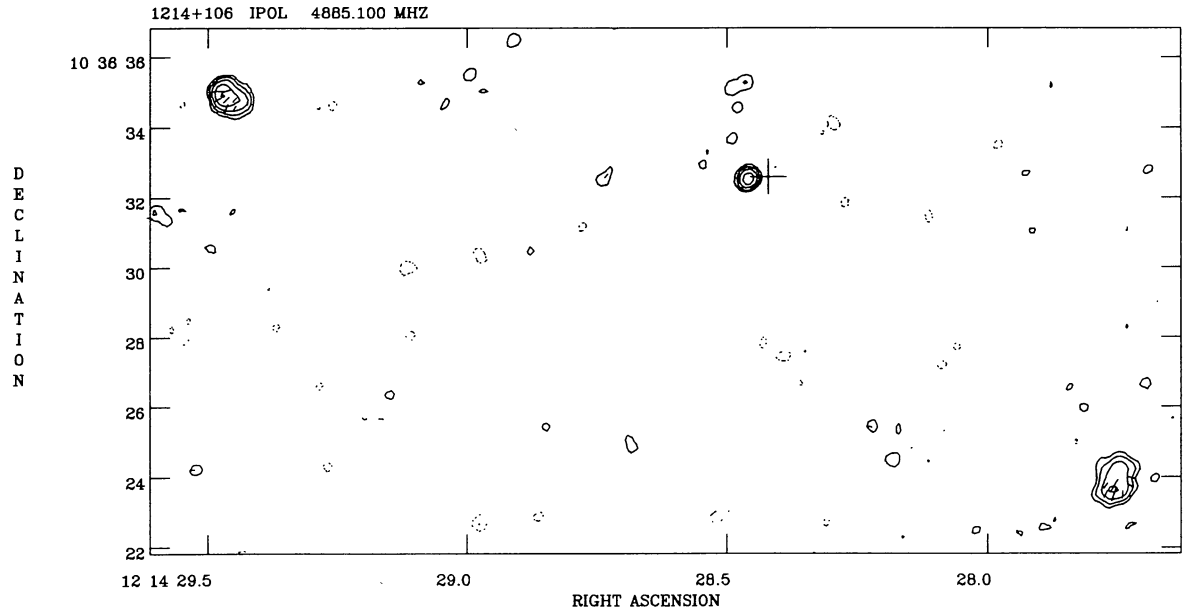

FIG. 81.—1214+106 at 5 GHz; contours $0.3 \times (-1, 1, 2, 4, 8, \cdots)$ mJy beam^{-1}; restoring beam $0''.39 \times 0''.36$ in P.A. −9°; polarization vector scale 2 mJy beam^{-1} arcsec^{-1}.

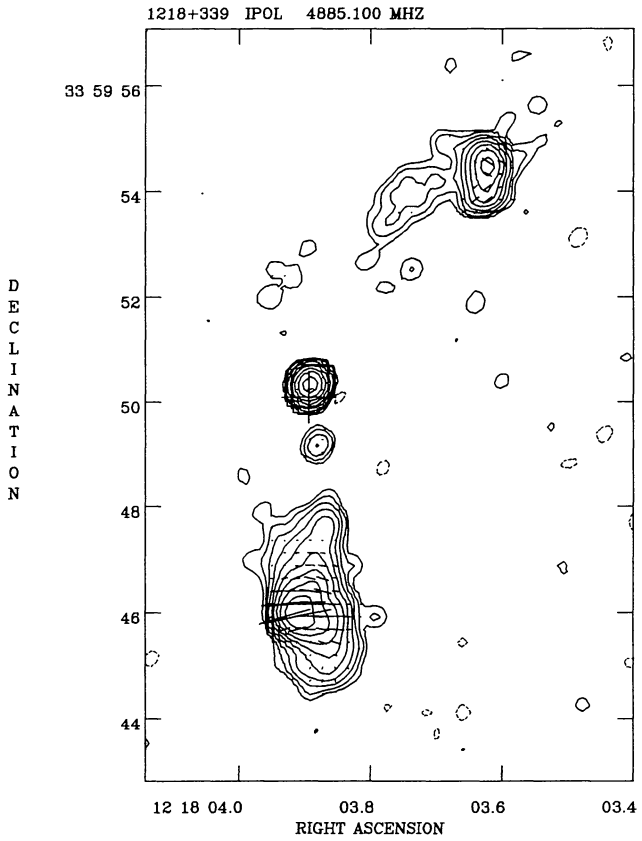

FIG. 82.—1218+339 at 5 GHz; contours $0.3 \times (-1, 1, 2, 4, 8, \cdots)$ mJy beam^{-1}; restoring beam $0''.36 \times 0''.34$ in P.A. $-22°$; polarization vector scale 20 mJy beam^{-1} arcsec^{-1}.

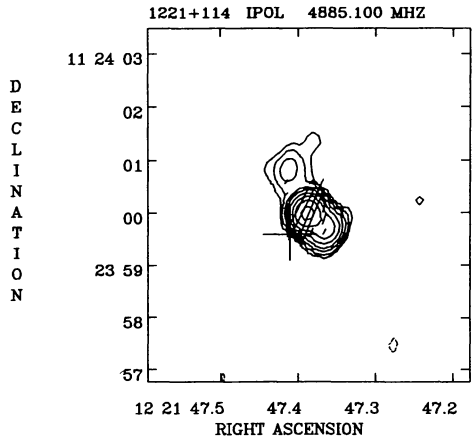

FIG. 83.—1221+114 at 5 GHz; contours $0.45 \times (-1, 1, 2, 4, 8, \cdots)$ mJy beam^{-1}; restoring beam $0''.40 \times 0''.34$ in P.A. $-13°$; polarization vector scale 5 mJy beam^{-1} arcsec^{-1}.

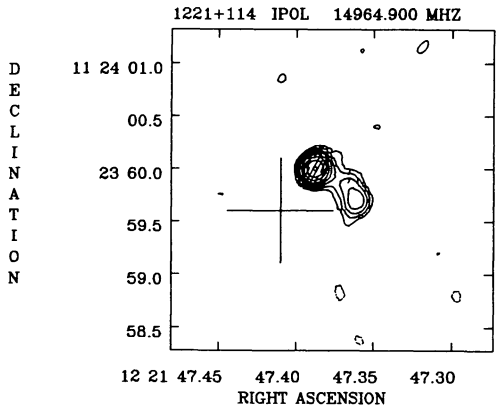

FIG. 84.—1221+114 at 15 GHz; contours $0.3 \times (-1, 1, 2, 4, 8, \cdots)$ mJy beam^{-1}; restoring beam $0''.15 \times 0''.14$ in P.A. $-18°$; polarization vector scale 10 mJy beam^{-1} arcsec^{-1}.

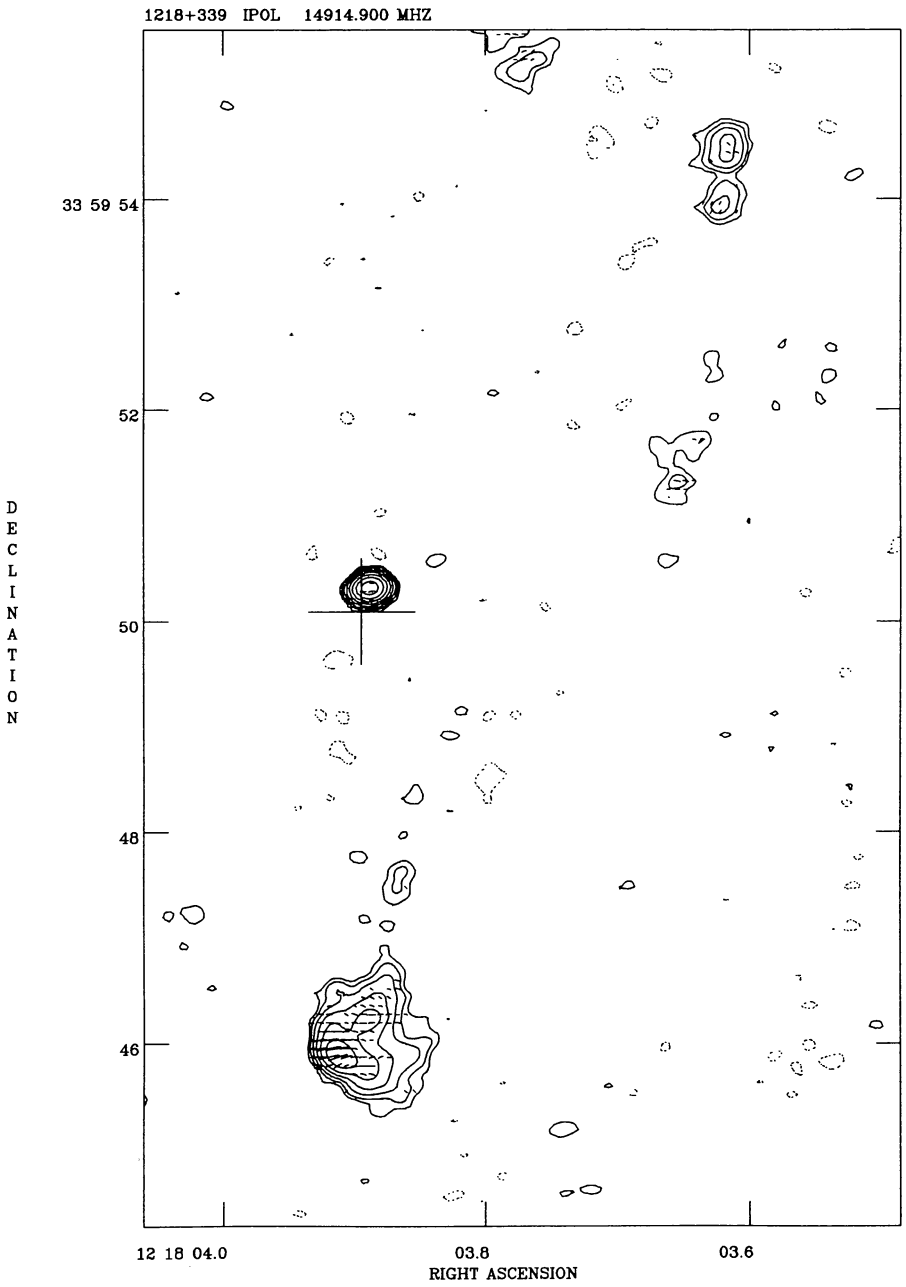

FIG. 85.—1218+339 at 15 GHz; contours $0.45 \times (-1, 1, 2, 4, 8, \cdots)$ mJy beam^{-1}; restoring beam $0''.20 \times 0''.15$ in P.A. $-85°$; polarization vector scale 20 mJy beam^{-1} arcsec^{-1}.

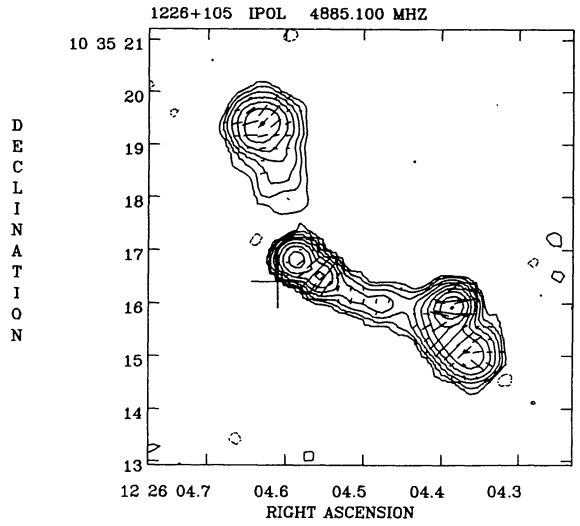

FIG. 86.—1226+105 at 5 GHz; contours $0.2 \times (-1, 1, 2, 4, 8, \cdots)$ mJy beam^{-1}; restoring beam 0″.38; polarization vector scale 5 mJy beam^{-1} arcsec^{-1}

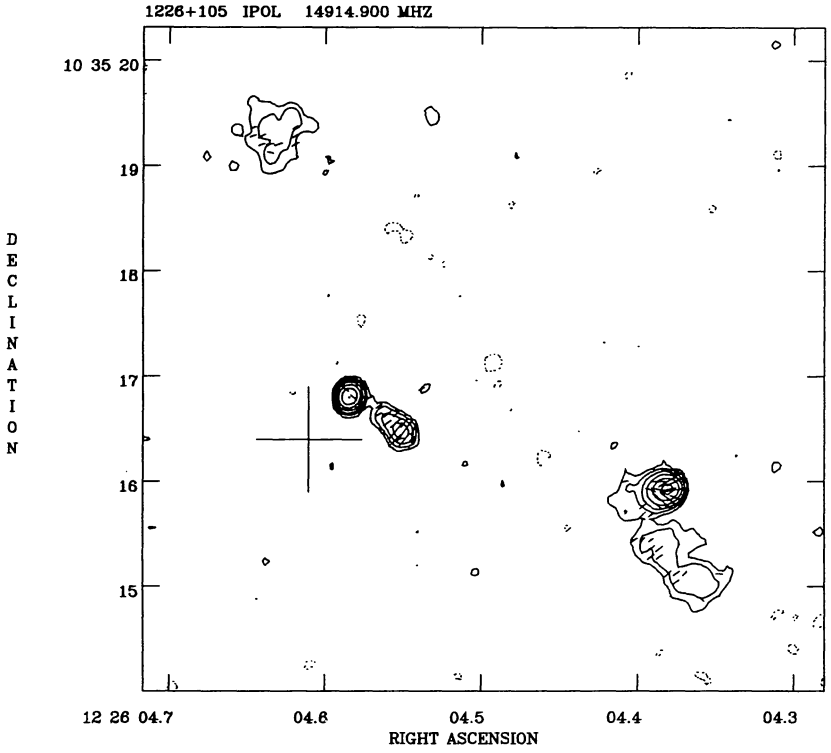

FIG. 87.—1226+105 at 15 GHz; contours $0.3 \times (-1, 1, 2, 4, 8, \cdots)$ mJy beam^{-1}; restoring beam 0″.15 × 0″.14 in P.A. −23°; polarization vector scale 5 mJy beam^{-1} arcsec^{-1}.

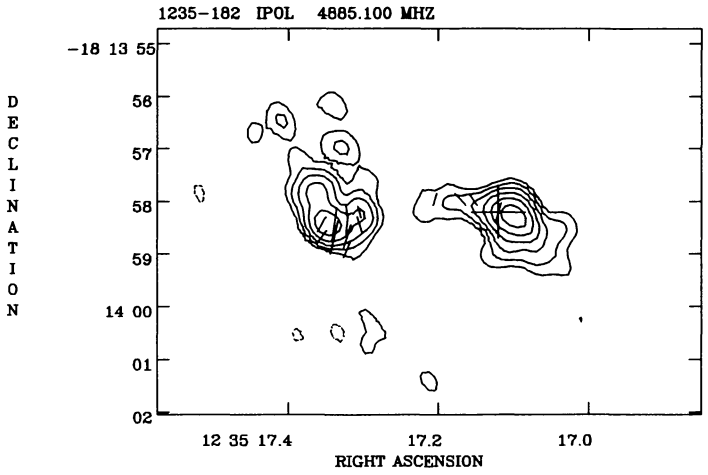

FIG. 88.—1235−182 at 5 GHz; contours 0.45 × (−1, 1, 2, 4, 8, · · ·) mJy beam^{-1}; restoring beam 0.″48 × 0.″36 in P.A. 28°; polarization vector scale 2 mJy beam^{-1} arcsec^{-1}.

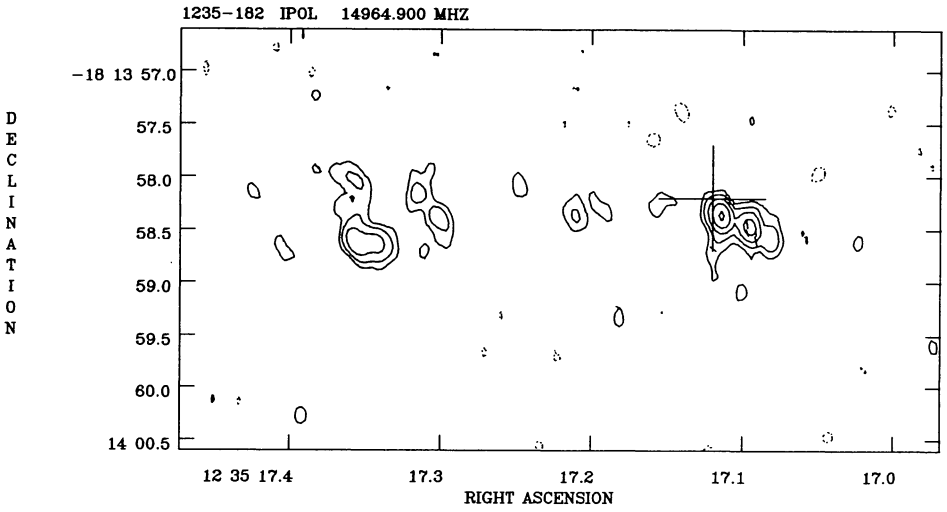

FIG. 89.—1235−182 at 15 GHz; contours 0.°3 × (−1, 1, 2, 4, 8, · · ·) mJy beam^{-1}; restoring beam 0.″22 × 0.″14 in P.A. 13°; polarization vector scale 5 mJy beam^{-1} arcsec^{-1}.

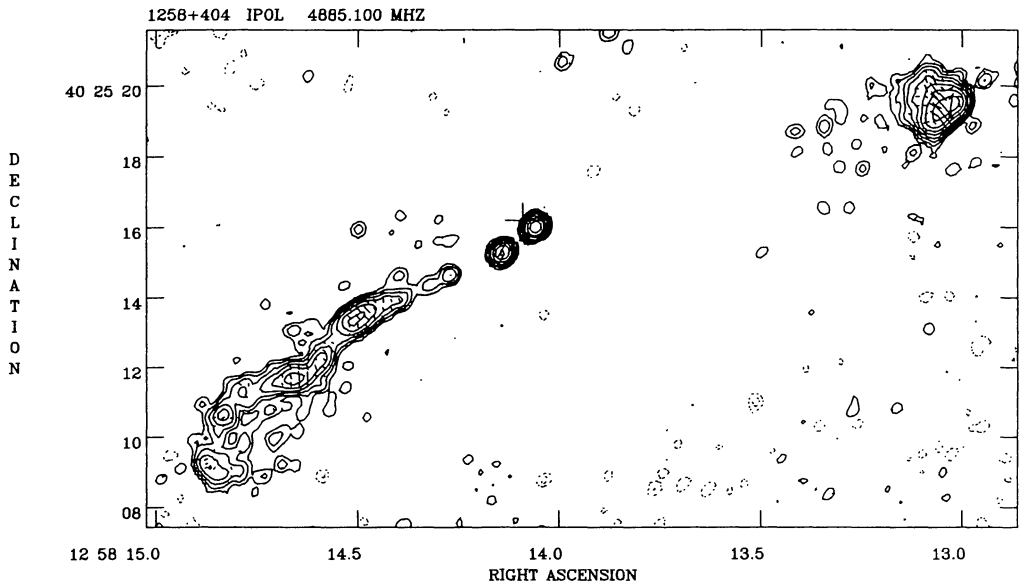

FIG. 90.—1258+404 at 5 GHz; contours $0.15 \times (-1, 1, 2, 4, 8, \cdots)$ mJy beam^{-1}; restoring beam $0''.34 \times 0''.32$ in P.A. $-24°$; polarization vector scale 5 mJy beam^{-1} arcsec^{-1}.

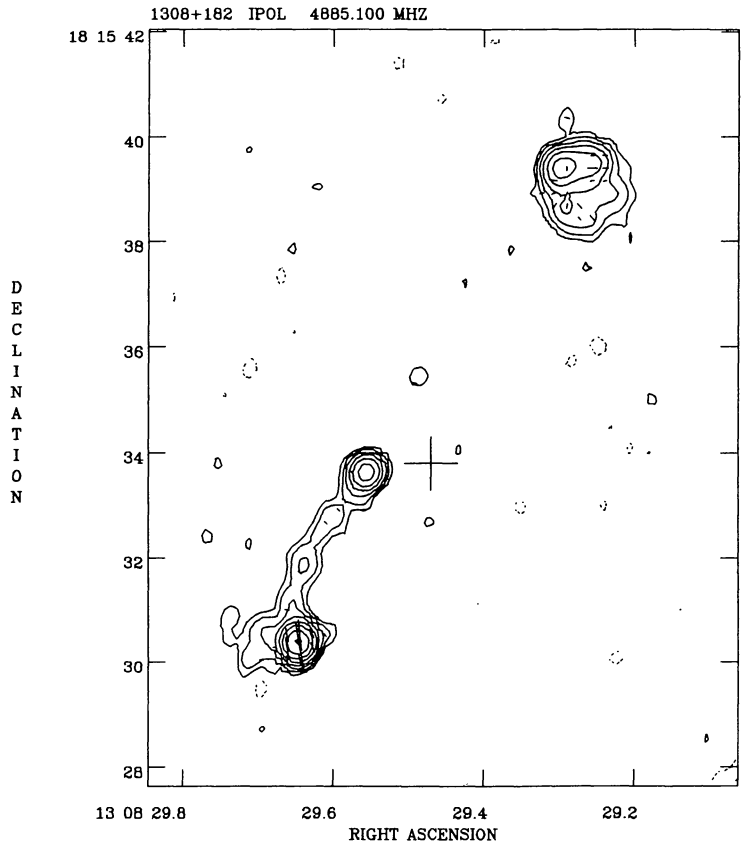

FIG. 91.—1308+182 at 5 GHz; contours $0.3 \times (-1, 1, 2, 4, 8, \cdots)$ mJy beam^{-1}; restoring beam $0''.39 \times 0''.35$ in P.A. $-5°$; polarization vector scale 5 mJy beam^{-1} arcsec^{-1}.

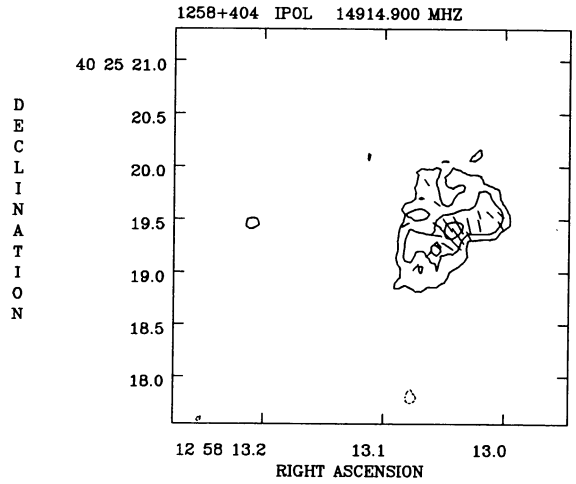

FIG. 92.—1258+404 at 15 GHz; contours $0.45 \times (-1, 1, 2, 4, 8, \cdots)$ mJy beam^{-1}; restoring beam $0''.15 \times 0''.14$ in P.A. 68°; polarization vector scale 5 mJy beam^{-1} arcsec^{-1}.

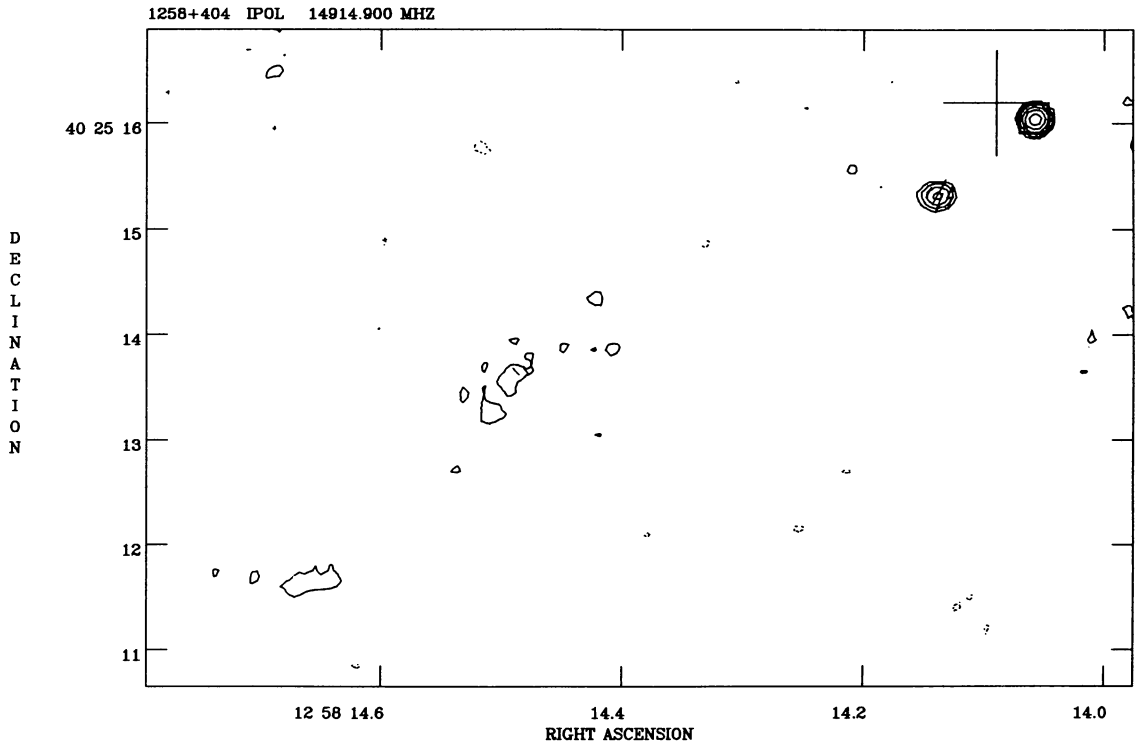

FIG. 93.—Same as Fig. 92

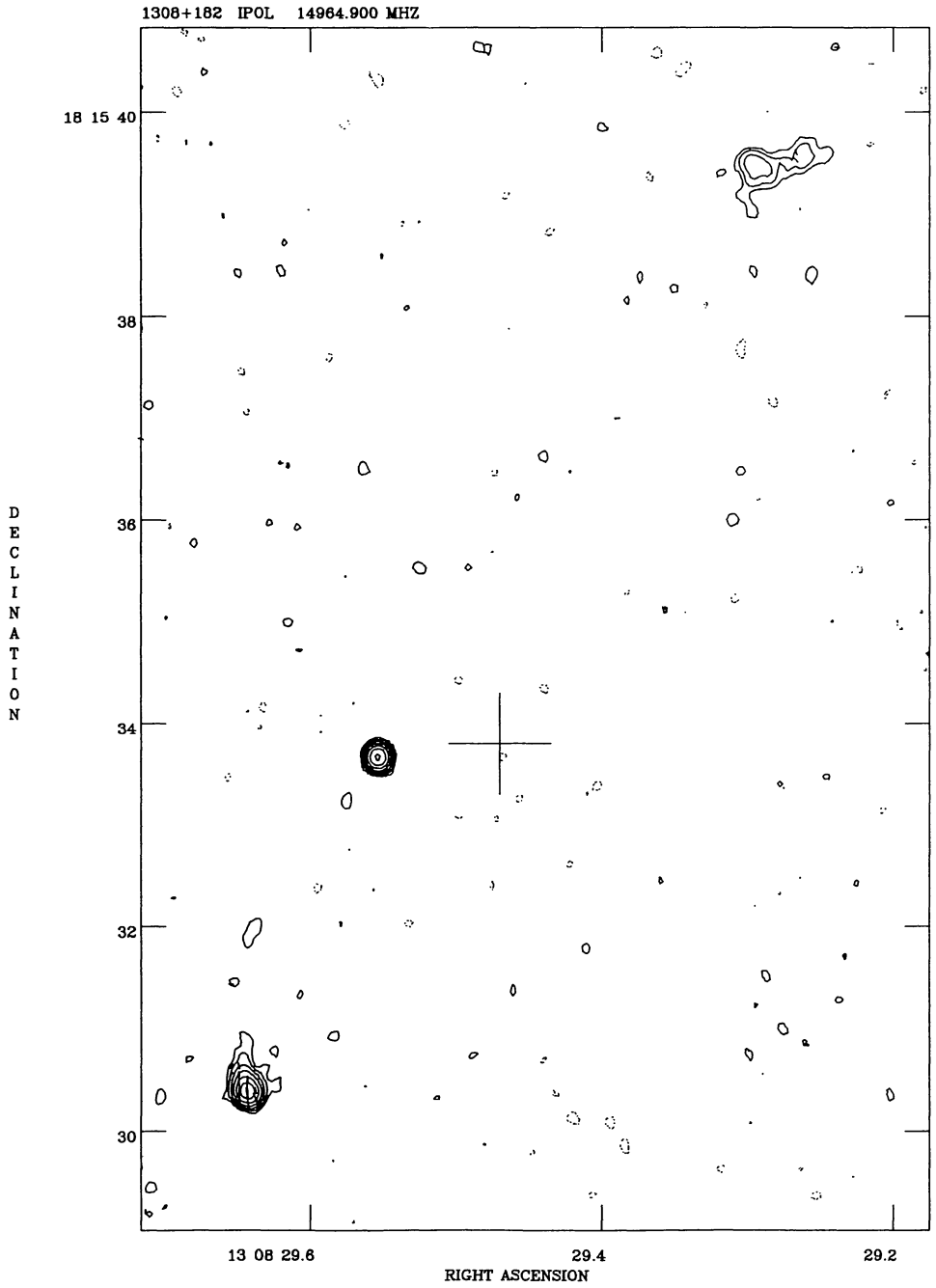

FIG. 94.—1308+182 at 15 GHz; contours $0.2 \times (-1, 1, 2, 4, 8, \cdots)$ mJy beam^{-1}; restoring beam 0.″14; polarization vector scale 5 mJy beam^{-1} arcsec^{-1}

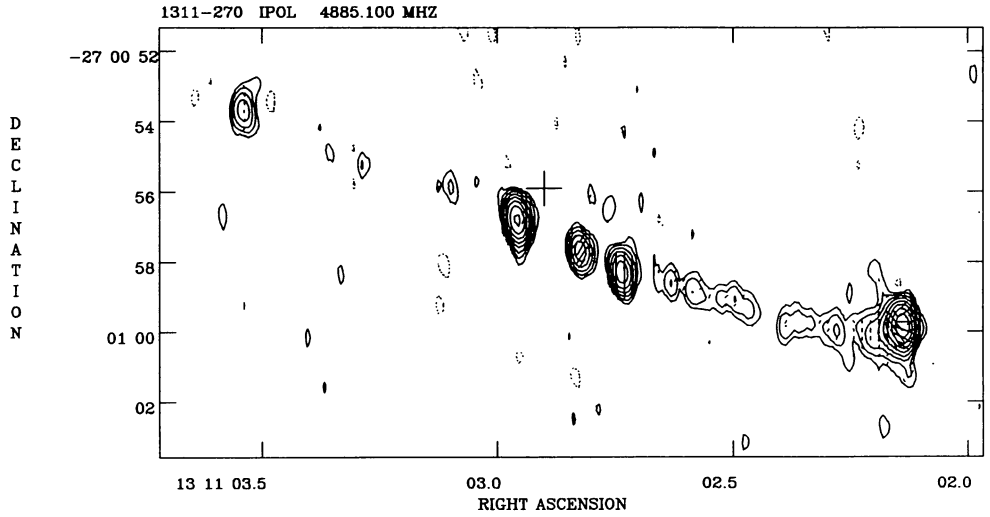

FIG. 95.—1311−270 at 5 GHz; contours $0.3 \times (-1, 1, 2, 4, 8, \cdots)$ mJy beam^{-1}; restoring beam $0''.69 \times 0''.32$ in P.A. 7°; polarization vector scale 5 mJy beam^{-1} arcsec^{-1}.

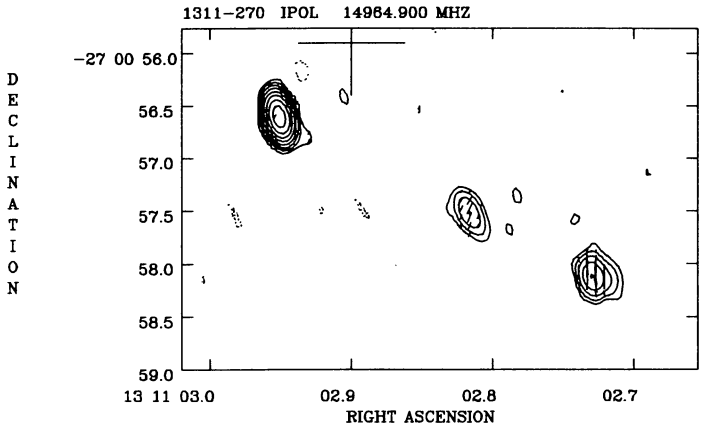

FIG. 96.—1311−270 at 15 GHz; contours $0.3 \times (-1, 1, 2, 4, 8, \cdots)$ mJy beam^{-1}; restoring beam $0''.25 \times 0''.13$ in P.A. 15°; polarization vector scale 10 mJy beam^{-1} arcsec^{-1}.

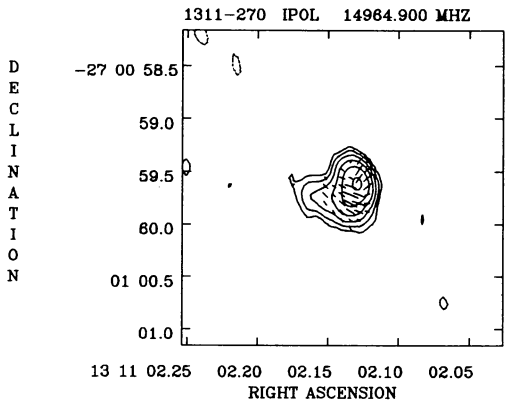

FIG. 97.—Same as Fig. 96

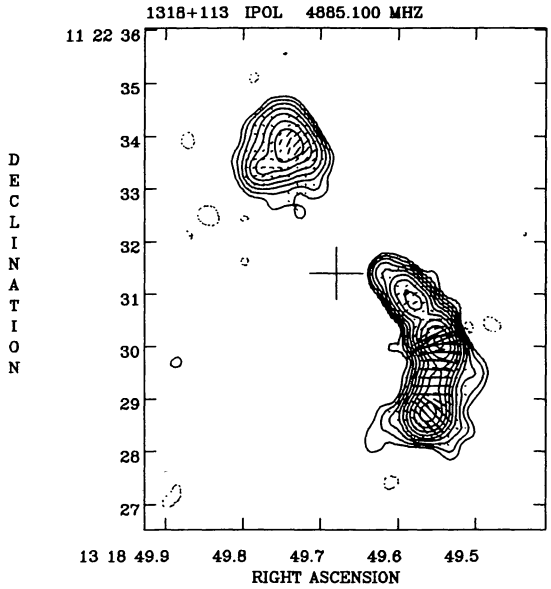

FIG. 98.—1318+113 at 5 GHz; contours $0.3 \times (-1, 1, 2, 4, 8, \cdots)$ mJy beam^{-1}; restoring beam $0''.38 \times 0''.34$ in P.A. $-4°$; polarization vector scale 2 mJy beam^{-1} arcsec^{-1}.

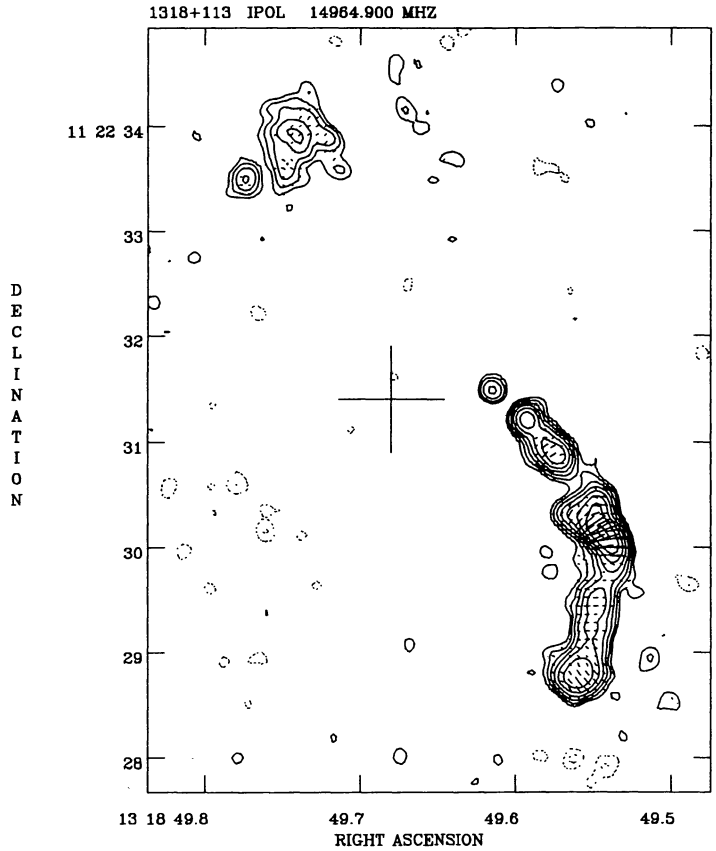

FIG. 99.—1318+113 at 15 GHz; contours $0.2 \times (-1, 1, 2, 4, 8, \cdots)$ mJy beam^{-1}; restoring beam $0''.16 \times 0''.14$ in P.A. 31°; polarization vector scale 20 mJy beam^{-1} arcsec^{-1}.

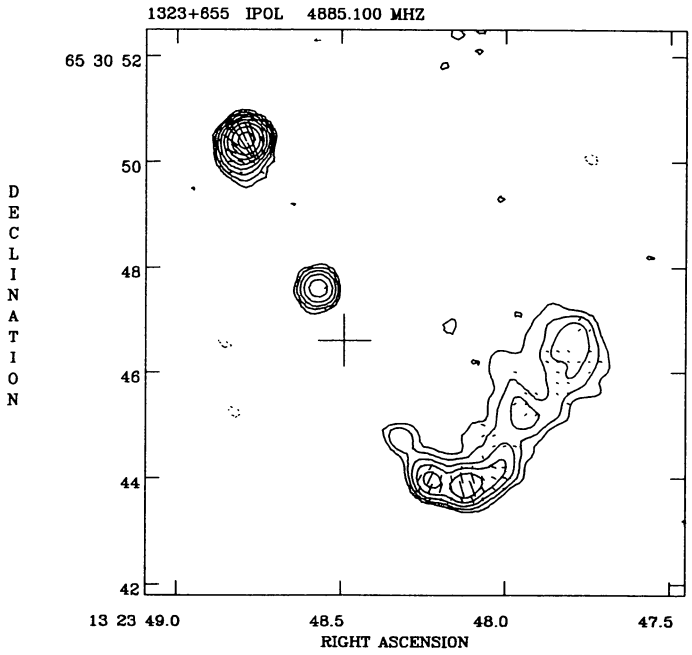

FIG. 100.—1323+655 at 5 GHz; contours $0.45 \times (-1, 1, 2, 4, 8, \cdots)$ mJy beam^{-1}; restoring beam 0.″40; polarization vector scale 10 mJy beam^{-1} arcsec^{-1}.

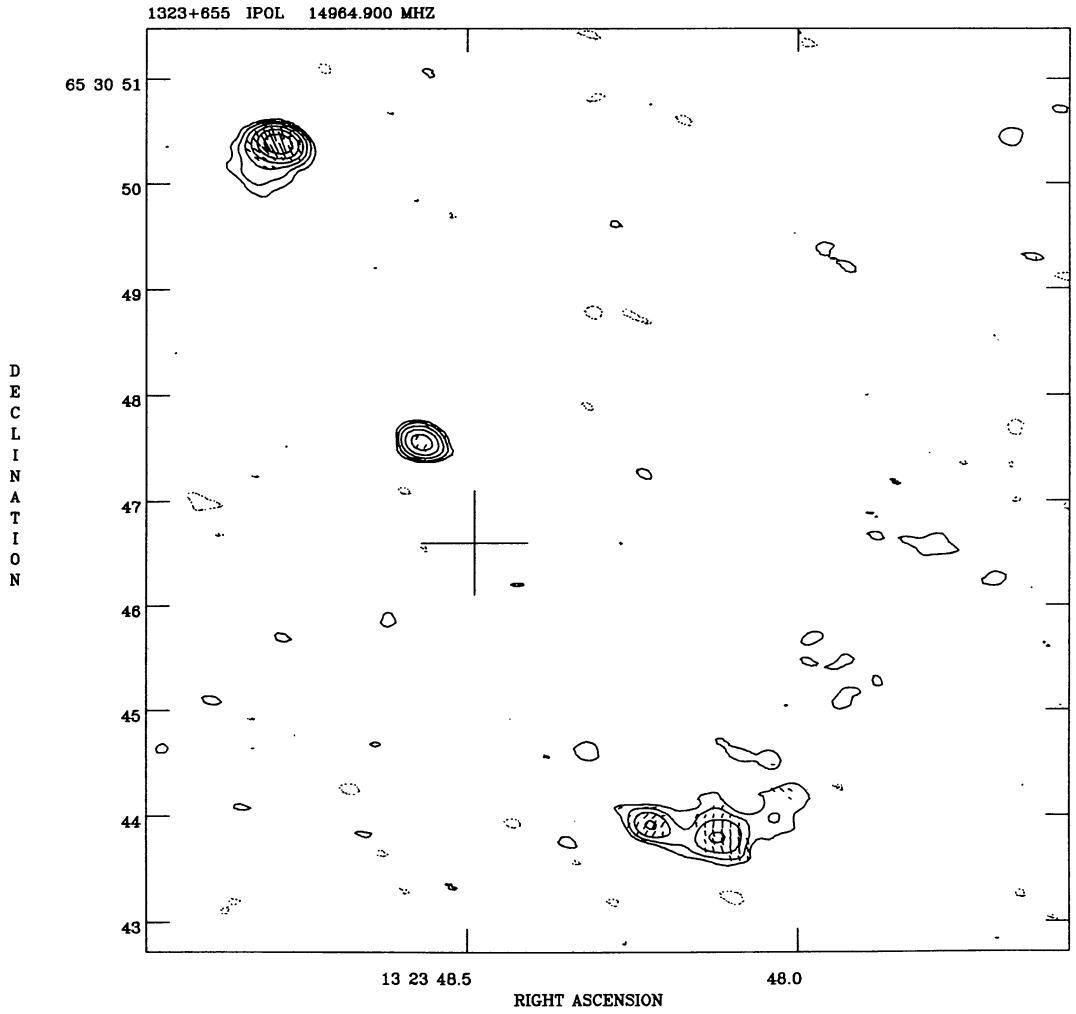

FIG. 101.—1323+655 at 15 GHz; contours $0.3 \times (-1, 1, 2, 4, 8, \cdots)$ mJy beam^{-1}; restoring beam 0.″25 × 0.″18 in P.A. 70°; polarization vector scale 10 mJy beam^{-1} arcsec^{-1}

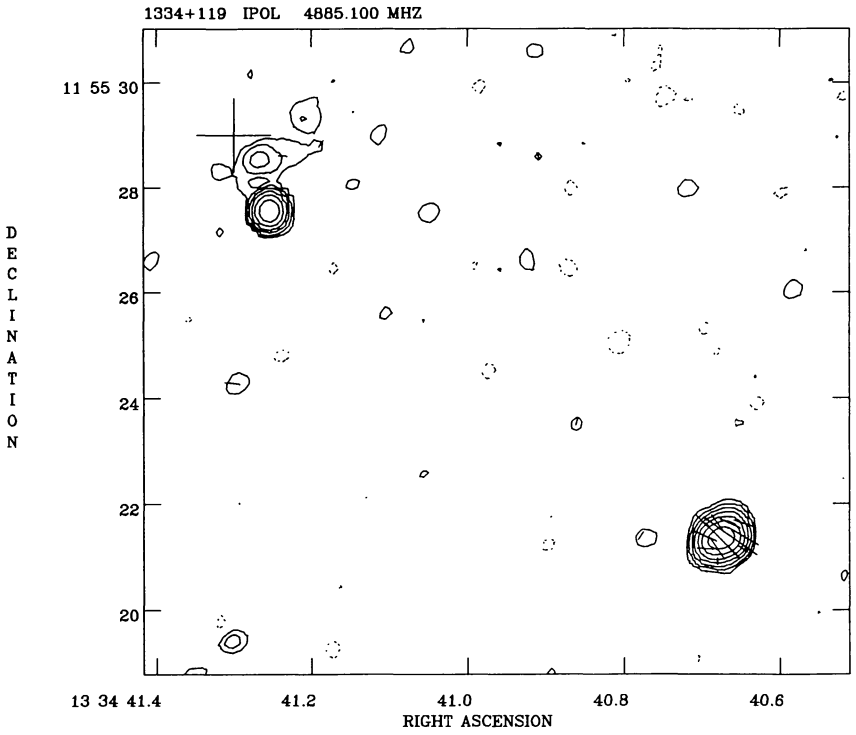

FIG. 102.—1334+119 at 5 GHz; contours $0.3 \times (-1, 1, 2, 4, 8, \cdots)$ mJy beam^{-1}; restoring beam $0''.39 \times 0''.36$ in P.A. 8°; polarization vector scale 2 mJy beam^{-1} arcsec^{-1}.

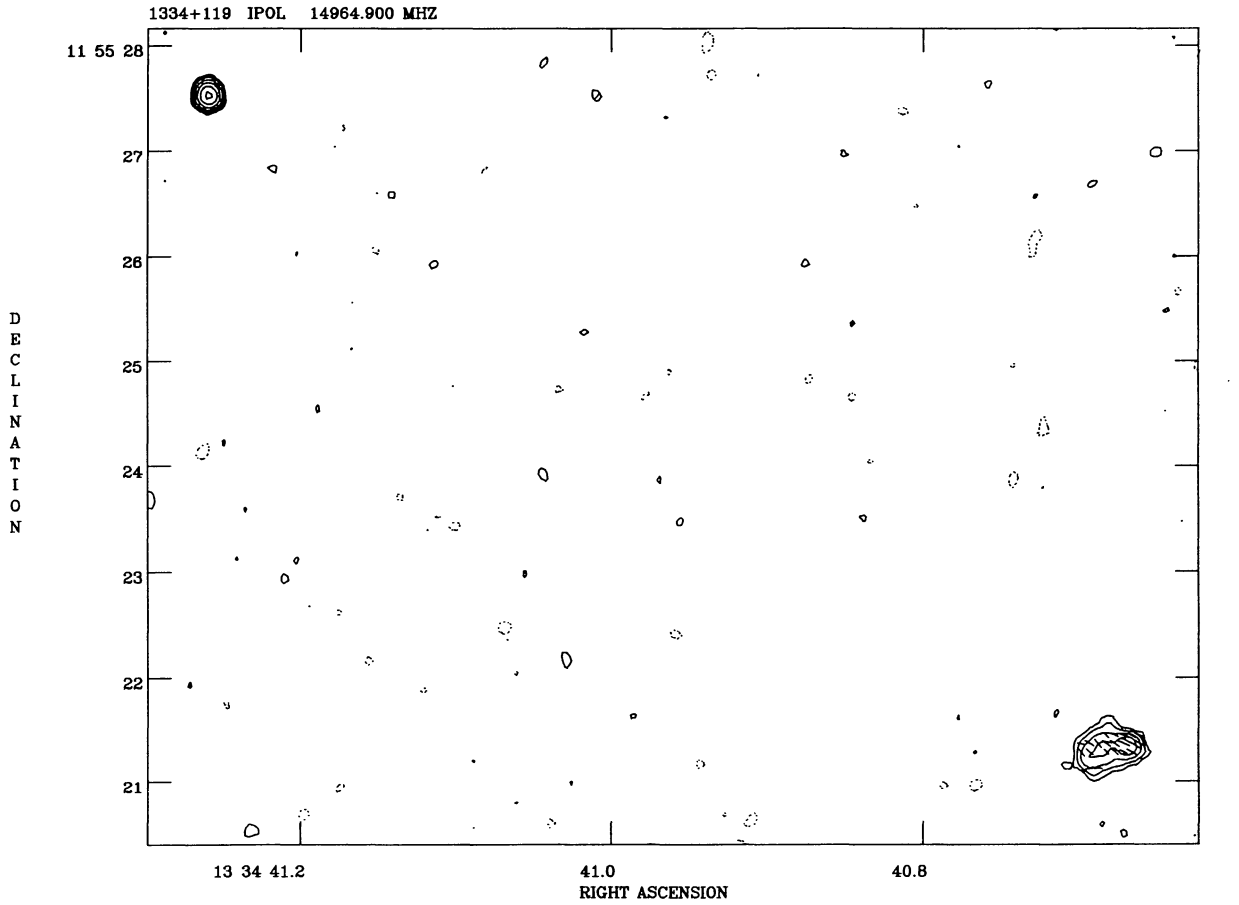

FIG. 103.—1334+119 at 15 GHz; contours $0.3 \times (-1, 1, 2, 4, 8, \cdots)$ mJy beam^{-1}; restoring beam $0''.15 \times 0''.14$ in P.A. 13°; polarization vector scale 5 mJy beam^{-1} arcsec^{-1}.

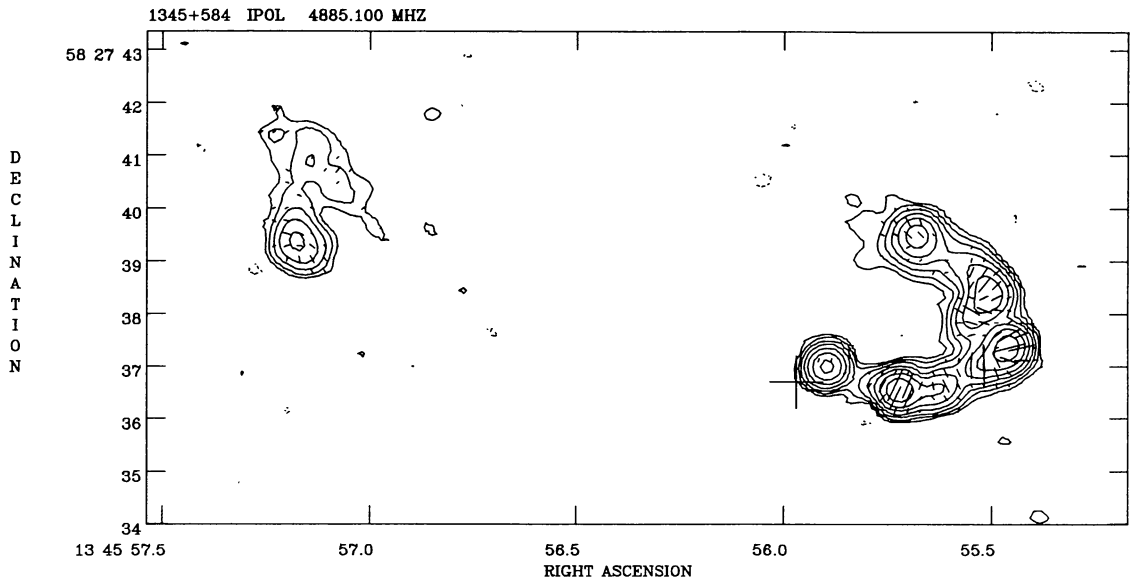

FIG. 104.—1345+584 at 5 GHz; contours $0.3 \times (-1, 1, 2, 4, 8, \cdots)$ mJy beam^{-1}; restoring beam 0.″45; polarization vector scale 5 mJy beam^{-1} arcsec^{-1}

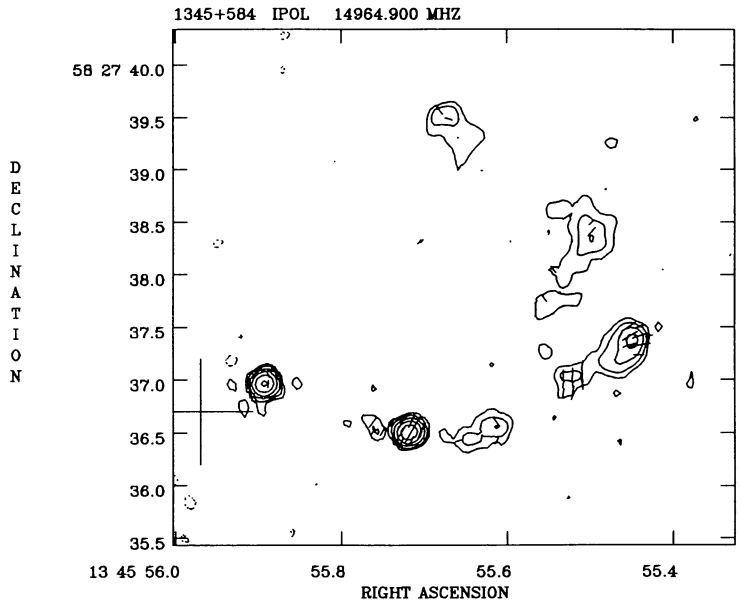

FIG. 105.—1345+584 at 15 GHz; contours $0.45 \times (-1, 1, 2, 4, 8, \cdots)$ mJy beam^{-1}; restoring beam 0.″15; polarization vector scale 5 mJy beam^{-1} arcsec^{-1}.

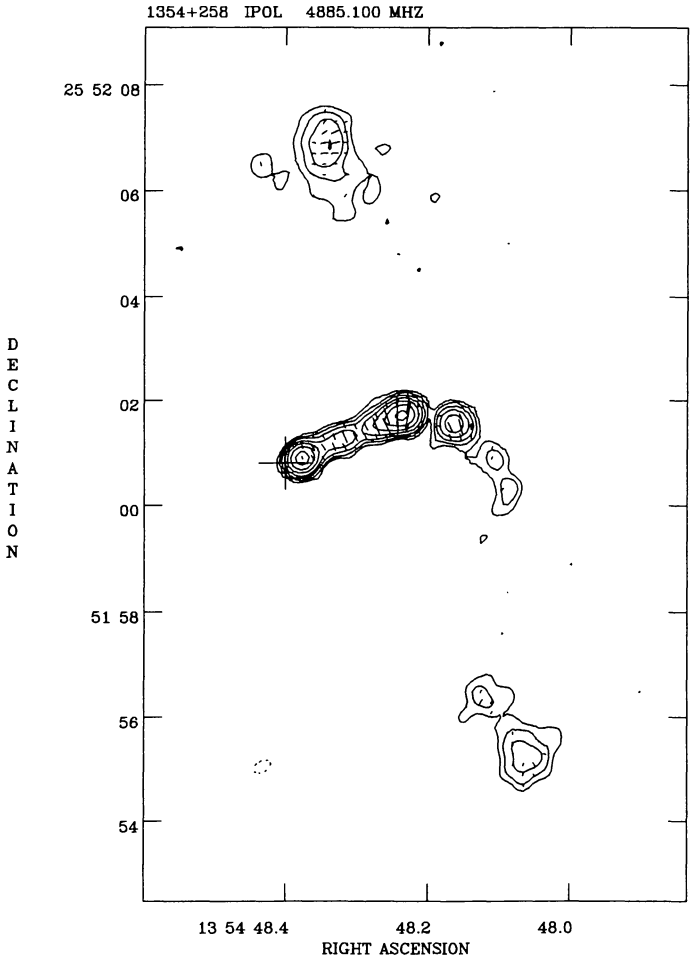

FIG. 106.—1354+258 at 5 GHz; contours $0.3 \times (-1, 1, 2, 4, 8, \cdots)$ mJy beam^{-1}; restoring beam 0.″35 × 0.″33 in P.A. −29°; polarization vector scale 5 mJy beam^{-1} arcsec^{-1}.

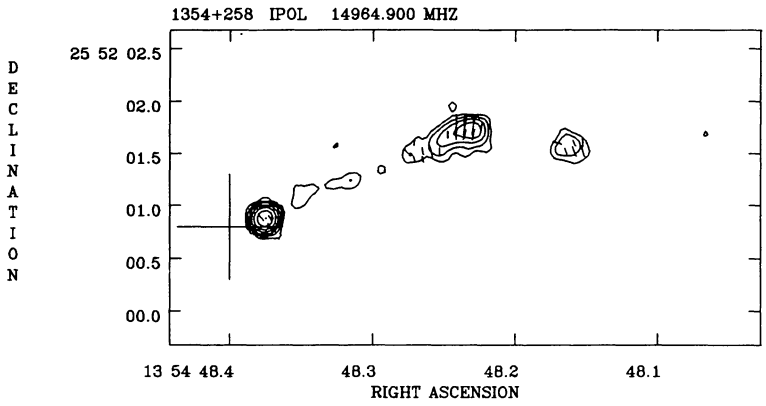

FIG. 107.—1354+258 at 15 GHz; contours $0.3 \times (-1, 1, 2, 4, 8, \cdots)$ mJy beam^{-1}; restoring beam 0.″14; polarization vector scale 5 mJy beam^{-1} arcsec^{-1}

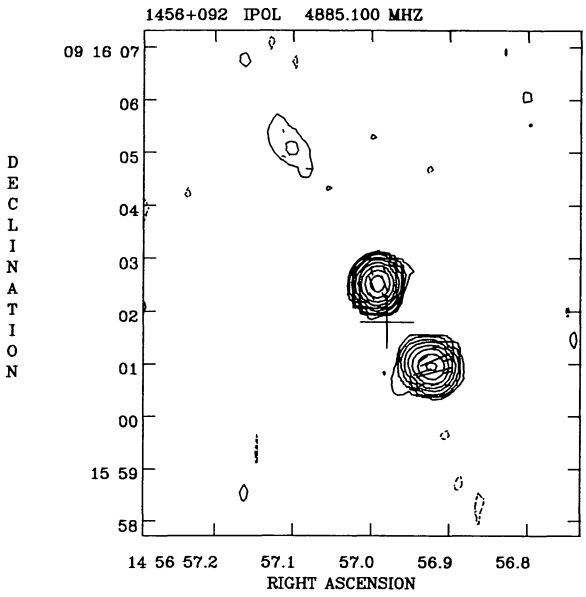

FIG. 108.—1456+092 at 5 GHz; contours $0.45 \times (-1, 1, 2, 4, 8, \cdots)$ mJy beam^{-1}; restoring beam $0''.42 \times 0''.37$ in P.A. 2°; polarization vector scale 5 mJy beam^{-1} arcsec^{-1}.

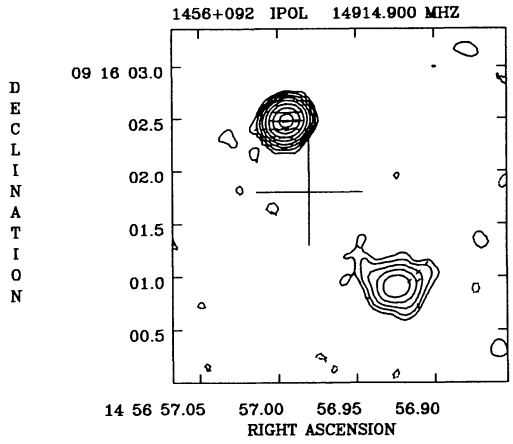

FIG. 109.—1456+092 at 15 GHz; contours $0.45 \times (-1, 1, 2, 4, 8, \cdots)$ mJy beam^{-1}; restoring beam $0''.22 \times 0''.20$ in P.A. −48°; polarization vector scale 20 mJy beam^{-1} arcsec^{-1}.

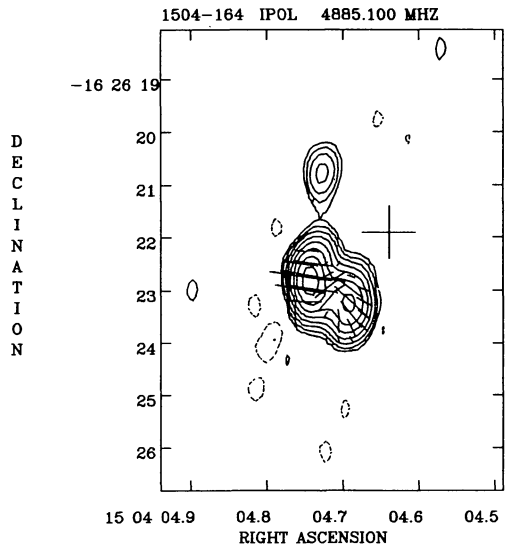

FIG. 110.—1504−164 at 5 GHz; contours $0.6 \times (-1, 1, 2, 4, 8, \cdots)$ mJy beam^{-1}; restoring beam $0''.60 \times 0''.34$ in P.A. −2°; polarization vector scale 5 mJy beam^{-1} arcsec^{-1}.

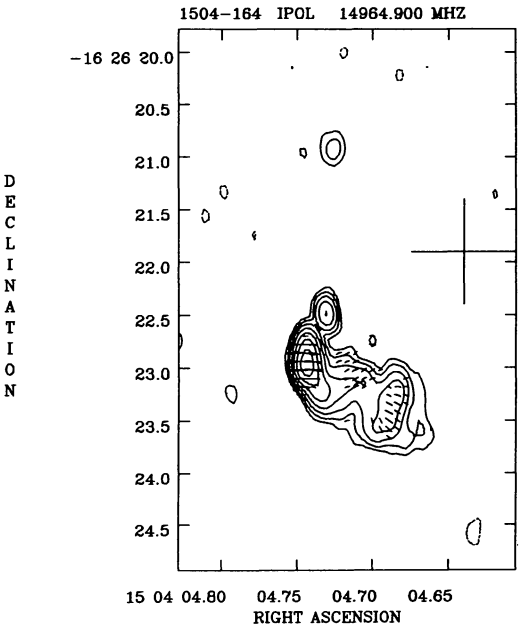

FIG. 111.—1504−164 at 15 GHz; contours $0.3 \times (-1, 1, 2, 4, 8, \cdots)$ mJy beam^{-1}; restoring beam $0''.22 \times 0''.13$ in P.A. 8°; polarization vector scale 5 mJy beam^{-1} arcsec^{-1}.

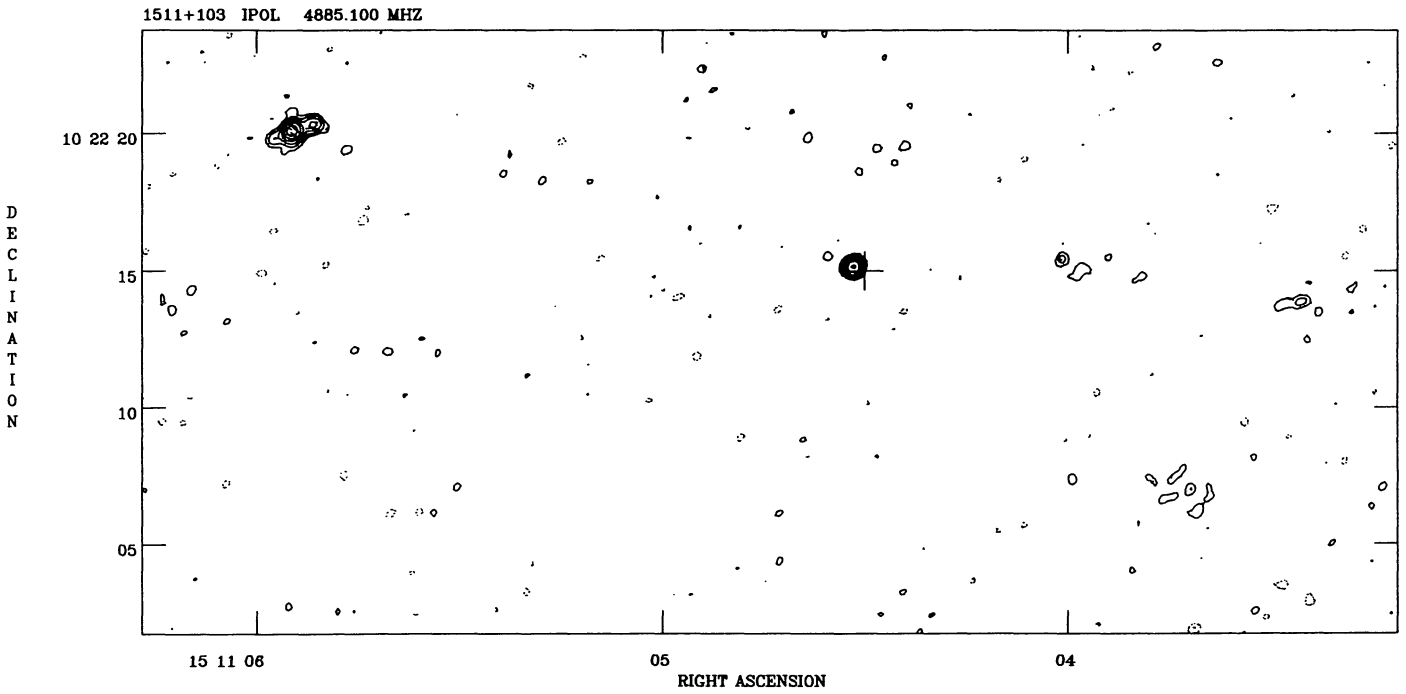

FIG. 112.—1511+103 at 5 GHz; contours $0.2 \times (-1, 1, 2, 4, 8, \cdots)$ mJy beam^{-1}; restoring beam $0''.38 \times 0''.36$ in P.A. $-21°$; polarization vector scale 2 mJy beam^{-1} arcsec^{-1}.

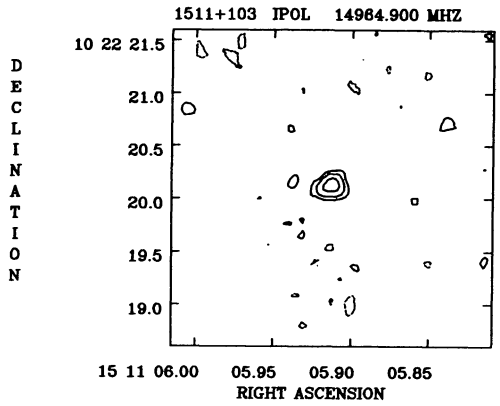

FIG. 113.—1511+103 at 15 GHz; contours $0.3 \times (-1, 1, 2, 4, 8, \cdots)$ mJy beam^{-1}; restoring beam $0''.15 \times 0''.13$ in P.A. 16°.

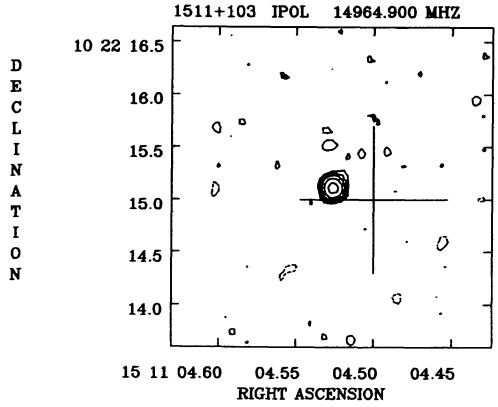

FIG. 114.—Same as Fig. 113

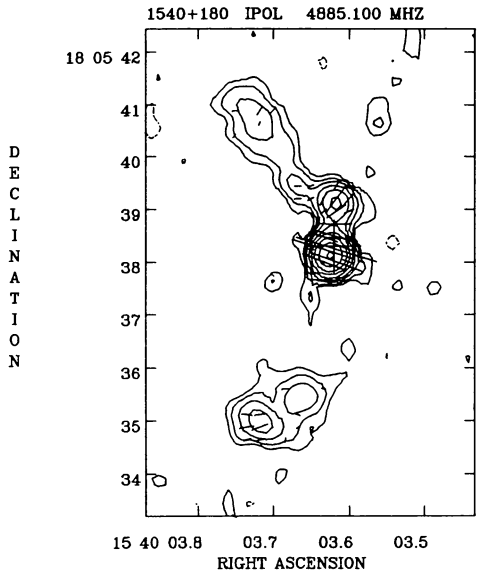

FIG. 115.—1540+180 at 5 GHz; contours $0.6 \times (-1, 1, 2, 4, 8, \cdots)$ mJy beam^{-1}; restoring beam 0″.40; polarization vector scale 5 mJy beam^{-1} arcsec^{-1}.

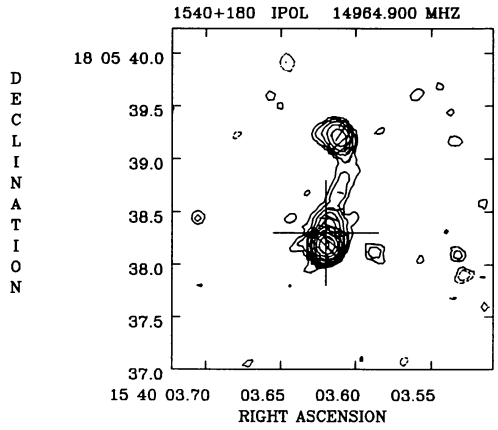

FIG. 116.—1540+180 at 15 GHz; contours $0.2 \times (-1, 1, 2, 4, 8, \cdots)$ mJy beam^{-1}; restoring beam 0″.15 × 0″.13 in P.A. 14°; polarization vector scale 5 mJy beam^{-1} arcsec^{-1}.

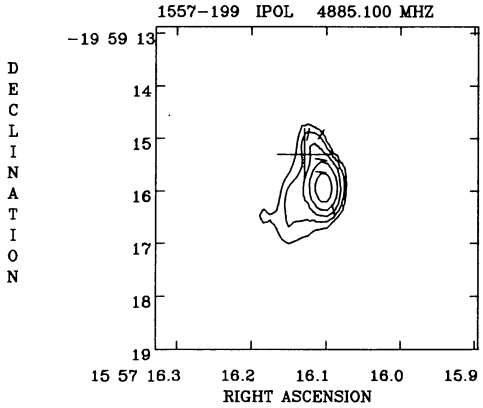

FIG. 117.—1557−199 at 5 GHz; contours $0.45 \times (-1, 1. 2, 4, 8, \cdots)$ mJy beam^{-1}; restoring beam 0″.61 × 0″.34 in P.A. 8°; polarization vector scale 2 mJy beam^{-1} arcsec^{-1}.

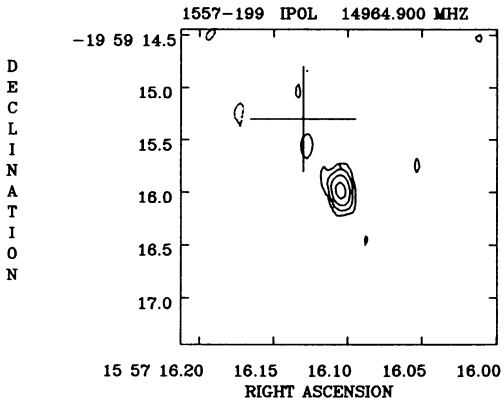

FIG. 118.—1557−199 at 15 GHz; contours $0.45 \times (-1, 1, 2, 4, 8, \cdots)$ mJy beam^{-1}; restoring beam 0″.23 × 0″.13 in P.A. 9°; polarization vector scale 10 mJy beam^{-1} arcsec^{-1}.

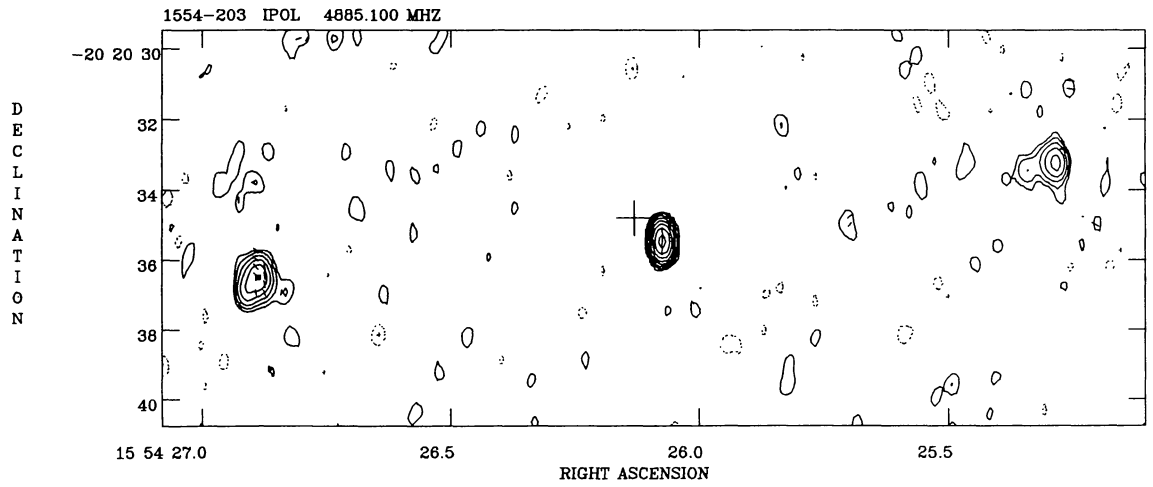

FIG. 119.—1554−203 at 5 GHz; contours $0.2 \times (-1, 1, 2, 4, 8, \cdots)$ mJy beam^{-1}; restoring beam $0''.63 \times 0''.34$ in P.A. 4°; polarization vector scale 2 mJy beam^{-1} arcsec^{-1}.

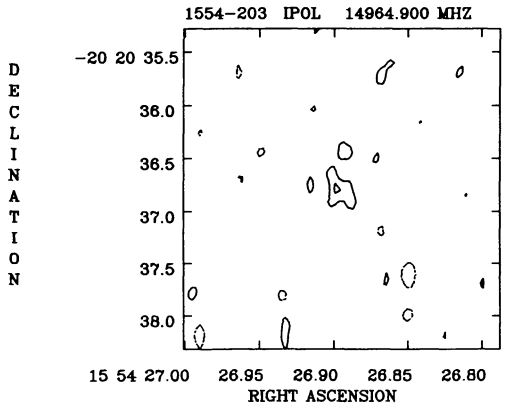

FIG. 120.—1554−203 at 15 GHz; contours $0.3 \times (-1, 1, 2, 4, 8, \cdots)$ mJy beam^{-1}; restoring beam $0''.24 \times 0''.13$ in P.A. 7°; polarization vector scale 5 mJy beam^{-1} arcsec^{-1}.

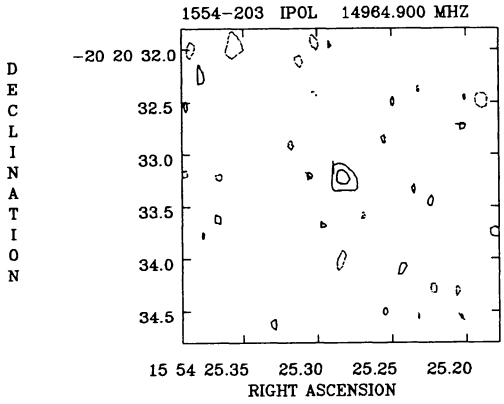

FIG. 121.—Same as Fig. 120

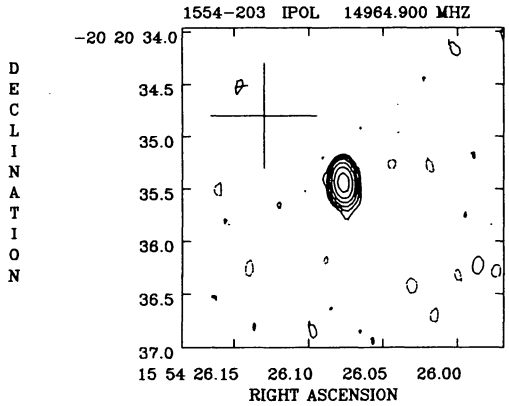

FIG. 122.—Same as Fig. 120

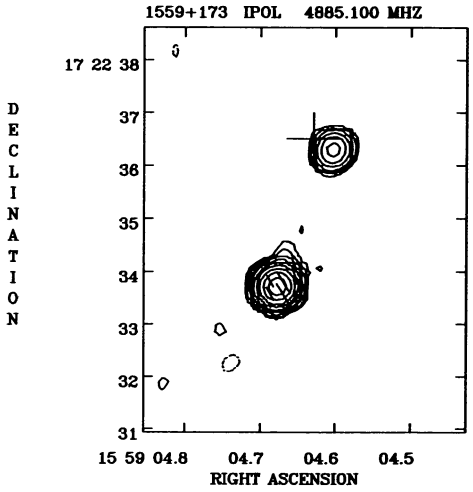

FIG. 123.—1559+173 at 5 GHz; contours $0.6 \times (-1, 1, 2, 4, 8, \cdots)$ mJy beam^{-1}; restoring beam 0.″39; polarization vector scale 5 mJy beam^{-1} arcsec^{-1}

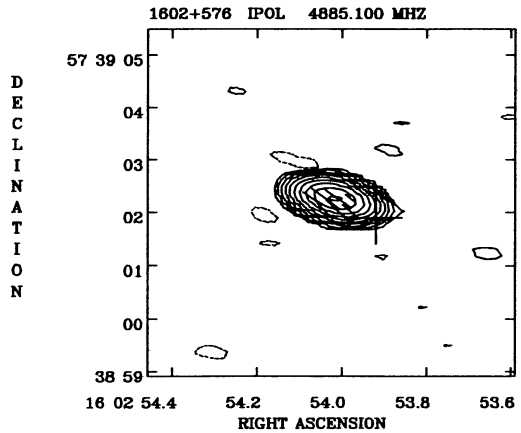

FIG. 124.—1602+576 at 5 GHz; contours $0.6 \times (-1, 1, 2, 4, 8, \cdots)$ mJy beam^{-1}; restoring beam 0.″76 × 0.″34 in P.A. 76°; polarization vector scale 2 mJy beam^{-1} arcsec^{-1}.

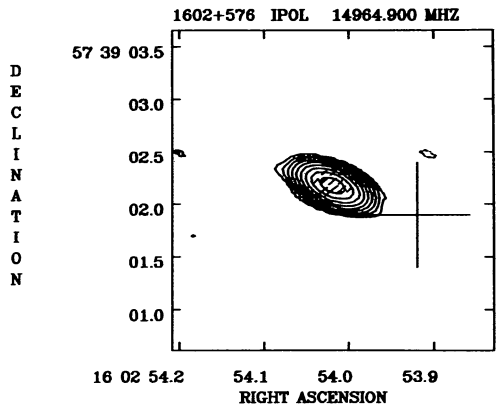

FIG. 125.—1602+576 at 15 GHz; contours $0.6 \times (-1, 1, 2, 4, 8, \cdots)$ mJy beam^{-1}; restoring beam 0.″34 × 0.″16 in P.A. 65°; polarization vector scale 10 mJy beam^{-1} arcsec^{-1}.

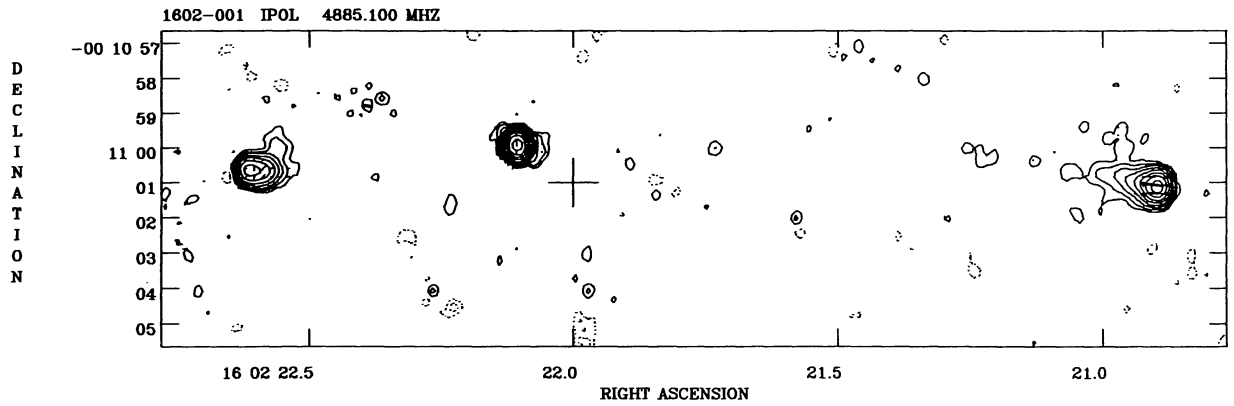

FIG. 126.—1602−001 at 5 GHz; contours $0.3 \times (-1, 1, 2, 4, 8, \cdots)$ mJy beam^{-1}; restoring beam $0\farcs44 \times 0\farcs35$ in P.A. 11°; polarization vector scale 10 mJy beam^{-1} arcsec^{-1}.

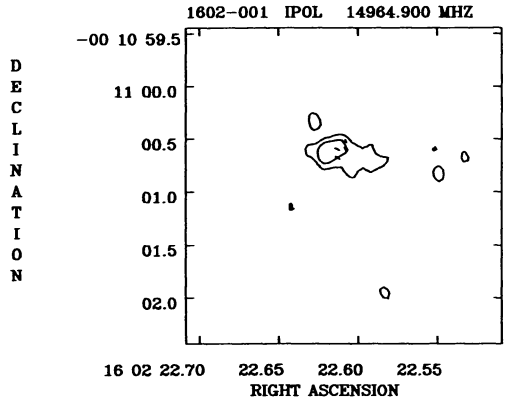

FIG. 127.—1602−001 at 15 GHz; contours $0.6 \times (-1, 1, 2, 4, 8, \cdots)$ mJy beam^{-1}; restoring beam $0\farcs17 \times 0\farcs13$ in P.A. 16°; polarization vector scale 10 mJy beam^{-1} arcsec^{-1}.

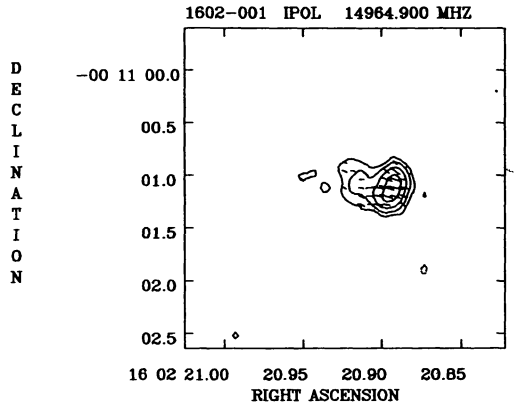

FIG. 128.—Same as Fig. 126

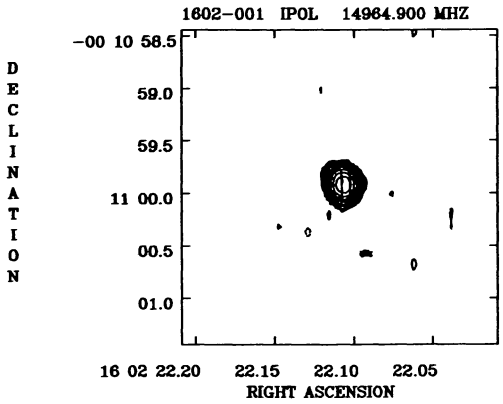

FIG. 129.—Same as Fig. 126

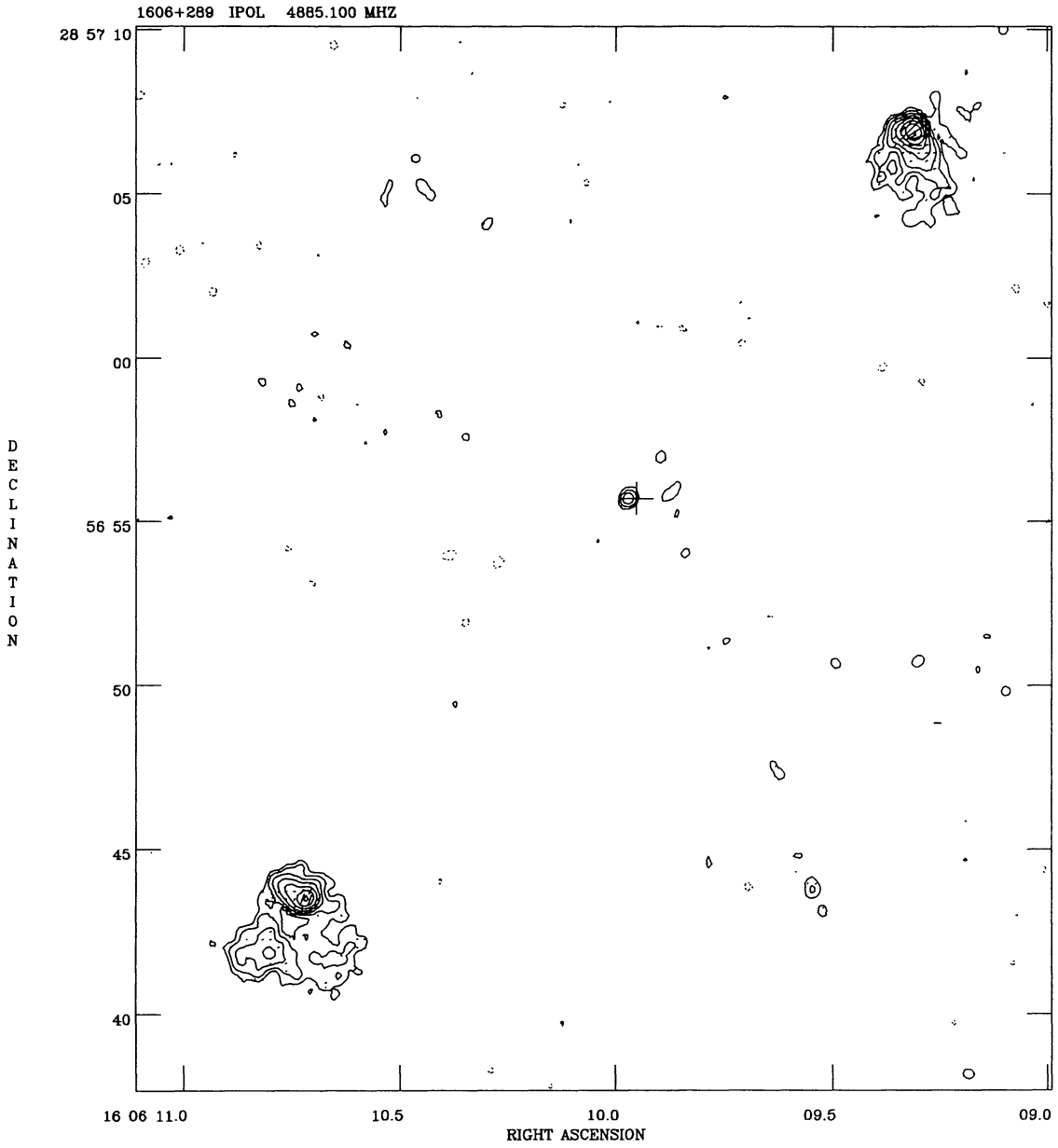

FIG. 130.—1606+289 at 5 GHz; contours $0.2 \times (-1, 1, 2, 4, 8, \cdots)$ mJy beam^{-1}; restoring beam $0''.36 \times 0''.34$ in P.A. $-26°$; polarization vector scale 5 mJy beam^{-1} arcsec^{-1}.

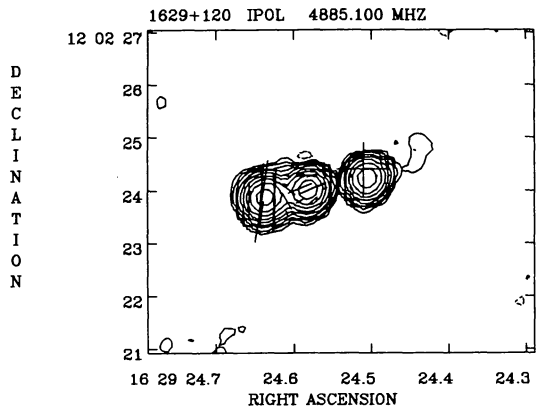

FIG. 131.—1629+120 at 5 GHz; contours $0.6 \times (-1, 1, 2, 4, 8, \cdots)$ mJy beam^{-1}; restoring beam $0''.40 \times 0''.38$ in P.A. $-11°$; polarization vector scale 10 mJy beam^{-1} arcsec^{-1}.

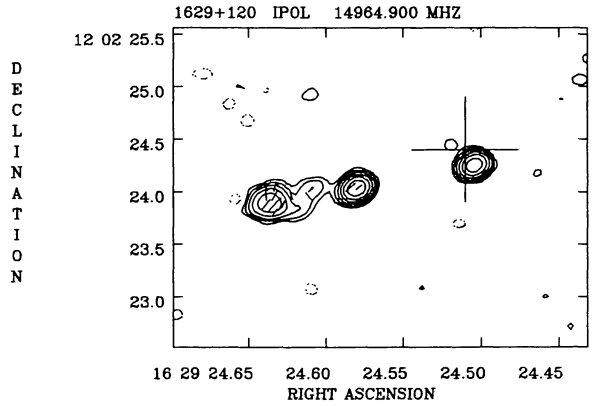

FIG. 132.—1629+120 at 15 GHz; contours $1.5 \times (-1, 1, 2, 4, 8, \cdots)$ mJy beam^{-1}; restoring beam $0''.17 \times 0''.14$ in P.A. $-65°$; polarization vector scale 20 mJy beam^{-1} arcsec^{-1}.

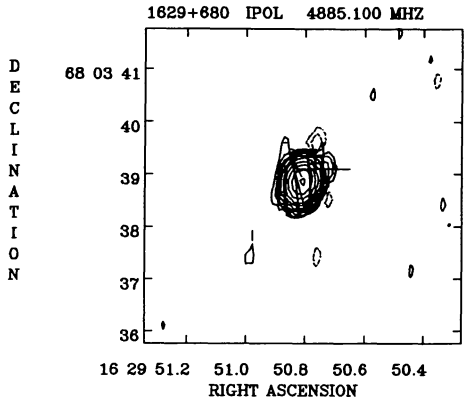

FIG. 133.—1629+680 at 5 GHz; contours $0.6 \times (-1, 1, 2, 4, 8, \cdots)$ mJy beam^{-1}; restoring beam $0''.43 \times 0''.32$ in P.A. $-11°$; polarization vector scale 10 mJy beam^{-1} arcsec^{-1}.

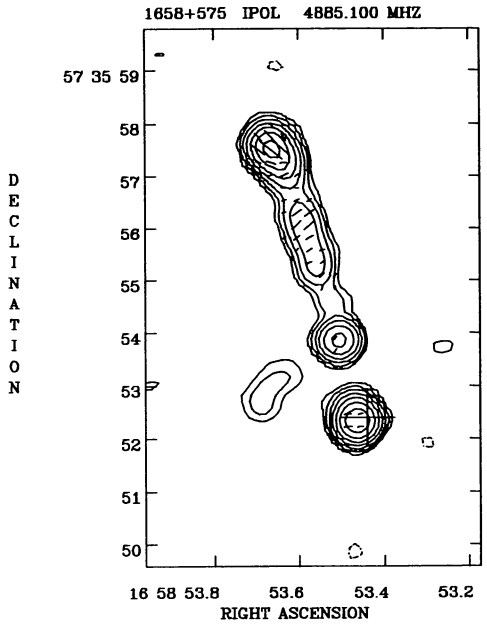

FIG. 134.—1658+575 at 5 GHz; contours $0.3 \times (-1, 1, 2, 4, 8, \cdots)$ mJy beam^{-1}; restoring beam 0".45; polarization vector scale 5 mJy beam^{-1} arcsec^{-1}.

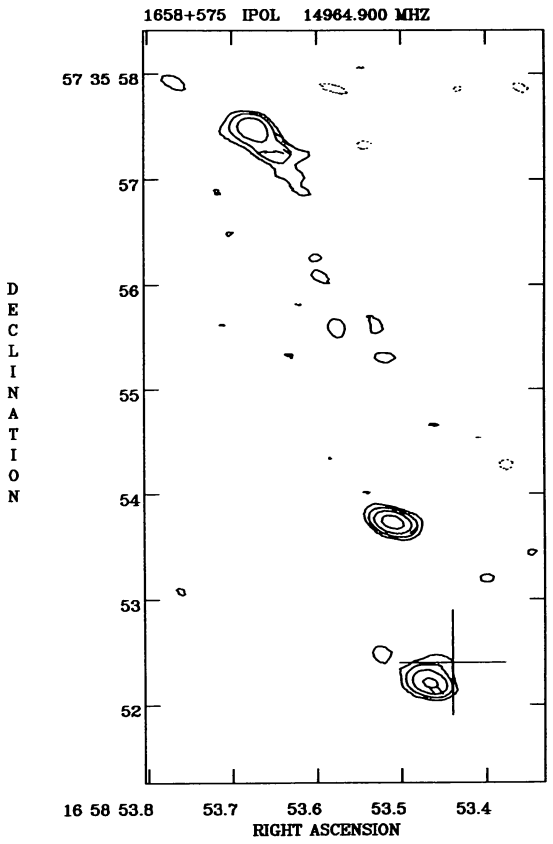

FIG. 135.—1658+575 at 15 GHz; contours $0.45 \times (-1, 1, 2, 4, 8, \cdots)$ mJy beam^{-1}; restoring beam 0".28 × 0".15 in P.A. 74°; polarization vector scale 5 mJy beam^{-1} arcsec^{-1}.

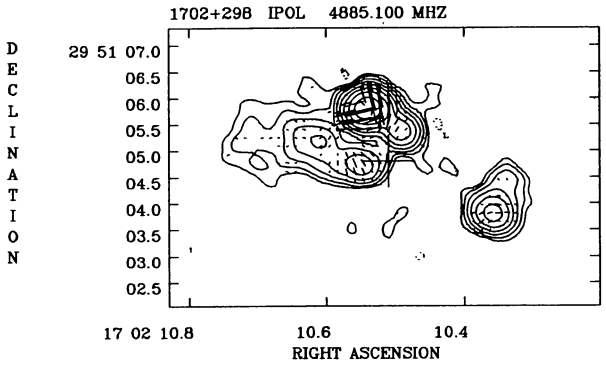

FIG. 136.—1702+298 at 5 GHz; contours $1.0 \times (-1, 1, 2, 4, 8, \cdots)$ mJy beam^{-1}; restoring beam 0".45 × 0".40 in P.A. 70°; polarization vector scale 2 mJy beam^{-1} arcsec^{-1}.

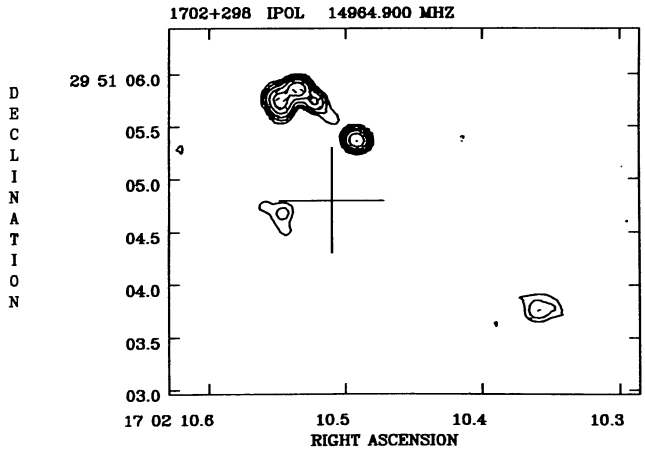

FIG. 137.—1702+298 at 15 GHz; contours $1.5 \times (-1, 1, 2, 4, 8, \cdots)$ mJy beam^{-1}; restoring beam 0".14 × 0".12 in P.A. 70°; polarization vector scale 50 mJy beam^{-1} arcsec^{-1}.

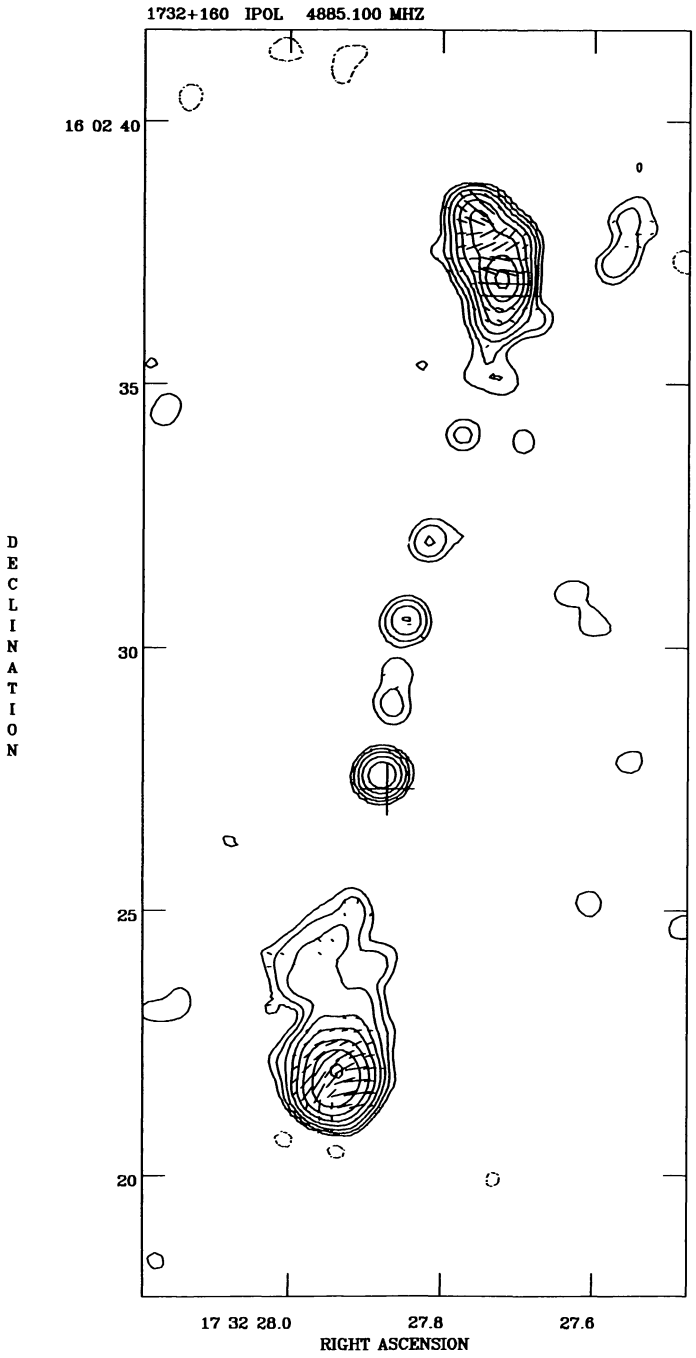

FIG. 138.—1732+160 at 5 GHz; contours $0.3 \times (-1, 1, 2, 4, 8, \cdots)$ mJy beam^{-1}; restoring beam 0".50; polarization vector scale 5 mJy beam^{-1} arcsec^{-1}.

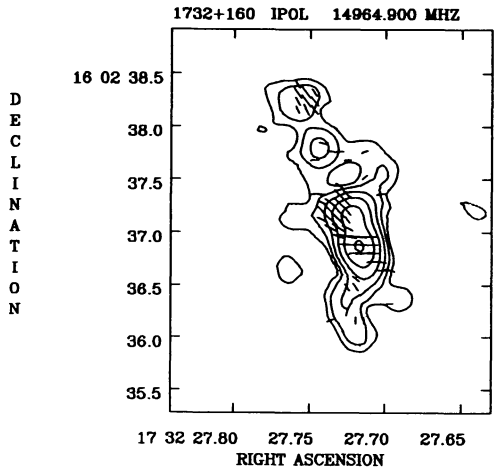

FIG. 139.—1732+160 at 15 GHz; contours $0.3 \times (-1, 1, 2, 4, 8, \cdots)$ mJy beam^{-1}; restoring beam 0".25; polarization vector scale 5 mJy beam^{-1} arcsec^{-1}.

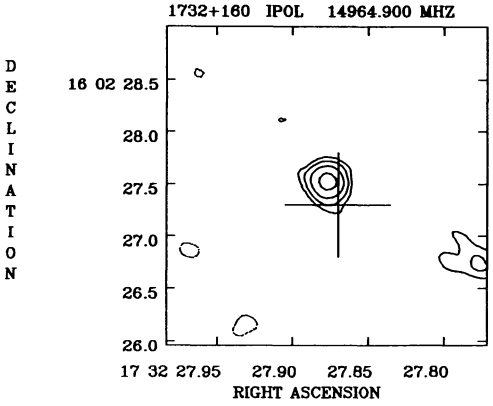

FIG. 140.—Same as Fig. 138

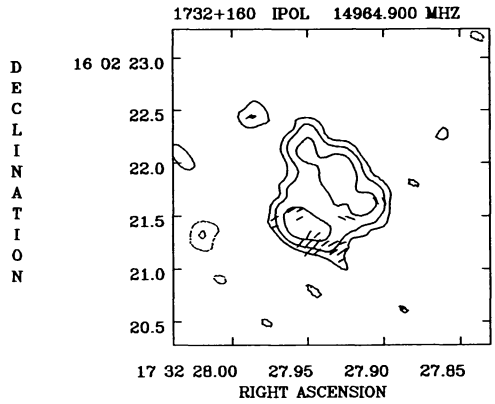

FIG. 141.—Same as Fig. 138

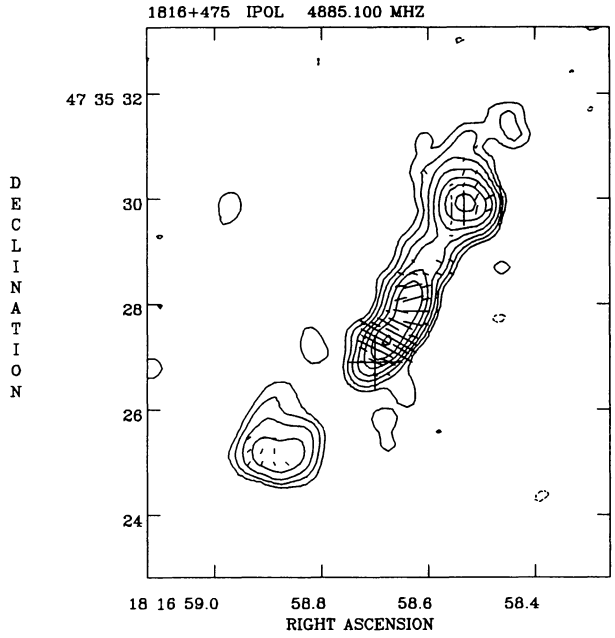

FIG. 142.—1816+475 at 5 GHz; contours $0.3 \times (-1, 1, 2, 4, 8, \cdots)$ mJy beam^{-1}; restoring beam 0.″42; polarization vector scale 5 mJy beam^{-1} arcsec^{-1}

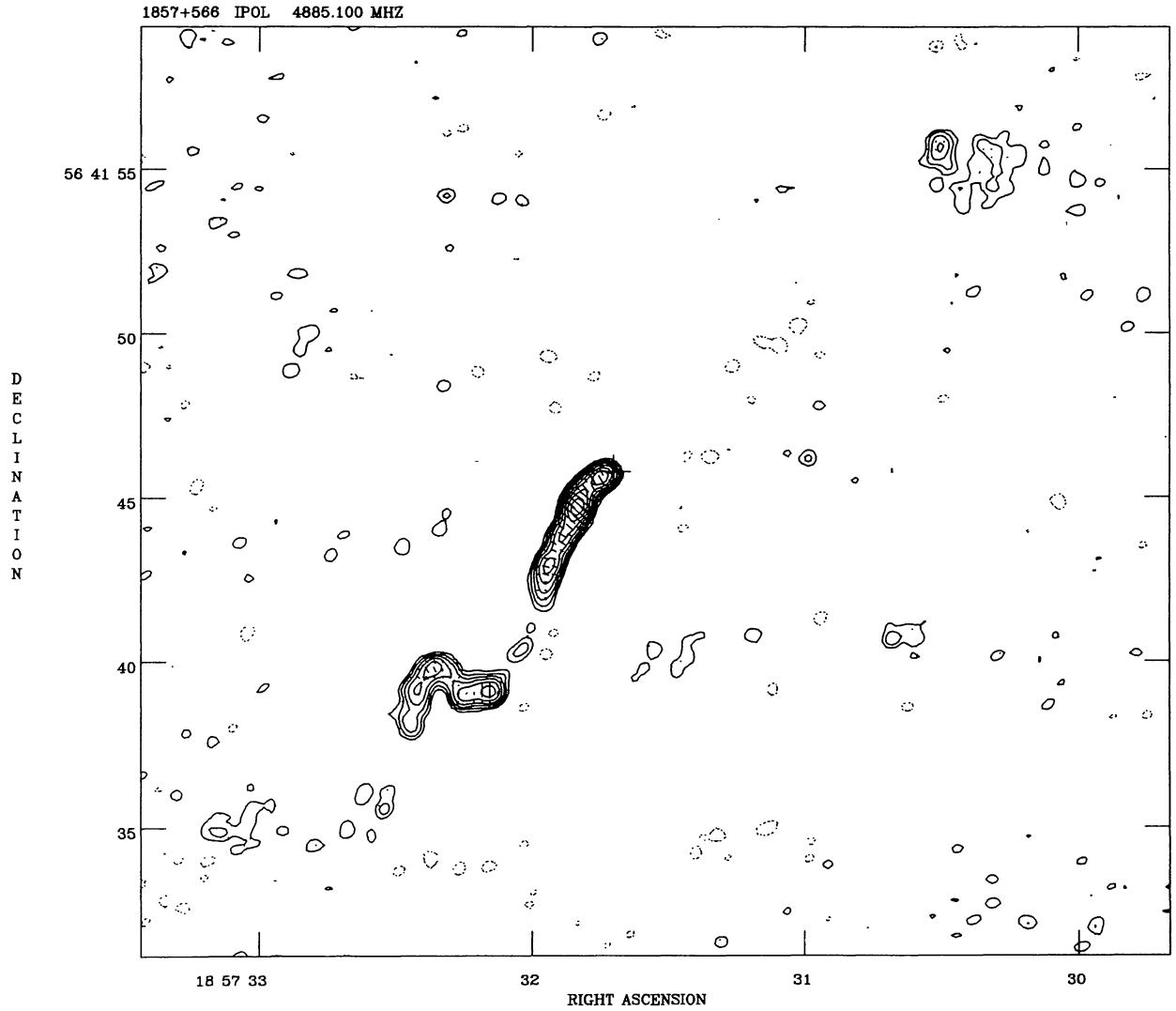

FIG. 143.—1857+566 at 5 GHz; contours $0.2 \times (-1, 1, 2, 4, 8, \cdots)$ mJy beam^{-1}; restoring beam 0.″40; polarization vector scale 10 mJy beam^{-1} arcsec^{-1}

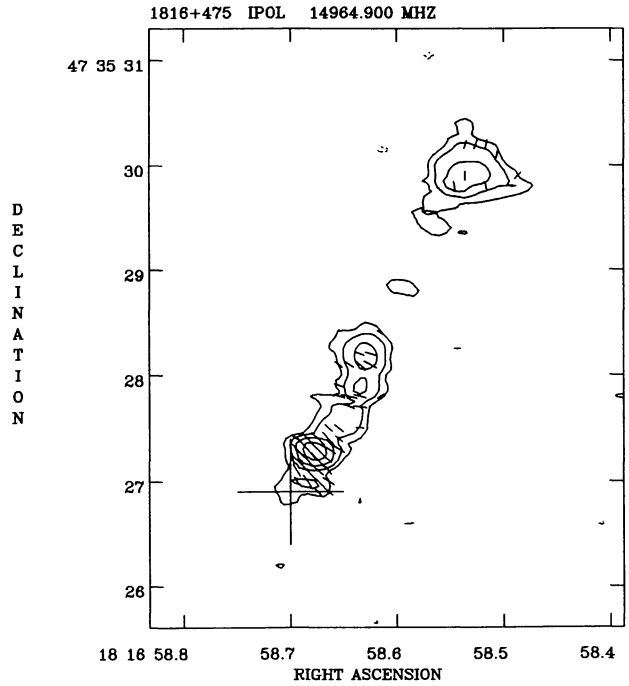

FIG. 144.—1816+475 at 15 GHz; contours $0.45 \times (-1, 1, 2, 4, 8, \cdots)$ mJy beam^{-1}; restoring beam $0''.26 \times 0''.15$ in P.A. 72°; polarization vector scale 5 mJy beam^{-1} arcsec^{-1}.

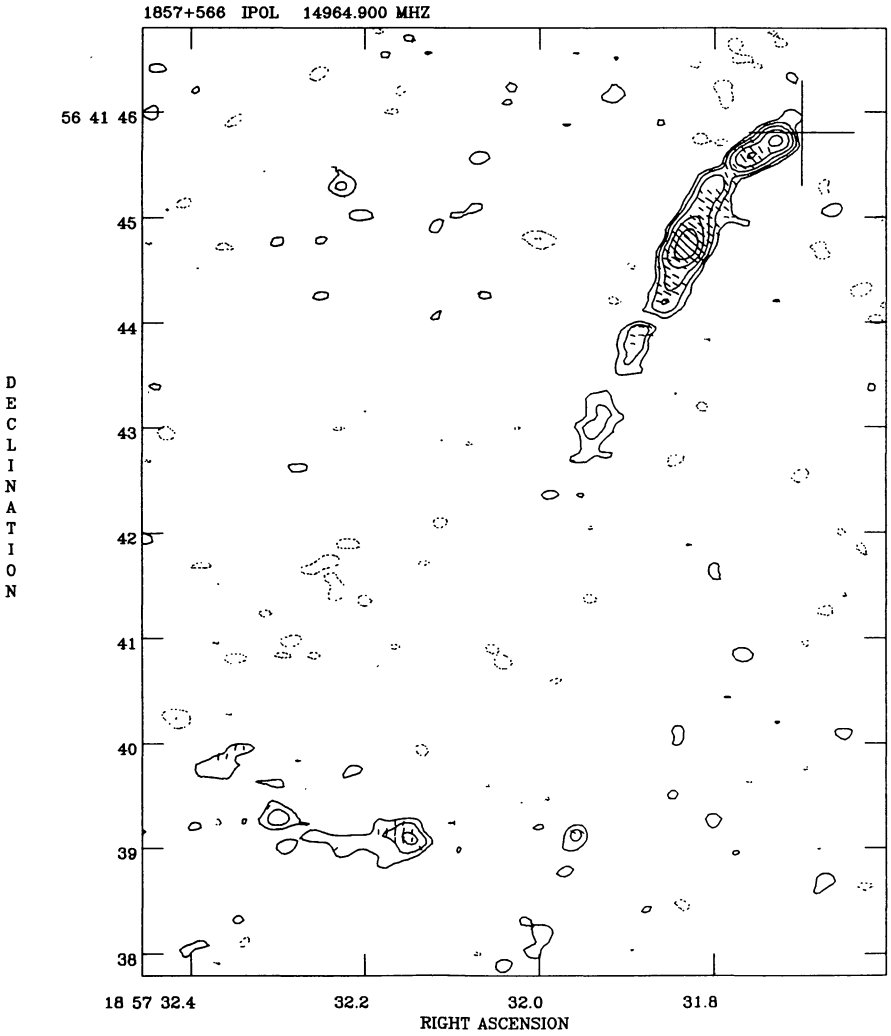

FIG. 145.—1857+566 at 15 GHz; contours $0.3 \times (-1, 1, 2, 4, 8, \cdots)$ mJy beam^{-1}; restoring beam $0''.20 \times 0''.16$ in P.A. 83°; polarization vector scale 10 mJy beam^{-1} arcsec^{-1}.

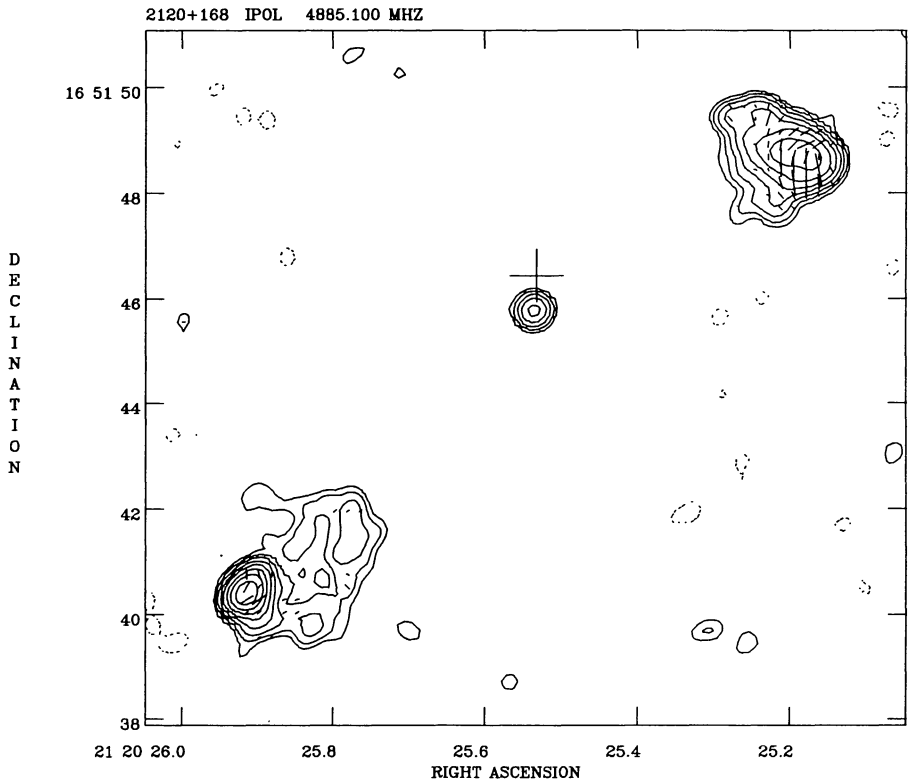

FIG. 146.—2120+168 at 5 GHz; contours $0.3 \times (-1, 1, 2, 4, 8, \cdots)$ mJy beam^{-1}; restoring beam 0".37; polarization vector scale 5 mJy beam^{-1} arcsec^{-1}

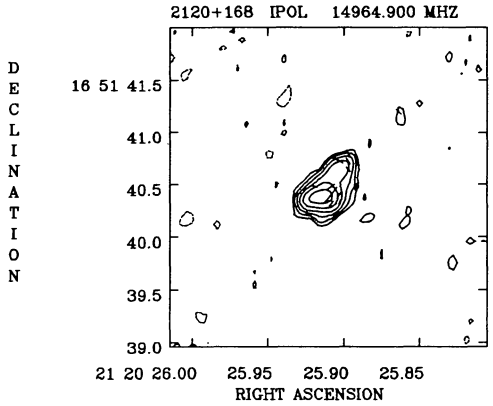

FIG. 147.—2120+168 at 15 GHz; contours $0.2 \times (-1, 1, 2, 4, 8, \cdots)$ mJy beam^{-1}; restoring beam 0".14; polarization vector scale 5 mJy beam^{-1} arcsec^{-1}.

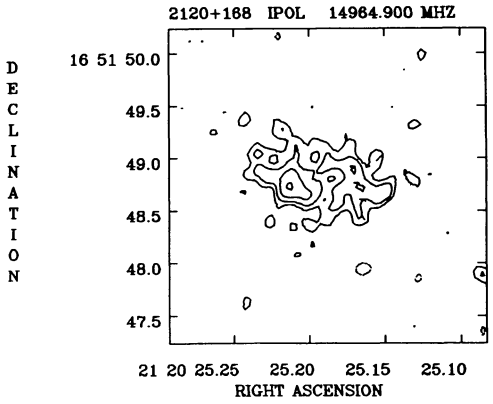

FIG. 148.—Same as Fig. 146

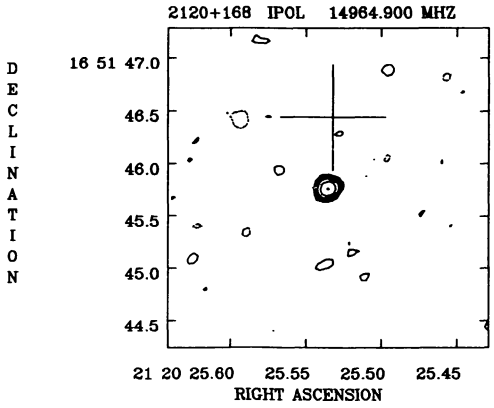

FIG. 149.—Same as Fig. 148

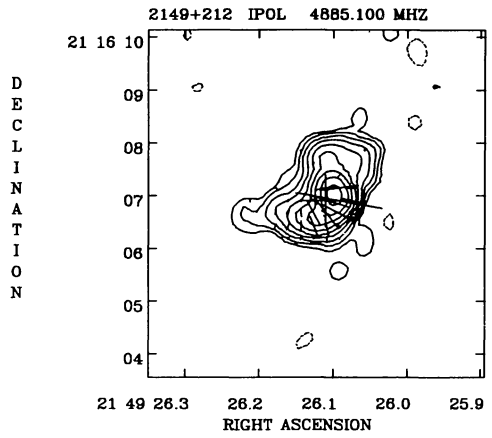

FIG. 150.—2149+212 at 5 GHz; contours $0.45 \times (-1, 1, 2, 4, 8, \cdots)$ mJy beam^{-1}; restoring beam $0''.39 \times 0''.36$ in P.A. $-56°$; polarization vector scale 10 mJy beam^{-1} arcsec^{-1}.

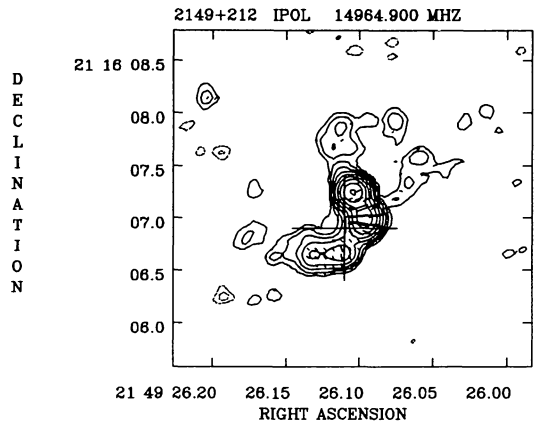

FIG. 151.—2149+212 at 15 GHz; contours $0.3 \times (-1, 1, 2, 4, 8, \cdots)$ mJy beam^{-1}; restoring beam $0''.16$; polarization vector scale 20 mJy beam^{-1} arcsec^{-1}.

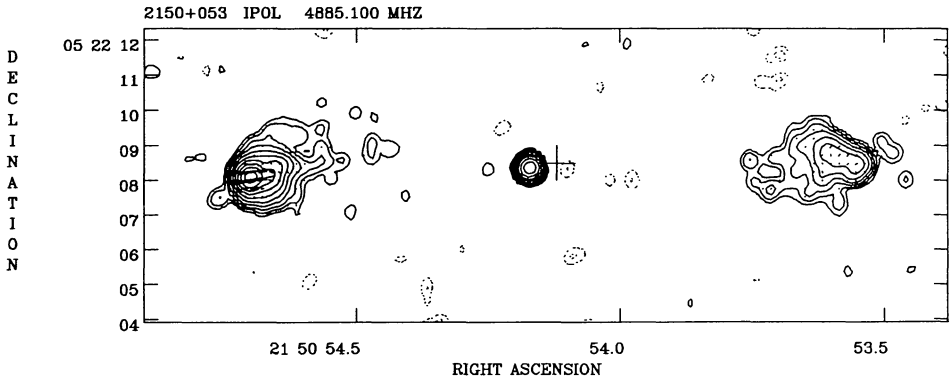

FIG. 152.—2150+053 at 5 GHz; contours $0.15 \times (-1, 1, 2, 4, 8, \cdots)$ mJy beam^{-1}; restoring beam $0''.39 \times 0''.37$ in P.A. 1°; polarization vector scale 20 mJy beam^{-1} arcsec^{-1}.

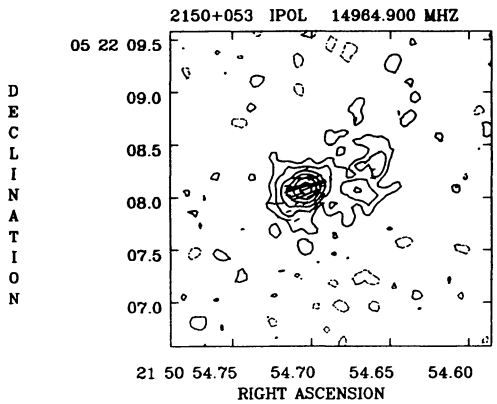

FIG. 153.—2150+053 at 15 GHz; contours $0.6 \times (-1, 1, 2, 4, 8, \cdots)$ mJy beam^{-1}; restoring beam $0''.13 \times 0''.12$ in P.A. $-17°$; polarization vector scale 20 mJy beam^{-1} arcsec^{-1}.

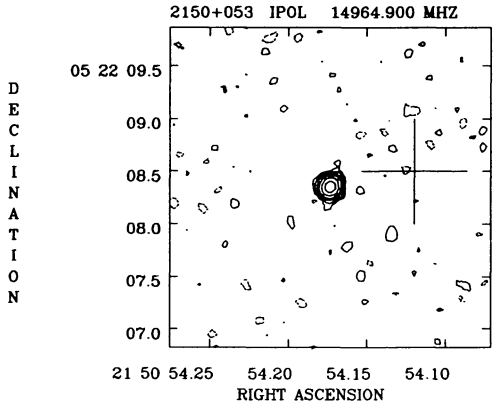

FIG. 154.—Same as Fig. 153

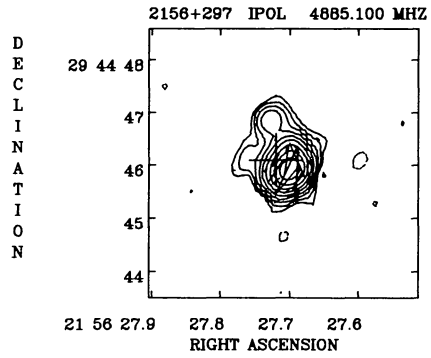

FIG. 155.—2156+297 at 5 GHz; contours $0.6 \times (-1, 1, 2, 4, 8, \cdots)$ mJy beam^{-1}; restoring beam 0.″35; polarization vector scale 10 mJy beam^{-1} arcsec^{-1}.

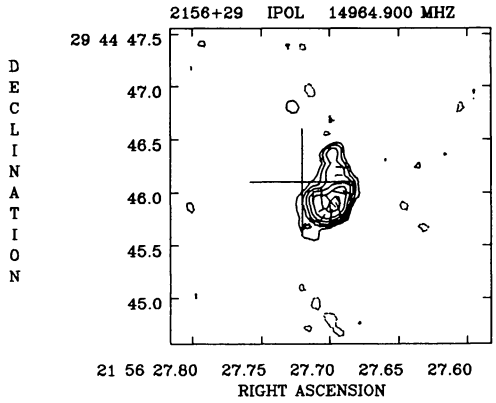

FIG. 156.—2156+297 at 15 GHz; contours $1.0 \times (-1, 1, 2, 4, 8, \cdots)$ mJy beam^{-1}; restoring beam 0.″12; polarization vector scale 20 mJy beam^{-1} arcsec^{-1}.

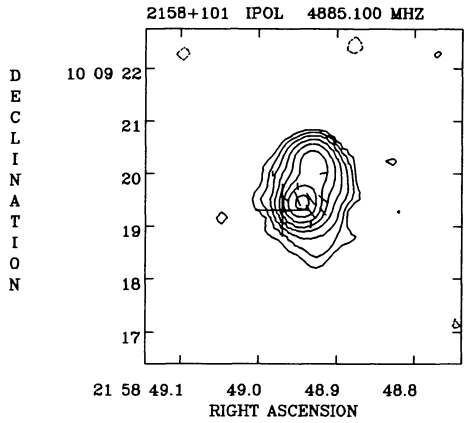

FIG. 157.—2158+101 at 5 GHz; contours $0.45 \times (-1, 1, 2, 4, 8, \cdots)$ mJy beam^{-1}; restoring beam 0.″39; polarization vector scale 5 mJy beam^{-1} arcsec^{-1}.

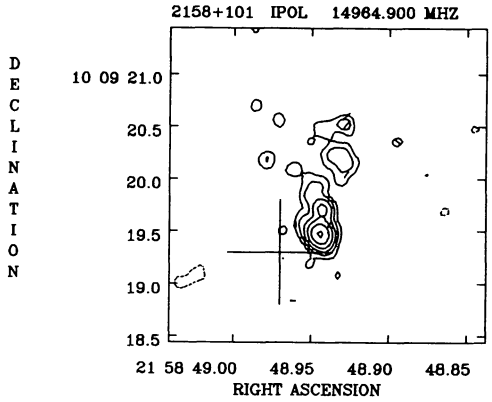

FIG. 158.—2158+101 at 15 GHz; contours $0.45 \times (-1, 1, 2, 4, 8, \cdots)$ mJy beam^{-1}; restoring beam $0.''15 \times 0.''13$ in P.A. 30°; polarization vector scale 10 mJy beam^{-1} arcsec^{-1}.

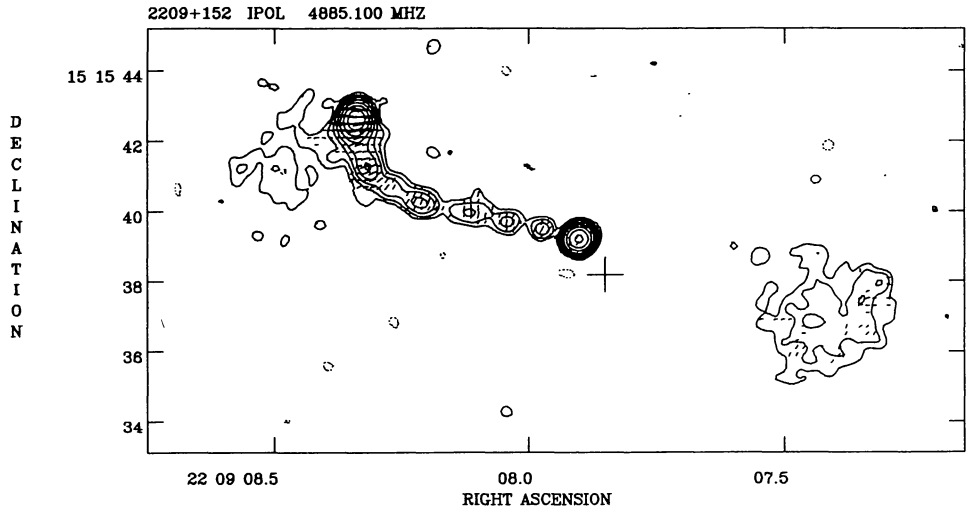

FIG. 159.—2209+152 at 5 GHz; contours $0.15 \times (-1, 1, 2, 4, 8, \cdots)$ mJy beam^{-1}; restoring beam 0.″45; polarization vector scale 2 mJy beam^{-1} arcsec^{-1}

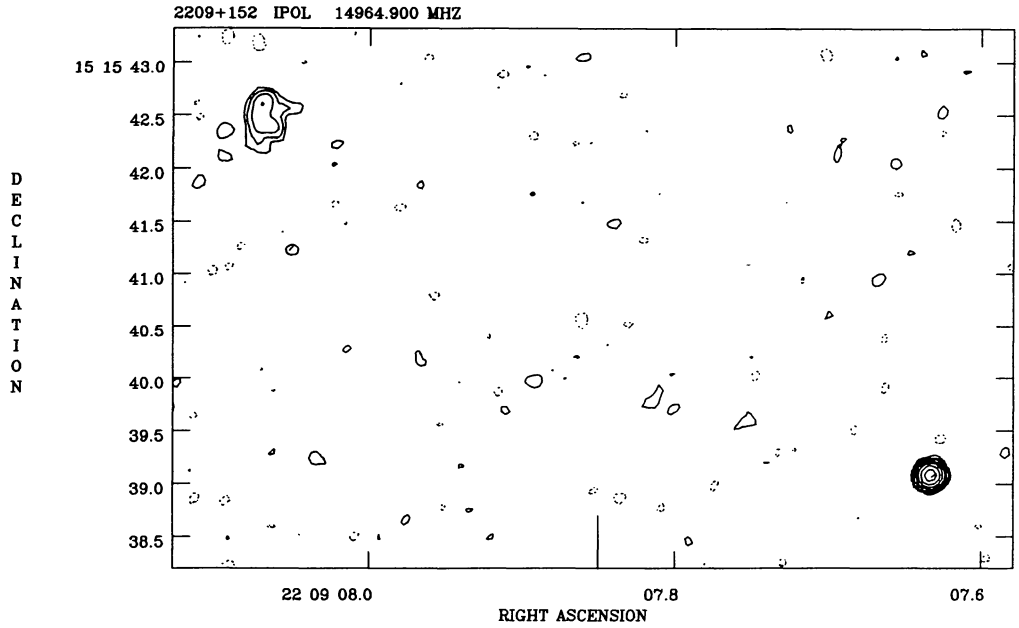

FIG. 160.—2209+152 at 15 GHz; contours $0.2 \times (-1, 1, 2, 4, 8, \cdots)$ mJy beam^{-1}; restoring beam 0.″14; polarization vector scale 5 mJy beam^{-1} arcsec^{-1}

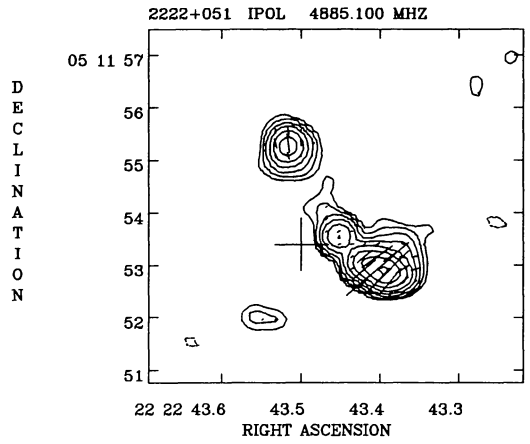

FIG. 161.—2222+051 at 5 GHz; contours $0.6 \times (-1, 1, 2, 4, 8, \cdots)$ mJy beam^{-1}; restoring beam 0″.39; polarization vector scale 10 mJy beam^{-1} arcsec^{-1}.

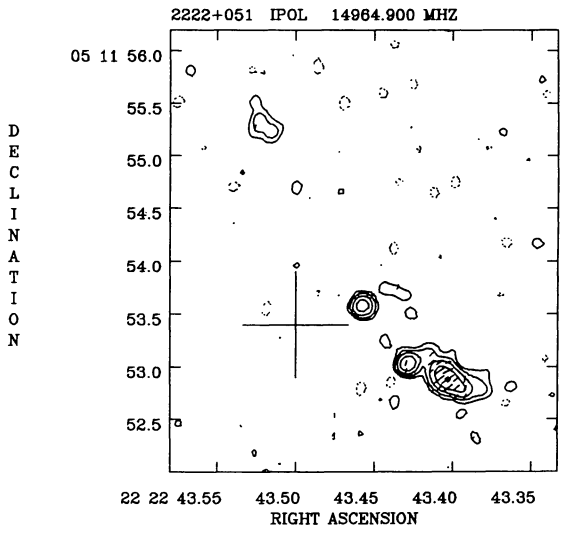

FIG. 162.—2222+051 at 15 GHz; contours $0.6 \times (-1, 1, 2, 4, 8, \cdots)$ mJy beam^{-1}; restoring beam 0″.13 × 0″.12 in P.A. −33°; polarization vector scale 20 mJy beam^{-1} arcsec^{-1}.

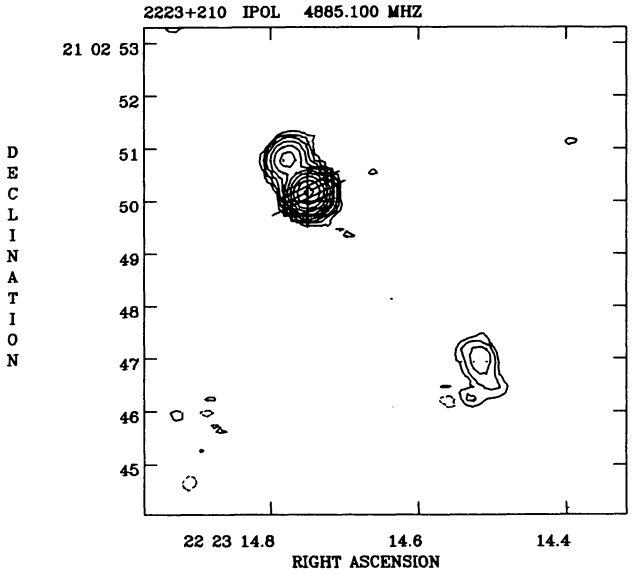

FIG. 163.—2223+210 at 5 GHz; contours $1.5 \times (-1, 1, 2, 4, 8, \cdots)$ mJy beam^{-1}; restoring beam 0″.40 × 0″.37 in P.A. −14°; polarization vector scale 50 mJy beam^{-1} arcsec^{-1}.

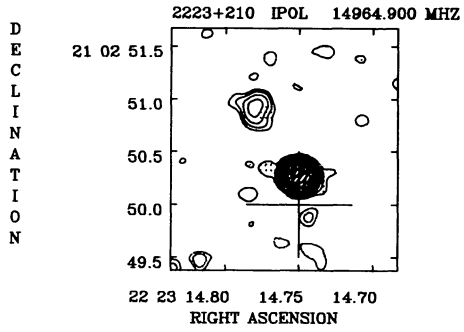

FIG. 164.—2223+210 at 15 GHz; contours $0.6 \times (-1, 1, 2, 4, 8, \cdots)$ mJy beam^{-1}; restoring beam 0″.14; polarization vector scale 100 mJy beam^{-1} arcsec^{-1}.

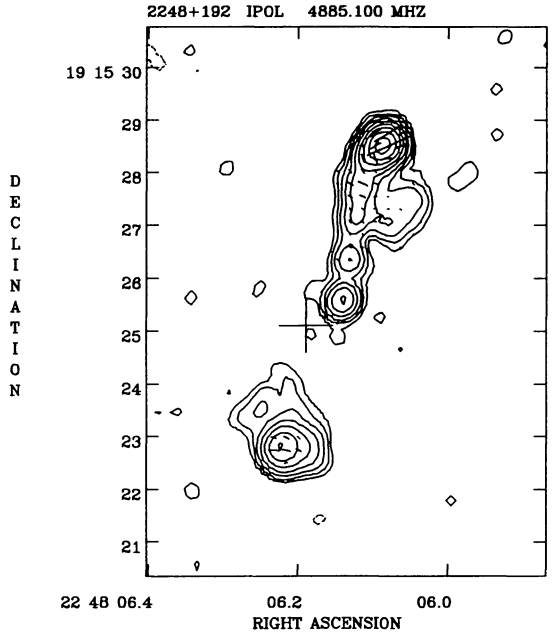

FIG. 165.—2248+192 at 5 GHz; contours $0.3 \times (-1, 1, 2, 4, 8, \cdots)$ mJy beam^{-1}; restoring beam $0''.39 \times 0''.36$ in P.A. $-8°$; polarization vector scale 10 mJy beam^{-1} arcsec^{-1}.

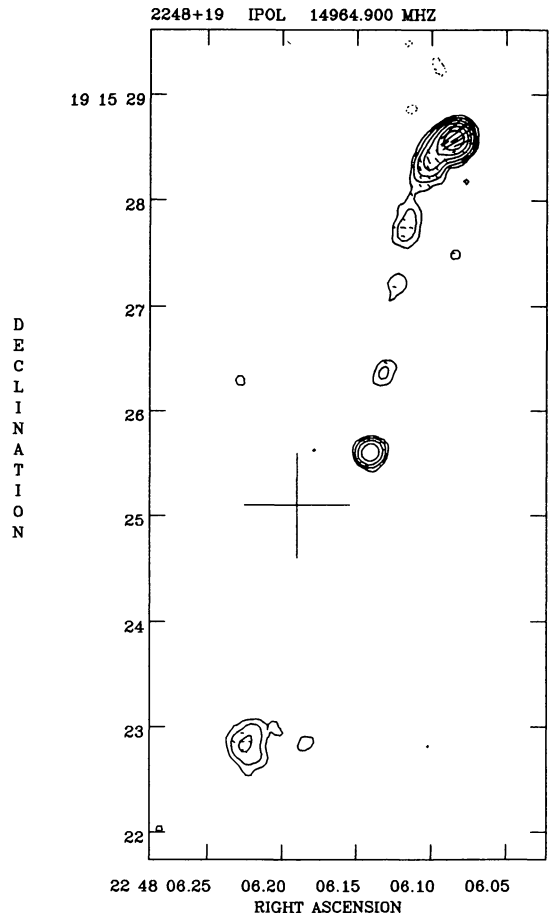

FIG. 166.—2248+192 at 15 GHz; contours $0.6 \times (-1, 1, 2, 4, 8, \cdots)$ mJy beam^{-1}; restoring beam $0''.17 \times 0''.16$ in P.A. $-50°$; polarization vector scale 20 mJy beam^{-1} arcsec^{-1}.

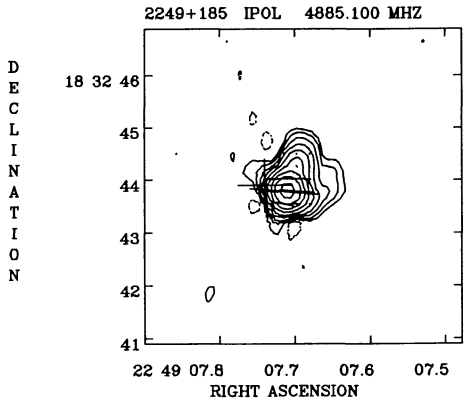

FIG. 167.—2249+185 at 5 GHz; contours $1.5 \times (-1, 1, 2, 4, 8, \cdots)$ mJy beam^{-1}; restoring beam $0''.37$; polarization vector scale 50 mJy beam^{-1} arcsec^{-1}

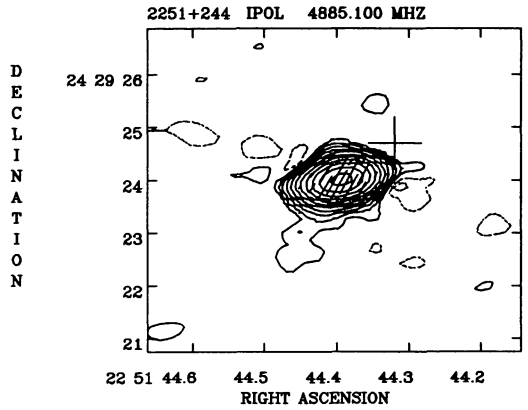

FIG. 168.—2251+244 at 5 GHz; contours $0.6 \times (-1, 1, 2, 4, 8, \cdots)$ mJy beam^{-1}; restoring beam $0''.69 \times 0''.37$ in P.A. $-81°$; polarization vector scale 20 mJy beam^{-1} arcsec^{-1}.

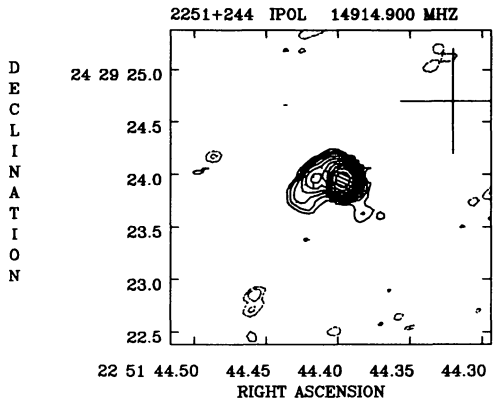

FIG. 169.—2251+244 at 15 GHz; contours $0.3 \times (-1, 1, 2, 4, 8, \cdots)$ mJy beam^{-1}; restoring beam $0''.14 \times 0''.13$ in P.A. 17°; polarization vector scale 50 mJy beam^{-1} arcsec^{-1}.

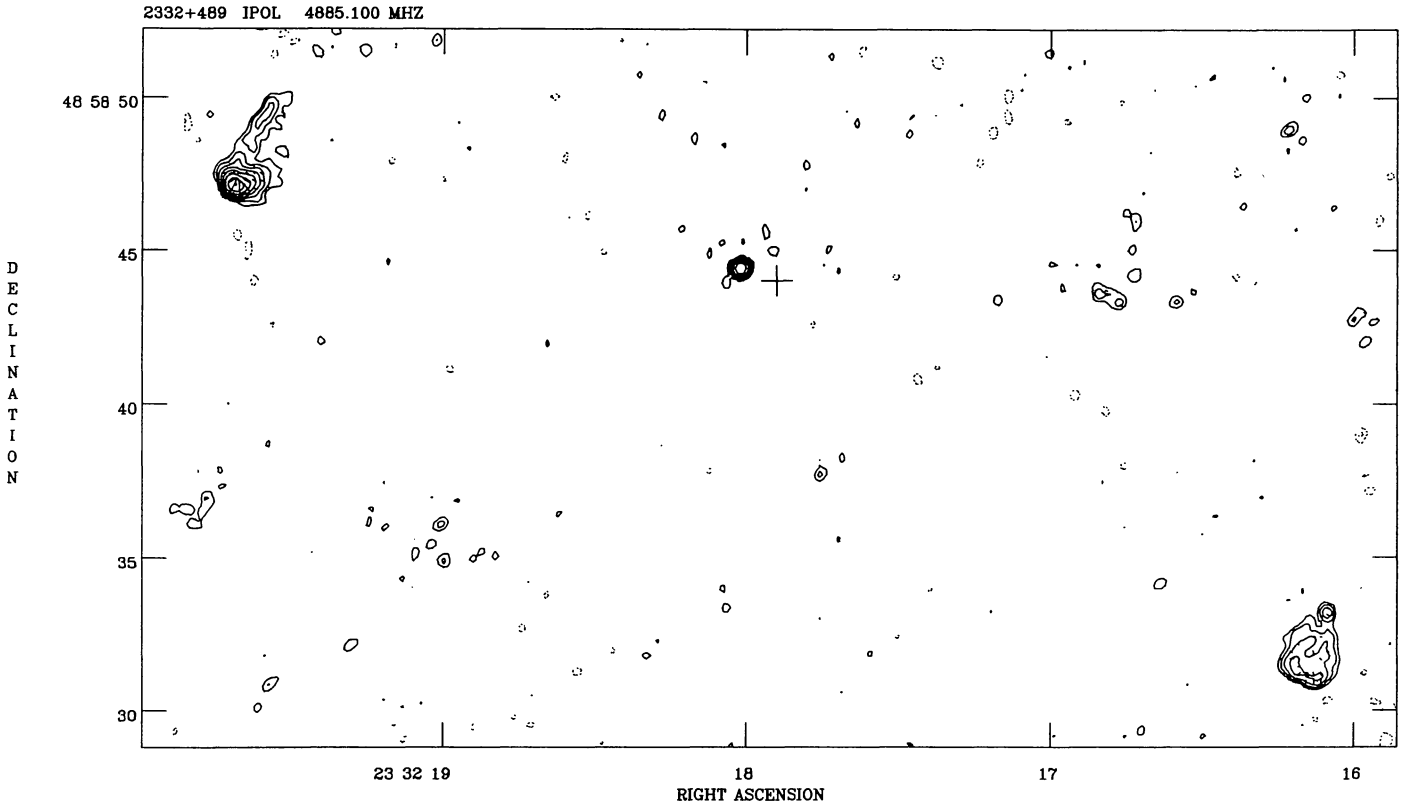

FIG. 170.—2332+489 at 5 GHz; contours $0.2 \times (-1, 1, 2, 4, 8, \cdots)$ mJy beam^{-1}; restoring beam $0''.35 \times 0''.32$ in P.A. $-18°$; polarization vector scale 5 mJy beam^{-1} arcsec^{-1}.

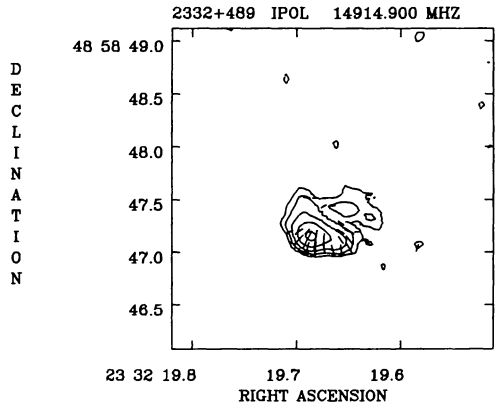

FIG. 171.—2332+489 at 15 GHz; contours $0.3 \times (-1, 1, 2, 4, 8, \cdots)$ mJy beam^{-1}; restoring beam $0''.16 \times 0''.15$ in P.A. 79°; polarization vector scale 5 mJy beam^{-1} arcsec^{-1}.

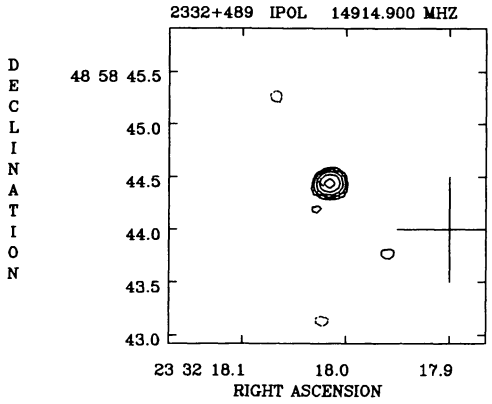

FIG. 172.—Same as Fig. 171

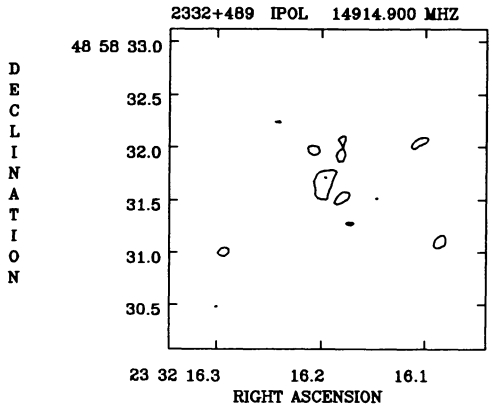

FIG. 173.—Same as Fig. 171

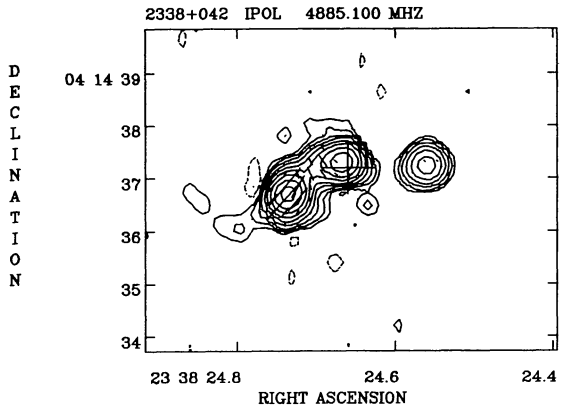

FIG. 174.—2338+042 at 5 GHz; contours $0.6 \times (-1, 1, 2, 4, 8, \cdots)$ mJy beam^{-1}; restoring beam 0.″40; polarization vector scale 20 mJy beam^{-1} arcsec^{-1}.

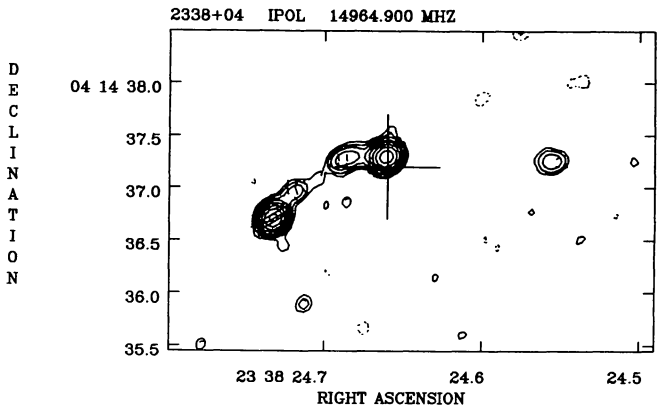

FIG. 175.—2338+042 at 15 GHz; contours $0.3 \times (-1, 1, 2, 4, 8, \cdots)$ mJy beam^{-1}; restoring beam 0.″14 × 0.″13 in P.A. −36°; polarization vector scale 20 mJy beam^{-1} arcsec^{-1}.

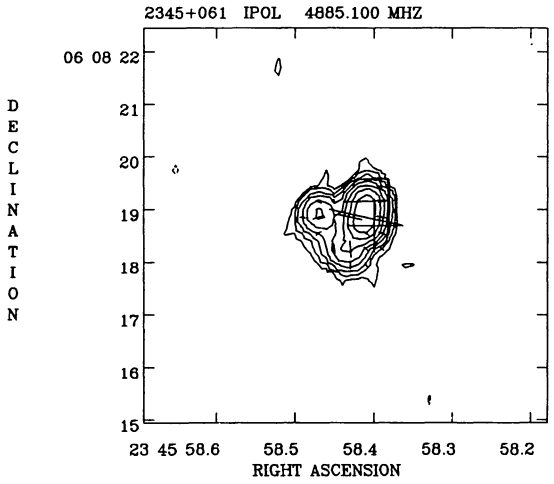

FIG. 176.—2345+061 at 5 GHz; contours $0.6 \times (-1, 1, 2, 4, 8, \cdots)$ mJy beam^{-1}; restoring beam 0.″40; polarization vector scale 5 mJy beam^{-1} arcsec^{-1}.

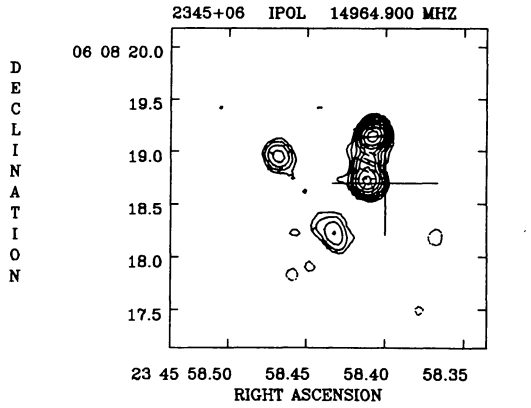

FIG. 177.—2345+061 at 15 GHz; contours $0.45 \times (-1, 1, 2, 4, 8, \cdots)$ mJy beam^{-1}; restoring beam 0.″14 × 0.″13 in P.A. −37°; polarization vector scale 10 mJy beam^{-1} arcsec^{-1}.

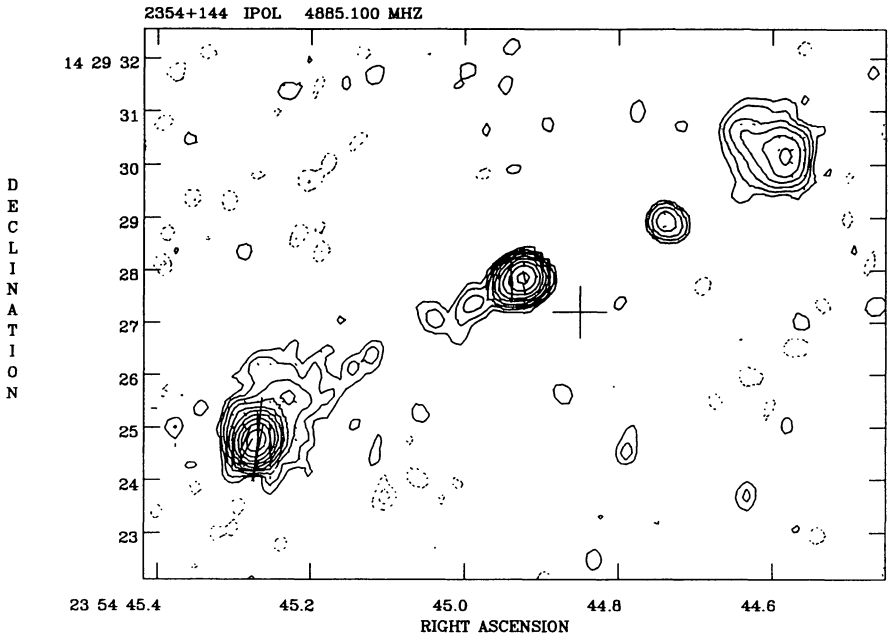

FIG. 178.—2354+144 at 5 GHz; contours $0.2 \times (-1, 1, 2, 4, 8, \cdots)$ mJy beam^{-1}; restoring beam 0″.39 × 0″.35 in P.A. 5°; polarization vector scale 10 mJy beam^{-1} arcsec^{-1}.

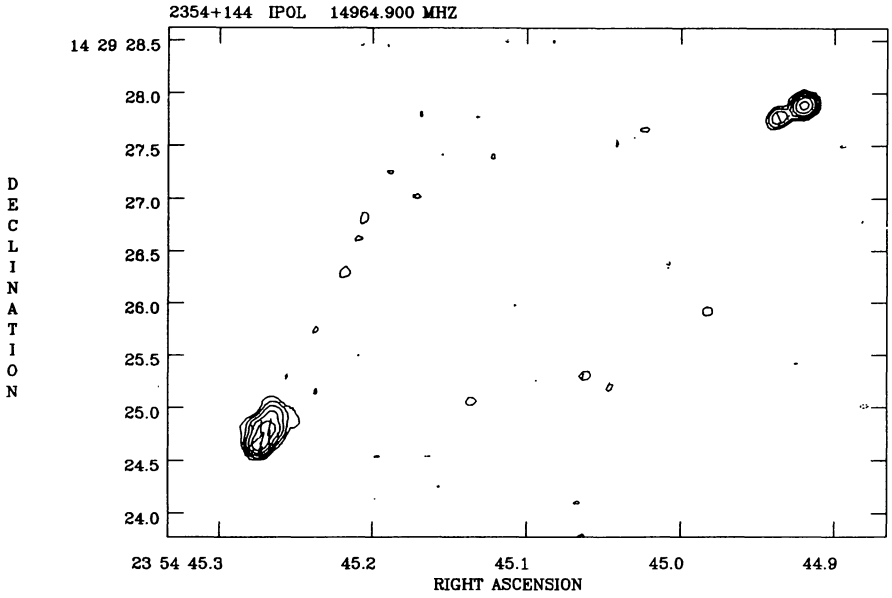

FIG. 179.—2354+144 at 15 GHz; contours $0.3 \times (-1, 1, 2, 4, 8, \cdots)$ mJy beam^{-1}; restoring beam 0″.13 × 0″.12 in P.A. −62°; polarization vector scale 5 mJy beam^{-1} arcsec^{-1}.